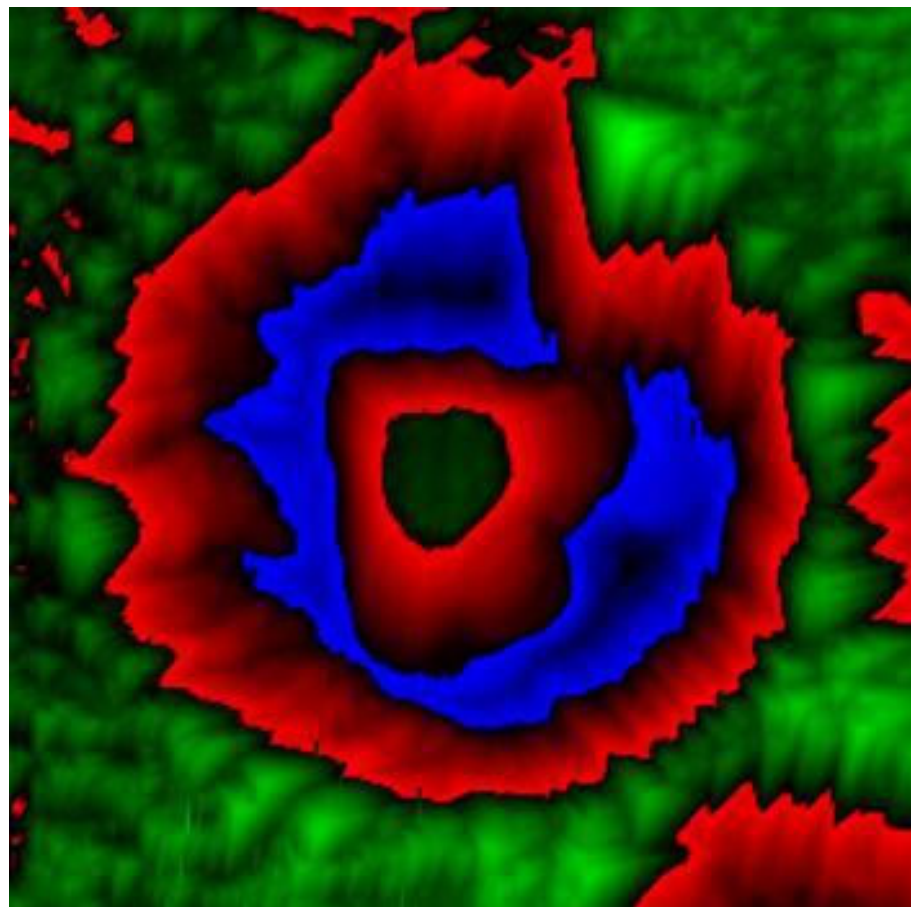


Bjørn Rune Sørås Rogne

# Application of Focused Ion Beam (FIB) on Arctic Steels

Trondheim, 24 June, 2010

NTNU  
Norwegian University of  
Science and Technology  
Faculty of Engineering Science and Technology  
Department of Product Development and Materials





Bjørn Rune Sørås Rogne

# Application of Focused Ion Beam (FIB) on Arctic Steels

TMM4910 - Structural Integrity, Master Thesis

Trondheim, 24 June, 2010

Norwegian University of Science and Technology (NTNU)  
Faculty of Engineering Science and Technology (IVT)  
Department of Product Development and Materials (PuMa)







## Preface

In the same year as NTNU celebrated 100 years of innovation, I started my work on my Master's thesis. Today's eager towards technology at nanoscale made the subject of this thesis suitable for its time.

Already in advance of this work I was privileged to be trained in use of a FIB/SEM dual beam system. The training was arranged by NTNU NanoLab, supervised by Chief Engineer Søren Heinze, and carried out together with my supervisor Professor Christian Thaulow. Even after the training Thaulow has been present during most of the laboratory work done at the dual beam system.

The steel material used in this work was provided by my contact person in SINTEF Erling Østby and master student Svein P. Astad. Astad heat treated the steel to form islands of MA that was a god basis of this work.

In the end of February Hysitron and Institut für Neue Materialien (INM) arranged Nanobrücken Nanomechanical Testing Workshop And Hysitron User Meeting in Saarbrücken. Attending the arrangement gave a brief introduction to the state of art research in this field. My contribution of a poster (the poster abstract is enclosed in Appendix A and referred to in [26]) during the conference made it easier to get contact and attention of my ongoing work.

Fortunately NTNU and INM are co-operating in this field and an appointment was made so I could stay some days after the conference to test FIB prepared specimens I brought with me. The testing gave me an opportunity to learn from people experienced with this kind of work. During the weekend stay Nousha Kheradmand, Afrooz Barnoush and his PhD candidate Mohamad Zamanzadeh were very helpful.

Here in Trondheim the testing with nanoindenter was delayed due to a contaminated transducer, that was sent to USA for cleaning. In forehand and after the problems PhD student Adina Basa, PhD student Masoud Asgari and Post doctor Jianying He have helped me with training, use of the system and problem solving.

The delay caused by the nanoindenter down time and later reparation of the dual beam system result in an extended handing in deadline to 12 July. In consultation with my supervisor the Acoustic Emission (AE) part of the problem text was removed and the title was adjusted according to this.

I am thankful to all the people that have influenced and helped me during the semester, including all the peoples named above, and especial my supervisor Professor Thaulow which has showed large interest in the work I have done this semester.



# Problem Text

THE NORWEGIAN UNIVERSITY  
OF SCIENCE AND TECHNOLOGY  
DEPARTMENT OF ENGINEERING DESIGN  
AND MATERIALS

**MASTER THESIS SPRING 2010  
FOR  
STUD. TECHN. BJØRN RUNE SØRÅS ROGNE**

**APPLICATION OF FOCUSED ION BEAM (FIB) AND ACOUSTIC EMISSION (AE)  
ON ARCTIC STEELS**

**Anvendelse av Focused Ion Beam og akustisk emisjon på arktiske stål**

Focused Ion Beam (FIB) can be used to prepare micro-sized specimens. The specimens are machined by Ga<sup>+</sup>-ions, while another beam supports the SEM images. Hence, FIB is also defined as a dual beam system. There exists only limited experience from applying FIB on steel and the main aim with the Master thesis is to define optimum conditions for FIB machining of steel, and perform own experiments. The experiments also include testing of the machined specimens in the nanoindenter, and supporting examinations with assistance of other metallographic techniques. In addition also acoustic emission shall be explored as a tool to obtain information about the detailed fracture mechanisms. This includes AE monitoring of weld thermal simulated specimens, and if possible also AE monitoring of FIB prepared specimens.

The following topics shall be answered

1. Describe the FIB system and perform a literature study on the application of FIB on metals in general and especially on steel. The presentation should include machining of pillars, fracture mechanics specimens and preparation of 3D images of the grain structures. Discuss limitations and advantages.
2. Perform systematic examinations to optimize the FIB parameters for steel, and define detailed procedures. Discuss limitations
3. Optimize the nanoindentation testing of the FIB specimens, and define detailed procedures. Discuss limitations.
4. Prepare FIB specimens from selected steel samples and perform testing. Important parameters are the size-, shape-, crystallographic orientation- and microstructural effects. Cooperation with Master-students working with EBSD and weld thermal simulation testing is encouraged.
5. AE signals from selected tests (geometry, temperature, microstructure) shall be evaluated, if possible this also includes AE monitoring of FIB prepared specimens

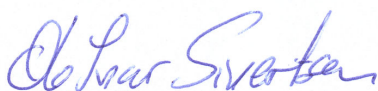
The thesis should be written as a research report with summary both in English and Norwegian, conclusion, literature references, table of contents, etc. During preparation of the text, the candidate should make efforts to create a well arranged and well written report. To ease the evaluation of the thesis, it is important to cross-reference text, tables and figures. For evaluation of the work a thorough discussion of results is appreciated.

Three weeks after start of the thesis work, an A3 sheet illustrating the work is to be handed in. A template for this presentation is available on the IPM's web site under the menu "Undervisning". This sheet should be updated when the Master's thesis is submitted.

The thesis shall be submitted as two paper versions. One electronic version is also requested on a CD or a DVD, preferably as a pdf-file.

#### Contact persons

Erling Østby, SINTEF  
Søren Heinze, NTNU NanoLab  
Adina Basa, PhD student NTNU



Ole Ivar Sivertsen  
Head of Division



Christian Thaulow  
Professor/Supervisor



NTNU  
Norges teknisk-  
naturvitenskapelige universitet

Institutt for produktutvikling  
og materialer

## Abstract

The background of the performed study was to investigate the focused ion beam (FIB) system and evaluate if its applications can be used on steels to better understand how steel behave. An Arctic steel quality was investigated during FIB fabrication of micro sized specimens, with subsequently loading with a nanoindenter instrument.

A important concern of high strength low alloy steel is to obtain sufficient high fracture toughness after heat affection due to welding and at temperatures as low as  $-60$  °C. The ductile to brittle transition reduces the fracture toughness and allows brittle fracture to occur. A model that describes the brittle fracture mechanism is the double-barrier model which uses local material characteristic and statistical grain and particle descriptions to model the fracture curve.

With the focused ion beam small micro sized specimens were fabricated locally in the microstructure. By using a nanoindenter instrument the specimens were loaded in a controlled manner to obtain the load and displacement data. Procedures describing the FIB milling and nanoindenter loading were developed. The loading data and complementary SEM pictures before and after the testing are used to better understand the deformation behavior in local part of the microstructure. Investigations such as this can help to better understand and develop models such as the double-barrier model. With a good understanding of the brittle fracture mechanisms in steel, development can be done to control the mechanisms that lead to the observed brittle behavior.

Micro sized pillar and fracture mechanical specimens were fabricated in the base material and a heat treated sample, but only the base metal plate was tested. The tested specimens shows somewhat concise results in spite of the unknown crystallography of the tested specimens. Characterization of the crystallography and by holding the specimens at sub grain size it should be feasible to accomplish more concise results at later studies. Further development of holders, preparation and testing procedure will make the testing easier to accomplish in later tests.

At this time it is not possible to do the loading at temperatures as low as  $-60^{\circ}$ , still it would be of great interest to observe the ductile-to-brittle transition for micro sized specimens in the future.



## Sammendrag

Bakgrunnen for det gjennomførte arbeidet har vært å undersøke fokusert ionstråle (focused ion beam, FIB) systemet og evaluere dets anvendelsesområdet opp mot stål og ståls oppførsel. Et arktisk stålkvalitet blitt undersøkt gjennom FIB fabrikasjon av prøver på mikrometerstørrelse. Etter fabrikasjon ble prøvene belastet i et nanoindenterings system.

Det høyfaste stålet av typen HSLA (high strength low alloy) må opprettholde en høy bruddseighet selv etter en varmpåvirket mikrostruktur og ved temperaturer så lave som  $-60\text{ }^{\circ}\text{C}$ . Overgangen fra duktil til sprø bruddoppførsel reduserer bruddseigheten og tillater sprøbrudd å skje. En modell som beskriver den sprø bruddmekanismen er "double-barrier" modellen som tar utgangspunkt i lokale materialegenskaper og statistiske fordelinger av korn og partikkel forekomster for å simulere når sprøbrudd inntreffer.

Med den fokuserte ionstrålen ble det produsert prøver på mikrometerskala lokalt i mikrostrukturen. Nanoindenter ble siden benyttet for å kontrollert belaste prøvene og samtidig logge lasts- og forskyvningsdata. Prosedyrer for fokusert ionstråle produksjonen og belastningen hved hjelp av nanoindentering ble utviklet. Både data under belastning og scanningselektronmikroskop (scanning electron microscope, SEM) bilder tatt før og etter forsøkene ble brukt for å evaluere deformasjons oppførsel lokalt i materialet. Slike undersøkelser kan være med på å forstå lokal materialoppførsel og være med på å utvikle modeller som "double-barrier" modellen. En god forståelse for materialets oppførsel i stål kan videre utvikling føre til bedre kontroll av mekanismene som fører til sprøbrudd.

Pilarer og bruddmekaniske prøver ble laget i både grunnmaterialet og en varmebehandlet mikrostruktur fra grunnmaterialet, hvor bare prøvene fra grunnmetallet ble belastet. Til tross for den ukjente krystallografiske orienteringen til de testede prøvene ble resultatene konsise, men med noe stor dataspredning. Karakterisering av krystallografisk orientering og ved å holde prøvegeometrien under kornstørrelsen bør data med mindre spredning være mulig å oppnå ved senere undersøkelse. Videre utvikling av holdere, preparering og testprosedyrer vil gjøre forsøkene enklere å gjennomføre senere. Ved dette tidspunktet er det ikke mulig å belaste prøver ved så lav temperatur som  $-60\text{ }^{\circ}\text{C}$ , i fremtiden vil det være spesielt interessant å undersøke overgangen fra duktil til sprø bruddoppførsel også for prøver på mikrometer skala.





# Contents

<b>Preface</b>	<b>i</b>
<b>Problem Text</b>	<b>ii</b>
<b>Abstract</b>	<b>v</b>
<b>Sammendrag</b>	<b>vii</b>
<b>Contents</b>	<b>ix</b>
<b>1 Introduction</b>	<b>1</b>
<b>2 Literature Survey</b>	<b>3</b>
2.1 Ductile-to-Brittle Transition in Steel . . . . .	3
2.1.1 The Double-Barrier Model . . . . .	5
2.2 The Focused Ion Beam System . . . . .	8
2.3 FIB Applications . . . . .	15
2.3.1 Basic Applications . . . . .	15
2.3.2 FIB Preparation of Material Specimens for Loading . . . . .	23
2.4 SEM Compatible Metallographic Techniques . . . . .	28
2.4.1 X-ray Energy Dispersive Spectroscopy . . . . .	29
2.4.2 Electron Backscatter Diffraction . . . . .	33
2.5 Three Dimensional Reconstruction . . . . .	36
<b>3 Experimental Procedure</b>	<b>39</b>
3.1 Sample Material and Sample Preparation . . . . .	39
3.2 Optimizing of FIB Specimen Fabrication . . . . .	42
3.3 Optimizing of Specimen Loading . . . . .	44
<b>4 Results and Discussion</b>	<b>49</b>
4.1 Sample and Sample Preparation . . . . .	49
4.2 Optimized FIB Preparation Procedure . . . . .	50
4.2.1 Pillar Specimen Preparation Procedure . . . . .	50
4.2.2 Cantilever Specimen Preparation Procedure . . . . .	58
4.3 Optimized Nanoindentation Testing Procedure . . . . .	63
4.3.1 Pillar Specimen Testing Procedure . . . . .	64
4.3.2 Cantilever Specimen Testing Procedure . . . . .	66
4.4 Test Results . . . . .	68
4.4.1 FIB Prepared Specimens . . . . .	68

4.4.2	Specimens After Loading . . . . .	71
4.4.3	Data From the Specimen Loading . . . . .	73
<b>5</b>	<b>Conclusion and Further Work</b>	<b>77</b>
	<b>References</b>	<b>79</b>
	<b>Appendix</b>	<b>I</b>
<b>A</b>	<b>Poster Abstract</b>	<b>I</b>
<b>B</b>	<b>Load Estimate</b>	<b>II</b>
B.1	Pillar . . . . .	II
B.2	Cantilever . . . . .	III
<b>C</b>	<b>Test Data of Pillar Series 100</b>	<b>V</b>
<b>D</b>	<b>Test Data of Pillar Series 200</b>	<b>X</b>
<b>E</b>	<b>Test Data of FM Series 100</b>	<b>XVI</b>

# 1 Introduction

The Arctic region is known for its cold and harsh climate and environment. Onshore the temperatures can go as low as  $-60\text{ }^{\circ}\text{C}$  and offshore the sea has several other challenges. Wind, sea waves, drifting icebergs and icing of constructions is a number of important sources of high construction loads. Large distances and little infrastructure complicate installation and maintenance work. Lightweight constructions simplify the transport and installation, and at the same time reduce the material amount and ecological footprint. If a construction is overloaded it must withstand the large loads and major deformations without total failure and a catastrophic event.

At this time effort in qualifying high strength low alloy (HSLA) steel for Arctic and cold conditions are being done. Allowance of using higher strength steel grades in constructions will reduce the necessary steel amount in a construction and at the same time reduce the weight. One of the largest concerns is the heat treatment due to welding combined with low temperatures which makes the steel brittle. If a failure happens in form of a brittle fracture there will exist little deformations and the fracture happens fast and with little prewarning. To avoid an unstable fracture like this the steel must have high fracture toughness that corresponds to a ductile behavior during fracture. Fracture mechanical samples with different geometries and weld simulated microstructure are tested to quantify the fracture toughness properties. Existence of hard and brittle phases, mainly martensite, in a ductile surrounding material is one of the expected reasons for the brittleness observed in specific heat treatments. To better understand the role of brittle phases the fracture mechanical testing is combined with acoustic emission (AE) monitoring.

Technological development toward miniaturized mechanical systems has the last years had a rapid development and is growing in areas of applications. One example of this is the micro electro mechanical systems (MEMS) devices. Consideration of failure in such devices combined with research for new and well suited materials have led to wide test methods to obtain a variety of parameters and properties. The observed size effect at small scales is significant, something that forces the testing to be performed at small real size geometries.

The interest of smaller scale effects and a better fundamental understanding of the mechanisms behind material deformation have led to a range of test methods at micro and nanometer scale. In the last years fabrication of micro sized pillars, by using a focused ion beam (FIB), has been extensive in use. By using a nanoindenter to load the pillars, micromechanical parameters can be obtained and used to characterize the size effect and the mechanisms behind it.

The work presented in this thesis will try to understand the FIB preparation technique used to prepare micro and sub micro sized specimens. There will be made micro sized specimens from HSLA steel that is designed to be loaded in a

nanointenter system to obtain mechanical properties. The small specimens allow individual grains and phases to be mechanical tested and characterized. The aim is to better understand the deformation mechanisms in steel and contribute to a better understanding or characterization of the ductile-to-brittle phenomenon.

## 2 Literature Survey

The literature survey starts by introducing the ductile-to-brittle transition in steels (Section 2.1), including the promising double-barrier model (Section 2.1.1). Double-barrier model describes an example on how brittle mechanisms can be modeled by using local properties and statistical data of the microstructure. The focus is thereafter moved to the focused ion beam (FIB) system (Section 2.2) and its applications (Section 2.3). This will be discussed in detail and be the main part in the literature survey section. Metallographic characteristics techniques compatible for a scanning electron microscopy (SEM) environment is presented in Section 2.4. The x-ray energy dispersive spectroscopy (XEDS) and electron backscatter diffraction (EBSD) techniques are powerful when combining with a FIB/SEM dual beam system. The same combination is able to reproduce a three dimensional material representation (Section 2.5).

### 2.1 Ductile-to-Brittle Transition in Steel

Arctic conditions are known to have a harsh environment. Expected temperatures can be as low as  $-60^\circ$  and there are possibilities for high applied loads. Consequence might be large deformations in the structures. In such situations

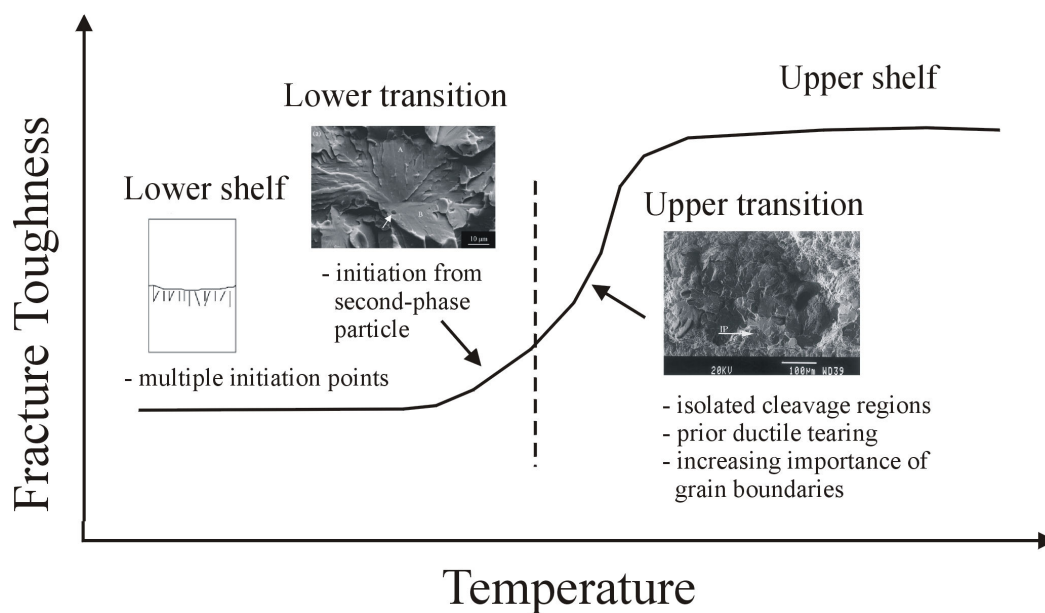


Figure 1: The ductile-to-brittle transition (DBT) in steel. When the temperature is reduced to the DBT temperature ( $T_{DBT}$ ) a sudden drop and large data scatter is seen in the fracture toughness. The figure is taken from [29, p. 23].

the steel must withstand high loads without total failure. To do this an adequate fracture toughness value is vital. An important concern in such circumstances is the ductile-to-brittle transition (DBT) observed in steels when the temperature goes down. Figure 1 [29, p. 23] illustrates this fact showing the rapid reduction of the fracture toughness when the temperature decreases to a DBT temperature ( $T_{DBT}$ ), indicated with a dashed line in the figure. Around the  $T_{DBT}$  large scatter in data is observed. As the curve name states the fracture behavior changes from fracturing by ductile manner to brittle fracture. The brittle fracture behavior is especially important to avoid. Brittle fracture usually happens fast and over long distances with none or minimal of warning signals.

Structural steels for Arctic conditions are usually high strength low alloy (HSLA) steels with good base metal fracture toughness properties. When the base metal is welded during structure production a zone around the weld bead is heated, followed by change in microstructure and material properties of the base metal. The heat affected zone (HAZ) is associated with lower toughness properties and a higher  $T_{DBT}$  than the rest of the base metal. HAZ is not discussed in detail here, but Figure 2 [9, p. 564] shows how the zone is divided into sub zones defined by the peak temperature. For a single-pass weld, in Figure 2(a), four sub zones are produced, and the coarse grained zone (CG HAZ) is generally associated with the zone having lowest toughness. During multipass welds, in Figure 2(b), the zones produced during the first weld are reheated and a number of new zones experience two heat cycles. For low carbon structural steels it is often found that the intercritically reheated coarse grained heat affected zone (IC CG HAZ) has the lowest toughness [9, p. 563]. The IC CG HAZ is the small region marked with A in Figure 2(b).

Davis and King [9] investigated the IC CG HAZ for three steels and concluded that the minimum impact toughness cannot be directly associated with the amount of MA (high-carbon martensite with some retained austenite) constituents being present. A near connected grain boundary network of blocky MA particles that are significantly harder than the internal grain microstructure, without grain refinement, gives the lowest impact toughness. Between close blocky MA particles it appears that residual transformation-induced stresses and stress concentration effects, resulting from debonding of MA particles, is the mechanism leading to the reduced toughness [9, p. 573]. Lambert-Perlade *et al.* [20] look at the fracture properties of a HSLA steel with weld thermal simulated CG HAZ and IC CG HAZ microstructures. It was observed that for the fracture toughness curves the  $T_{DBT}$  is increased from about  $-120$  °C for the base metal to about  $30$  °C for the IC CG HAZ simulated samples. To model the observed behavior three weakest-link probabilistic models were applied to account for the DBT fracture toughness curve. The most promising double-barrier (DB) model is described

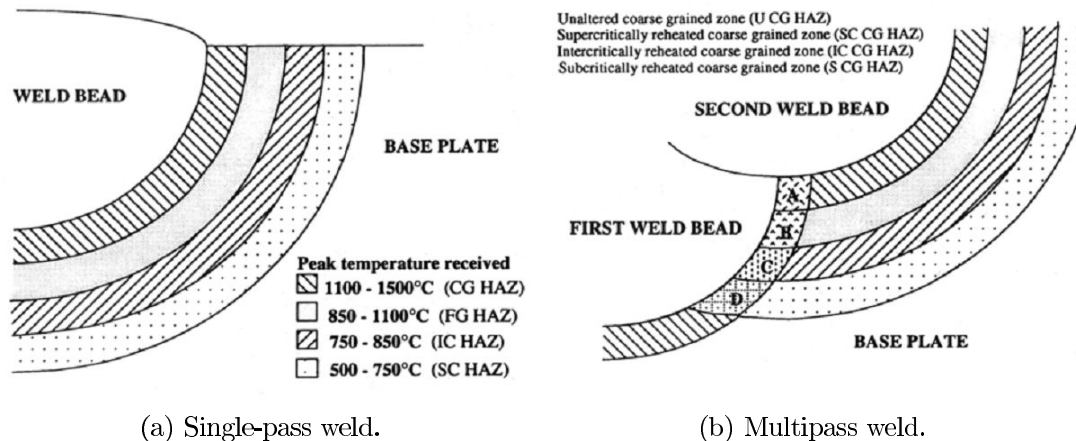


Figure 2: The heat affected zone of (a) single-pass weld and (b) multipass weld. Taken from [9, p. 564].

below and highlights some of the observations done by Lambert-Perlade *et al.* [20].

### 2.1.1 The Double-Barrier Model

The DB model assumes that brittle fracture occurs. Related to the DBT curve in Figure 1 the steel is close to or beneath the  $T_{DBT}$ . Hard and brittle particles in the microstructure are the source to the brittle cleavage fracture. The particles might be MA particles, carbides or other hard and brittle species. On the way to the final cleavage fracture, that starts trough or at a particle, a micro cleavage fracture might be stopped at a barrier. The barrier most likely to stop the micro cleavage fracture is the boundary between the particle and the grain lattice or the boundary between two grains. In the experiment performed by Lambert-Perlade *et al.* [20] the particles are MA constituents in a bainitic sounding microstructure. The prior austenitic grain size, where high angular grain boundaries exist, is the grain boundary barrier that is able to stop a micro fracture. In the following part the hard and brittle particle is assumed to be a blocky MA constituent in a bainitic microstructure.

Figure 3 shows the different steps in the DB model. *Step 0*, Figure 3(a), is the start condition where a MA particle has its place in a surrounding bainitic microstructure. When a load is applied the local maximum principal stress ( $\sigma_I$ ) around the particle give a corresponding maximum principal stress inside the particle ( $\sigma_{MA}$ ).  $\sigma_{MA}$  is given in Equation (1), where  $\sigma_{eq}$  is the local von Mises equivalent stress in the bainite matrix and  $\sigma_y$  is the yield stress in the bainite matrix. When  $\sigma_I$  exides  $\sigma_y$  the  $\sigma_{MA}$  will shortly achieve its critical stress value  $\sigma_{MA}^c$  where the

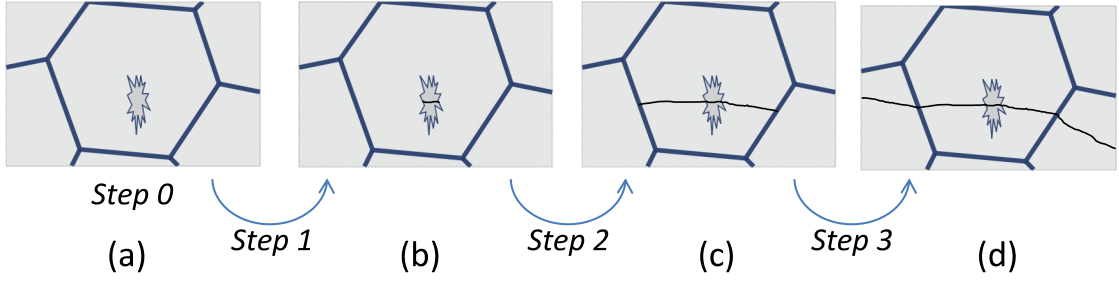


Figure 3: Shows the steps in the double-barrier (DB) model. Based on figure from [20, p. 1049].

particle fractures.

$$\sigma_{MA} = \sigma_I + 1.8(\sigma_{eq} - \sigma_y) \quad (1)$$

A micro fracture initiated in *Step 0* grows fast as a cleavage fracture through *Step 1*, the passage from Figure 3(a) to (b), and reach the MA to bainite matrix boundary. In this first barrier,  $\sigma_I$  must exceed a transition stress value,  $\sigma_{pm}$ , to grow further. The subscript pm indicates that it is the particle to matrix interface. If the crack crosses the first barrier it will grow until it meets the last possible barrier at the grain boundaries in *Step 2*, the transition from Figure 3(b) to (c). When the crack meets a high angular grain boundary the matrix to matrix stress value ( $\sigma_{mm}$ ) must be exceed to allow further crack growth. If the matrix to matrix barrier is exceed the crack grows as a cleavage fracture. No other barrier can stop the fracture ending in a final fracture. This last *Step 3* is the Figure 3(c) to (d) transition.

For a given microstructure the active barriers are varying. Three possible outcomes are given in Figure 4 and are depending on the temperature ( $T$ ). For temperatures higher than  $T_3$  the fracture is dominated of plastic tearing. At very low temperatures below  $T_1$  the initiation of crack is immediately leading to final failure. When  $\sigma_I$  local increases to the point where  $\sigma_{MA}$  equals  $\sigma_{MA}^c$  a micro crack will initiate and crack through the particle. Since  $\sigma_I$  already has exceeded  $\sigma_{pm}$  and  $\sigma_{mm}$ , none of the barriers are able to stop the ongoing micro fracture, ending in a final cleavage fracture. Lambert-Perlade *et al.* [20, p. 1043] describes the fracture surface without ductile damage at the cleavage surface. For the investigated steel the  $T_1$  temperature is around  $-170$  °C.

Temperatures between  $T_1$  and  $T_2$  allows a particle to matrix barrier controlled final fracture. When  $\sigma_I$  local increases to the point where  $\sigma_{MA}$  equals  $\sigma_{MA}^c$  a micro crack will initiate and grow through the particle. At this moment  $\sigma_I < \sigma_{pm}$  leading to micro crack arrest at the particle to matrix boundary. With further increase of  $\sigma_I$  to  $\sigma_{pm}$  the micro crack will continue propagate. Since  $\sigma_{pm} > \sigma_{mm}$  the propagating micro crack propagates through the grain boundary barriers ending in final cleavage fracture. In experiments this is observed as ductile damage around



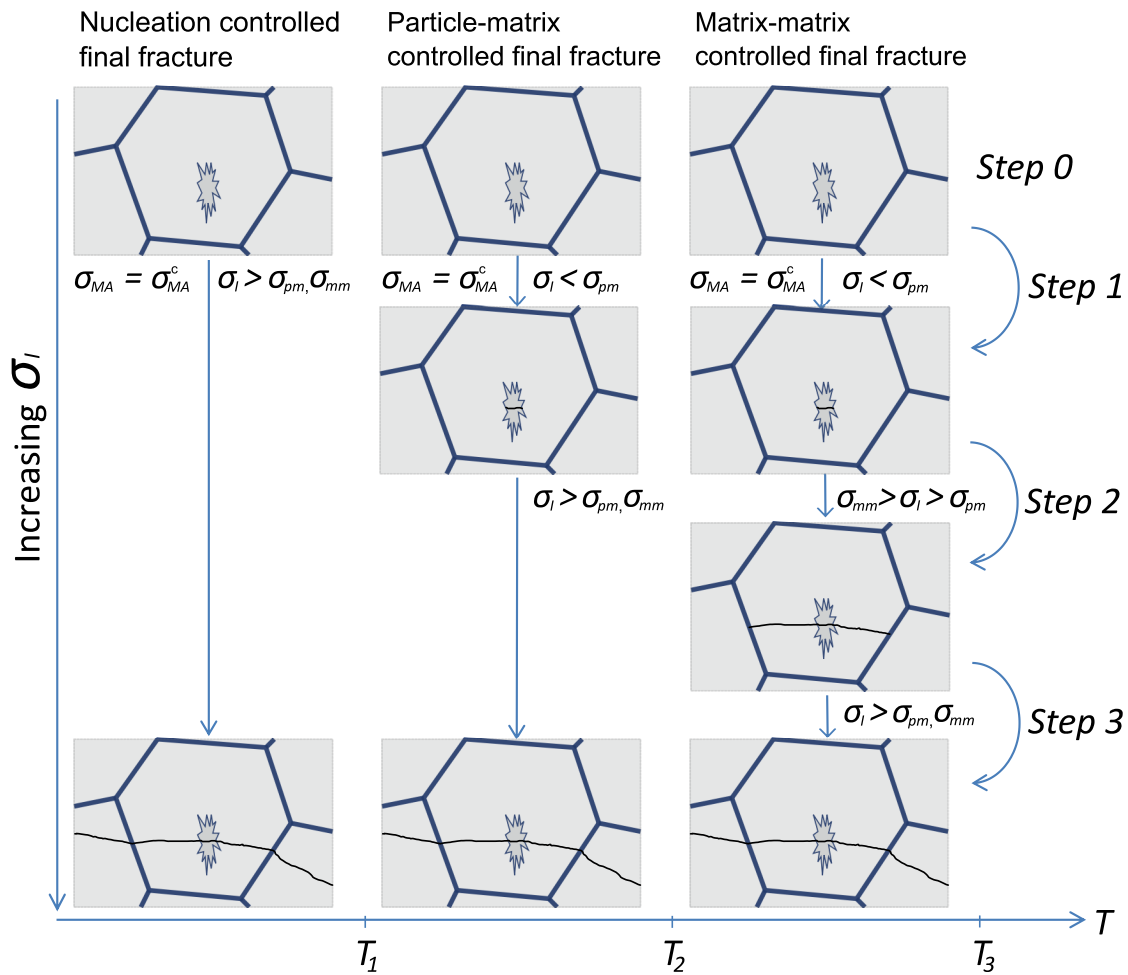


Figure 4: The different cleavage fracture progress compared with the temperature ( $T$ ) for a given microstructure. At  $T < T_1$  the final fracture is nucleation controlled, at  $T_1 < T < T_2$  final fracture is particle to matrix controlled, for  $T_2 < T < T_3$  matrix to matrix controlled final fracture exists.  $T$  above  $T_3$  the failure happens during ductile tearing, which is not included in the DB model.

cracked MA particles.

At higher temperature, between  $T_2$  and  $T_3$ , the strength of the matrix to matrix interface is higher. Similar to the particle to matrix controlled final fracture, the initiated micro crack propagates until it stops at the particle to matrix interface. When the local stress increases and exceeds  $\sigma_{pm}$  the micro crack continues to propagate until it is stopped by the strong matrix to matrix interface ( $\sigma_{mm} > \sigma_I > \sigma_{pm}$ ). Even further stress increase ends in  $\sigma_I$  exceeding  $\sigma_{mm}$  and final fracture.

The DB model is used to simulate the fracture curve when brittle fracture mechanisms are the outcome. Several observations during experiments are supporting the theory. Examples of this is high-energy acoustic signals detected in forehand of a unstable fracture [20, pp. 1052–1053], which corresponds to micro crack propagation and arrest, and EBSD mapping of polished surfaces revealing that micro cracks are stopped at high angle boundaries [20, p. 1046]. The fact that the DB model relates its parameters to local material properties as yield in particle and matrix phases, strength between the interfaces and statistical distribution of grain and particle sizes makes the model very interesting.

## 2.2 The Focused Ion Beam System

The traditional focused ion beam (FIB) system consist of a vacuum system and chamber, liquid metal ion source, ion column, sample stage, detectors, gas injection system and a computer that controls the previous listed instruments. Figure 5 shows a schematic overview of the FIB system and in the following section this instruments will be briefly introduced. The combination of a FIB and a scanning electron microscope (SEM) in form of a dual beam instrument will be discussed and linked to the available equipment at NTNU NanoLab that was used in this work.

### Vacuum System

The vacuum system in a FIB system can be divided in two regions: source and ion column, and sample and detectors. The source and ion column region requires a high vacuum to avoid contamination and to prevent electrical discharge in the high voltage column. The vacuum pressure could be in the order of  $10^{-8}$  mbar. The sample and detector region call for a lower vacuum at about  $10^{-6}$  mbar. The main reason is to keep a free ion path avoiding interaction between the gas molecules and the ion beam. At pressure in  $10^{-4}$  mbar range the interaction effect becomes noticeable [12, Ch. 1].

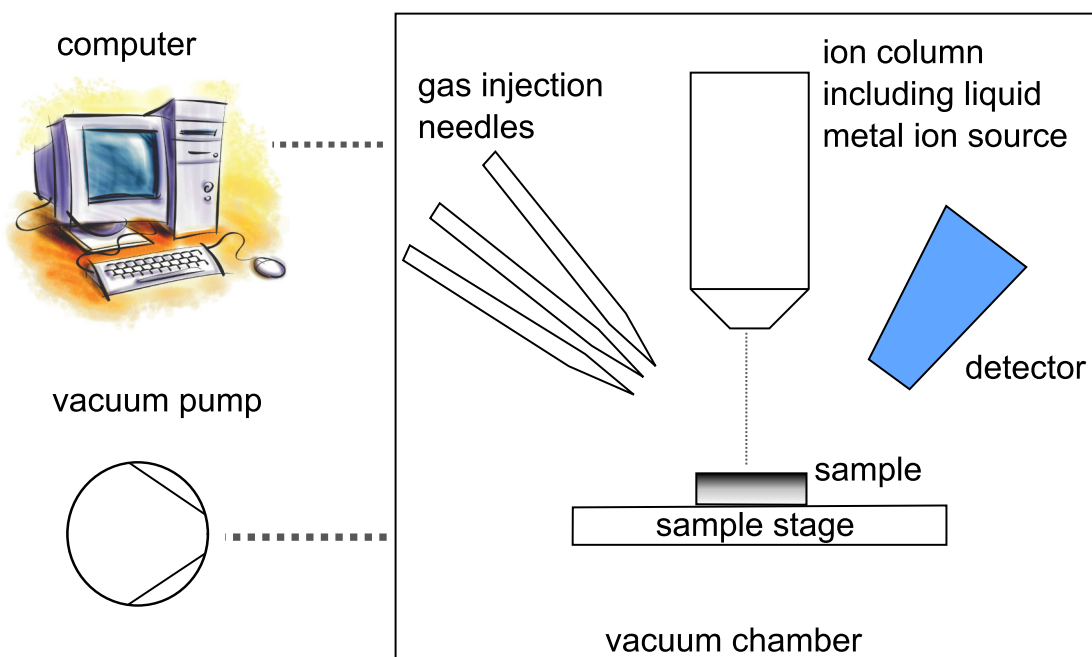


Figure 5: Schematic overview of the FIB system, based on figure from [12, p. 2].

### Liquid Metal Ion Source

To produce an ion beam a liquid metal ion source (LIMS) is needed. The metal source is melted, ionized and pulled away from the source in a controlled manner. A schematic representation is displayed in Figure 6.

The metal source is attached to a non-reacting needle and surrounded with a coil heater. The coil heater is electrical feed and heats the metal source to liquid state. The melted metal source is wetting the solid state needle. Beneath the needle tip an extractor electrode is pulling the liquid metal to the needle tip forming a small point source. The surface tension and electrostatic tension shape the point source into a Taylor cone. The electrical field from the extractor electrode pulls off and ionizes the metal by field evaporation [12, 16]. Figure 6(a) shows a principal sketch of the LIMS layout and Figure 6(b) shows a zoomed view of the needle tip and liquid metal pulled off and ionized by the electrical field.

LIMS is at this time usually made of gallium (Ga) because it has suitable properties. This includes a high surface tension, low vapor pressure, low melting point ( $T_{mp} = 29.8^\circ\text{C}$ ), reliable metal supply and long lifetime. The consumable Ga metal wets the needle to form a point source. The needle is usually made of tungsten (W) avoiding degradation of the needle geometry. When using Ga and W respectively as metal source and needle material the needle tip diameter is in the range of  $2\ \mu\text{m}$  to  $5\ \mu\text{m}$  and the formed Ga Taylor cone diameter of  $2\ \text{nm}$  to

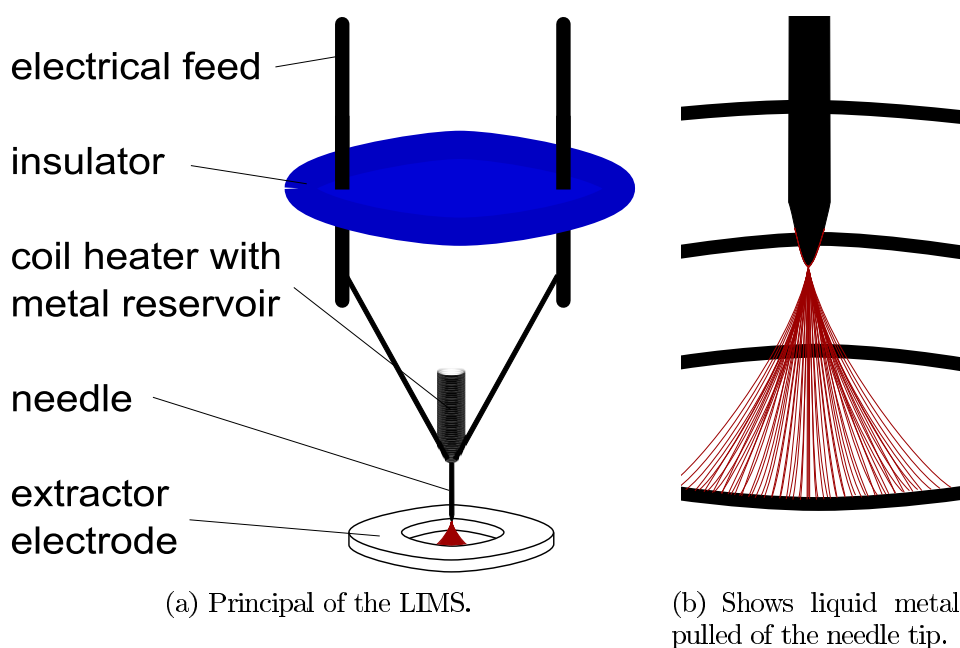


Figure 6: Sketch of (a) the liquid metal ion source (LIMS) and (b) zoomed view of the ionized metal pulled of the needle by the extractor force.

5 nm [12, 16, 37].

### Ion Column

In the ion column the ion beam extracted from the LIMS is accelerated and focused down towards a sample attached to the sample stage. The ion column is schematically shown in Figure 7. Besides the LIMS it is mainly composed of two lenses and aperture. The first lens is the condenser lens directing the ion beam downward the ion column. When the ions meet the aperture only the beam center part will pass. After the beam reduction from the adjustable aperture diameter the second lens is focusing the beam toward a point on the sample surface.

To obtain a thin beam at the sample surface a correct beam voltage, aperture diameter and working distance is important. The thinnest beam is obtained with high voltage, small aperture diameter and short working distance [12, 16].

### Sample Stage

Usually the sample stage is able of a 5-axis movement in the x, y, z, rotational and tilt axis. The stage is often as large as 300 mm and has to be very stable to perform accurate positioning. Thermal stability is a key parameter to avoid both

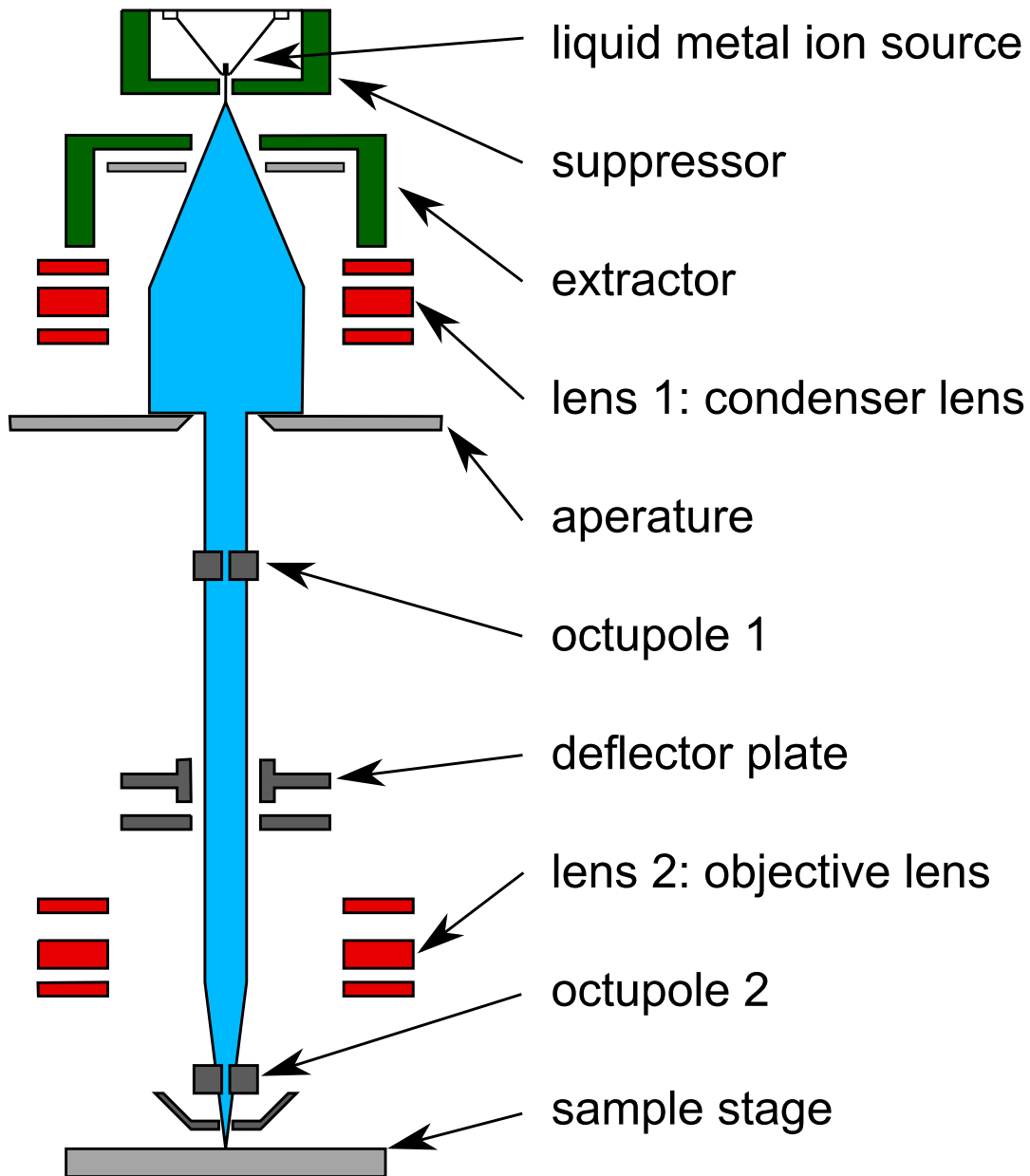


Figure 7: Principal sketch of the ion column based on figure from [15].

inaccurate positioning and specimen drift [12].

### **Imaging Detectors**

Image detectors in FIB is typical a multi-channel plate or an electron multiplier. A multi-channel plate is mounted directly above the sample and collects the secondary electrons (SE). It is two types of electron multipliers one that collect secondary electrons and another collecting secondary positive ions (SI). The electron multiplier is placed in an angle of  $45^\circ$  to the ion beam [12]. Principles behind the imaging are discussed in Section 2.3.1.

### **Gas Sources**

Often the FIB system is including a gas delivery system that allows site specific deposition or enhanced etching. The gas is delivered in controlled amount into the chamber. Use of gas injection needles allows the gas to be applied close to the point of interest usually about  $100\ \mu\text{m}$  over the surface. A deposition material is forming by letting a gas adsorbed on the sample surface near the needle outlet. When the ion beam strikes, the gas will break down and form a thin deposit layer at the surface. By repeat this deposition process the material will build up. The deposition process is a balance between milling and deposition and with too high ion beam current machining will occur. The deposited material can be a metal (W, Pt and C are common) or insulator (different glass types). Chemically enhanced sputtering or etching can be done by applying selected gases to specific specimen material [12]. The processes behind the milling, deposition and chemical enhanced milling are further discussed in Section 2.3.1.

### **The Dual-Beam System**

The FIB technology is often combined with a scanning electron microscope (SEM) column in form of a dual beam system. This combination extends the possibilities to mill complex shape and characterizations. SEM can be used to deposit very low energy deposition that does not affect the underlying surface. Three dimensional (3D) information is easy to obtain by switch between SEM imaging and milling off thin material slices. The stepwise images are then representing 3D pictures of a small volume. Instead of imaging element mapping in form of x-ray energy dispersive spectrometry (XEDS) and crystallographic analysis using electron backscatter diffraction (EBSD) detection [12]. These subjects are further discussed in Section 2.4 and 2.5.

The available FIB/SEM dual-beam system is a Helios NanoLab produced by FEI. Picture of the system is presented in Figure 8 and includes the same parts as earlier presented in Figure 5. Figure 9(a) shows inside the chamber that holds

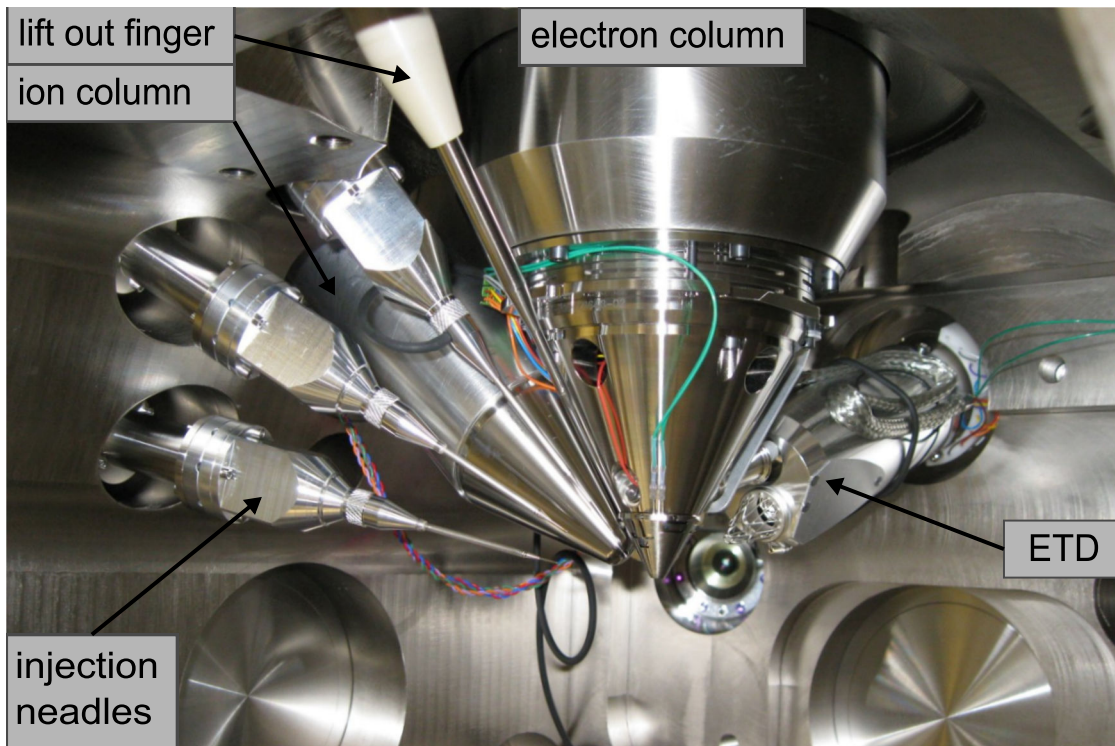
a chamber pressure lower than  $2.6 \cdot 10^{-6}$  mbar. Mounted inside the chamber ceiling is a SEM column, FIB column, Everhart–Thornley detector (ETD), three gas injection needles and a lift out finger. The lift out finger is mainly used to lift out transmission electron microscopy (TEM) samples prepared by the FIB. The SEM column is supplied with a through-the-lens detector (TLD). The ETD is of the type scintillator–photomultiplier, while TLD is a scintillator.



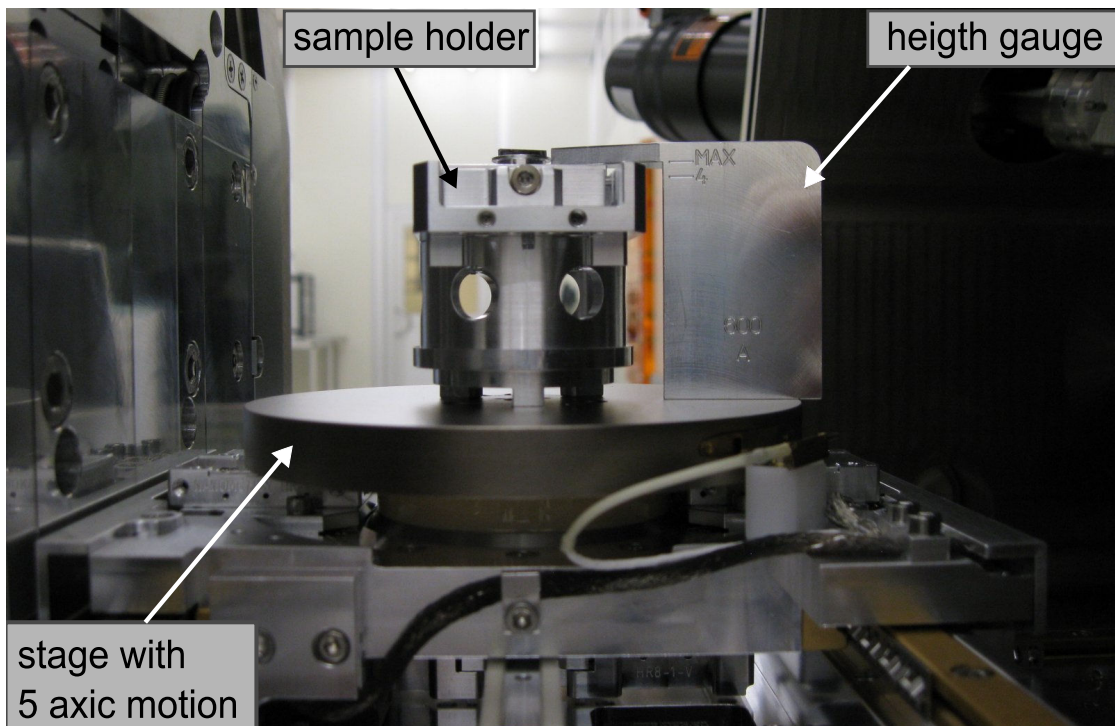
Figure 8: Picture of the Helios NanoLab FIB/SEM dual-beam system.

The FIB stage in Figure 9(b) is 150 mm in diameter and can rotate in five axis. The provided holder is placed on top of the stage with the holders emphasized in Figure 10.





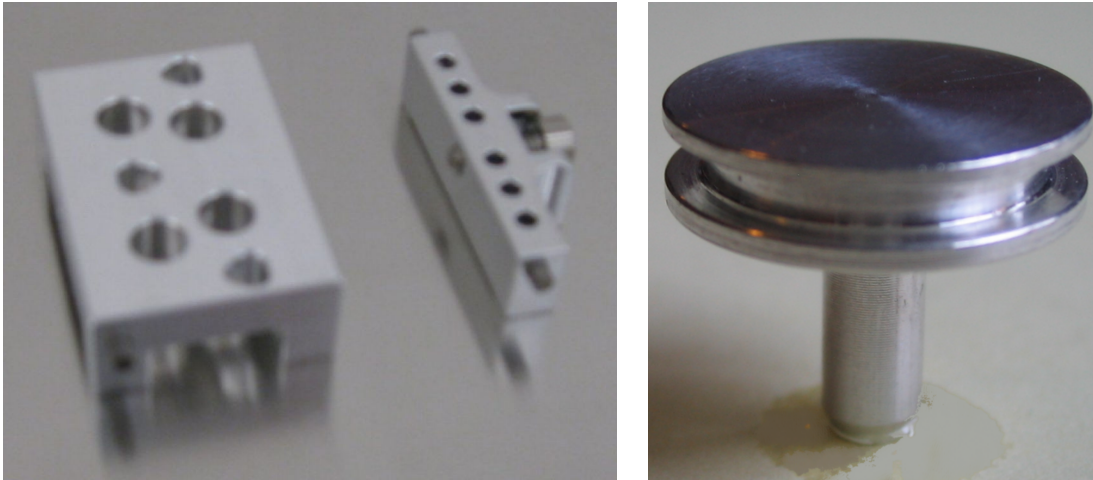
(a) Inside the FIB chamber.



(b) The FIB stage, holder and sample. The height gauge is placed at the stage.

Figure 9: Picture of (a) FIB chamber and (b) sample stage.





(a) The FIB holder.

(b) Sample stub.

Figure 10: The (a) FIB holder and (b) sample stub.

## 2.3 FIB Applications

With the basic imaging, milling, deposit and etching possibilities FIB is equipped with a large variety of functionality. The FIB/SEM platform extends the possibilities even further with ability to image and provide detail information about complex and detailed work during nanomanipulation. In these sections FIB applications are introduced along with important parameters and background information. First the basic applications is introduced in Section 2.3.1 and ends with use more specific and relevant applications for this work trough Section 2.3.2. After introducing metallographic techniques in Section 2.4 the important FIB/SEM 3D reconstruction is presented in Section 2.5.

### 2.3.1 Basic Applications

#### Imaging

To get a brief understanding of the FIB imaging process an introduction to the ion-solid interaction is needed. When a high energy  $\text{Ga}^+$  ion hits the sample surface it will interfere whit the surface material trough elastic and inelastic interactions as illustrated in Figure 11 [37]. The inelastic energy transfer happens when the ion energy is transferred to electrons in the sample. This results in ionization followed by emission of secondary electrons (SE) and electromagnetic radiation from the sample. In the elastic interaction the  $\text{Ga}^+$  ion is colliding into the sample atoms followed by series of collisions in form of a collision cascade. If the kinetic

energy transfer from the  $\text{Ga}^+$  ion into a sample atom exceeds a critical value, the displacement energy, the atom will be displaced out of position. The displaced atom will further interact with other atoms and might result in several displaced atoms. A surface atom displaced out of position might emit from the surface as sputtered particles. The sputtered particles can be charged or neutral secondary particles. Eventually the  $\text{Ga}^+$  atom stops, implanted into the sample surface [37].

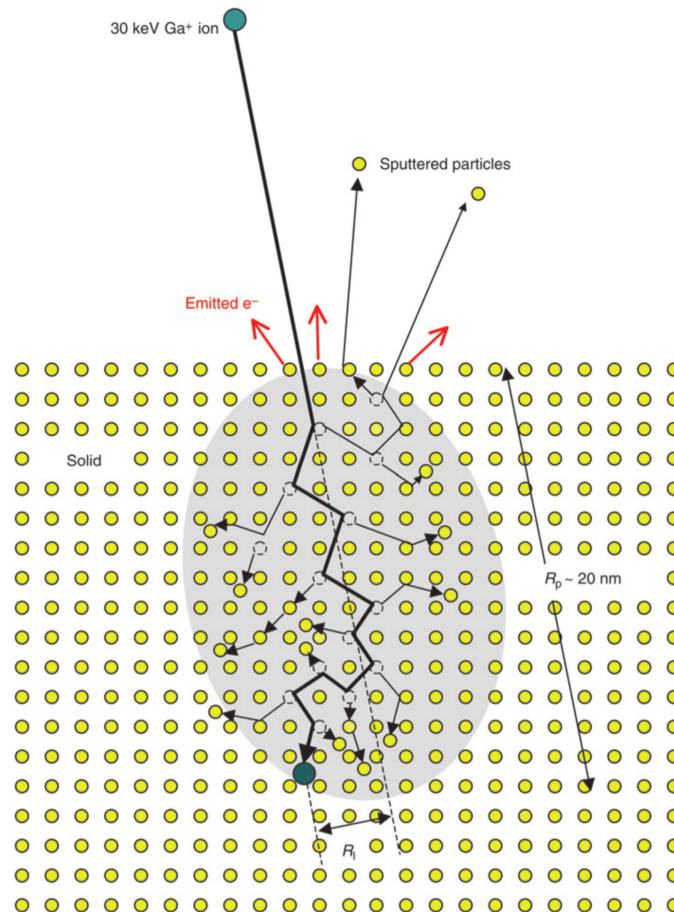
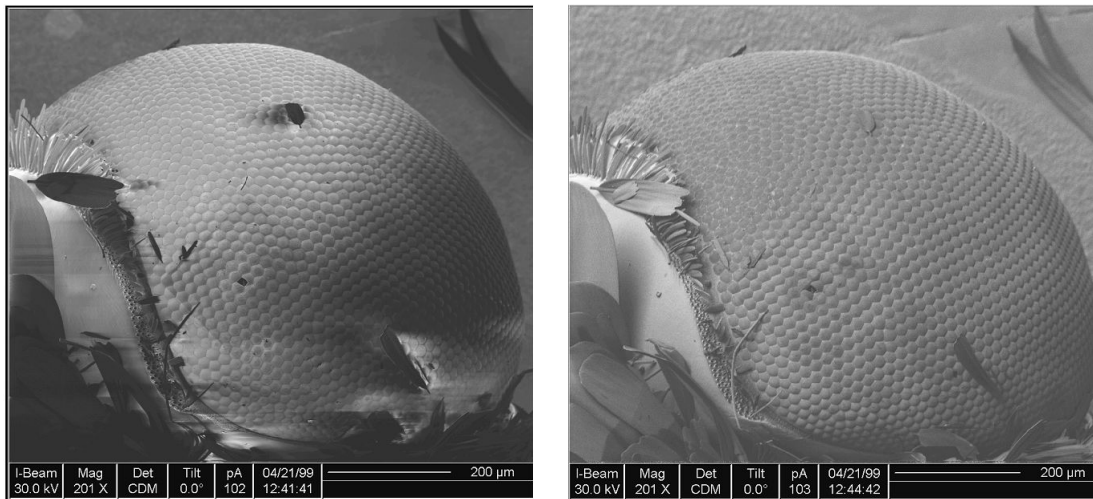


Figure 11: The collision cascade for a 30 keV  $\text{Ga}^+$  ion. When the ion enters the sample surface secondary electrons and sputtered particles are ejected from the surface. The  $\text{Ga}^+$  ion is left implanted at a statistical projected range ( $R_p$ ) and lateral range ( $R_l$ ). Figure is taken from [37, p. 391].

The ejected SE and positive charged secondary ions (SI) can be collected to form an image. Standard imaging mode is to collect the SE to form a raster image. In Figure 12 [12, p. 15] images of a bug eye produced by (a) ion induced SE and (b) ion induced SI are compared. The two images show mostly complementary

information except from some dark regions in SE image. This dark regions is caused by insulation material implanted with positive charged  $\text{Ga}^+$  ions. The positive regions attract the negative charged emitted SE, hence no electrons will be collected for these regions. These type of artifacts are not seen in the ion induced SI picture since the positive charged particles are not retained back to the surface.



(a) Secondary electron (SE) image.

(b) Secondary ion (SE) image.

Figure 12: Image of bug eye produced by (a) secondary electrons (SE) and (b) secondary ions (SI). Taken from [12, p. 15].

Picture contrast is obtained when changes occurs in sputtering direction or in SE and SI amount. This is due to change in sample topology or differences in the sample composition. The parameters that effects the picture contrast is illustrated in Figure 13. Figure 13(a) and (b) illustrates differences in crystallographic orientation for a amorphous material where in (a)  $\text{Ga}^+$  ions easily can move deep into the sample trough plane channeling and (b) the  $\text{Ga}^+$  early collides into sample atoms. A higher nucleus mass is illustrated in (c) and illustration (d) is placed at an edge showing topological differences.

The SE and SI are produced for every frame in a raster image and collected trough a detector. The use of dual-beam FIB/SEM systems allows to use a SEM to produce images while the FIB column is used for other applications. A standard imaging beam current for FIB pictures is in the range between 1.5 pA and 48 pA, where the high resolution images is obtained from the lowest beam current [7, p. 5–92].

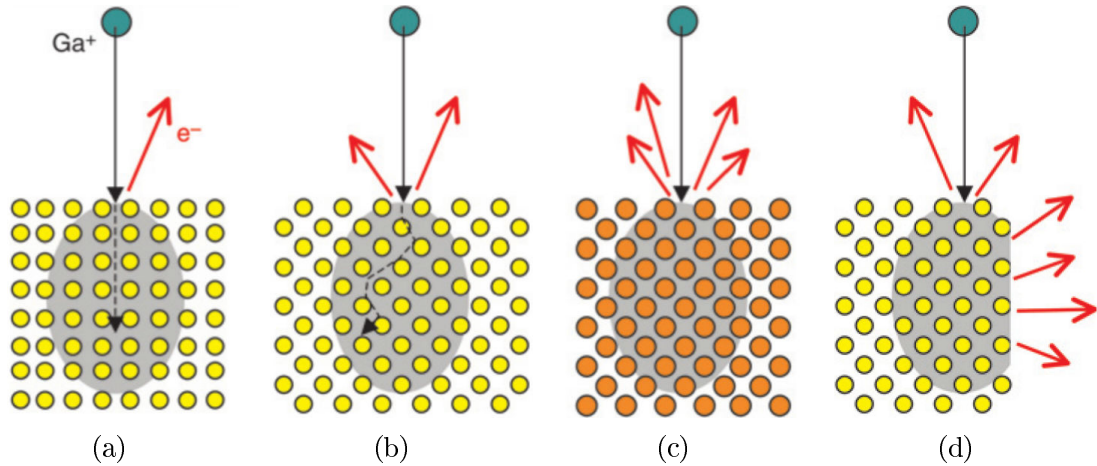


Figure 13: Showing image influence of (a), (b) different crystallographic orientation, (c) higher nucleus mass and (d) geometrical differences at the surface. Taken from [37, p. 392]

## Milling

During imaging, particles are sputtered away from the surface in a low current milling process. By increasing the ion current, and hence the sputtering rate, the process becomes a micro milling process. The milling process allows material removal from the sample surface to form desired forms. Usually the milling is done using predefined patterns or by making own scripts. The sputtering rate of the milling process depends on the same parameters as for imaging and the introduced collision cascade in Figure 11 will be discussed here and quantified. The ion–solid interaction is often simulated using Monte Carlo calculations with the programs Transport of Ions in Matter (TRIM) or Stopping of Ions in Matter (SRIM). The TRIM/SRIM simulation calculates and quantifies concerns as sputtering rate, back sputtering of  $\text{Ga}^+$  ions and the  $\text{Ga}^+$  ion implantation range for different materials. Simulations shows good consistence with experimental data. Unfortunately the TRIM/SRIM simulations do not account for difference in crystallographic orientation and must thereby be used with wariness for such phenomena.

The  $\text{Ga}^+$  ions are implanted into the material surface during imaging and milling. Several parameters are used to statistical quantify the ion range where the  $\text{Ga}^+$  ions stop. Most used parameter is the (longitudinal) projected range ( $R_p$ ) which is the ion implantation depth parallel to the ion beam (see Figure 11). TRIM  $R_p$  simulated values for a 30 keV  $\text{Ga}^+$  ion hitting perpendicular to the surface can be seen in Figure 14 for four selected solid elements.

Sputtering conditions are often quantified by the sputtering yield ( $Y$ ) which

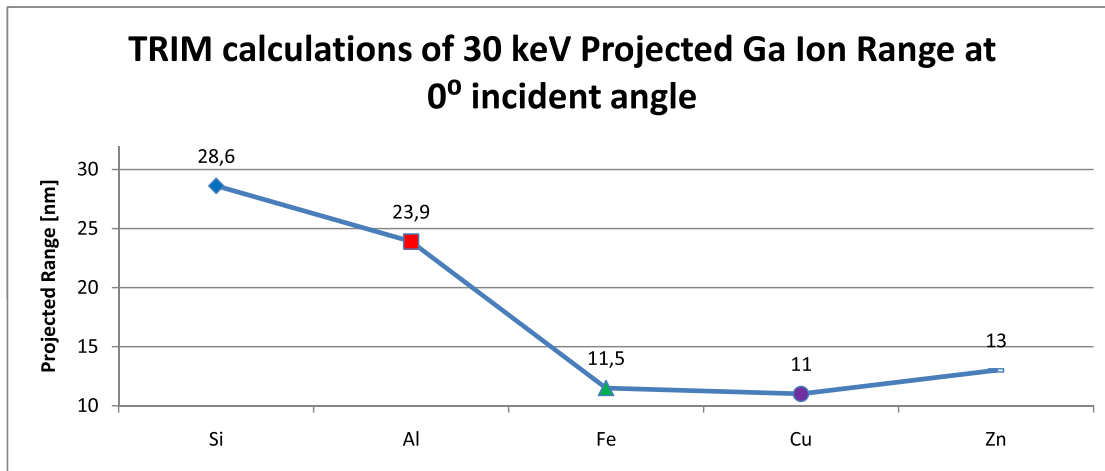


Figure 14: Projected range ( $R_p$ ) for a 30 keV  $\text{Ga}^+$  ion implanted into different solid elements. The data is found in [12, Appendix C].

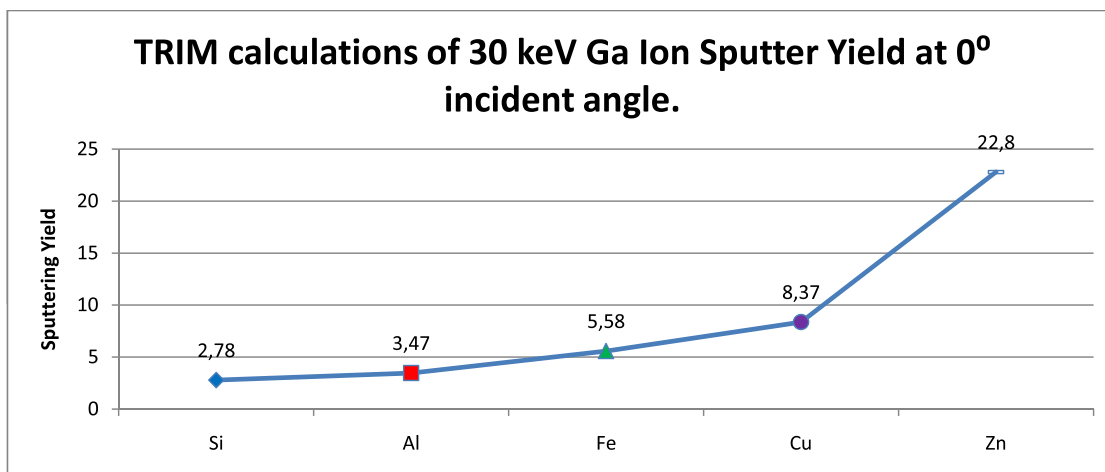


Figure 15: Sputtering yield ( $Y$ ) for a 30 keV  $\text{Ga}^+$  ion implanted into different solid elements. The data is found in [12, Appendix A].

is defined as the number of ejected particles per incidence ion [12, p. 28]. TRIM simulated values of  $Y$  is plotted in Figure 15 for 30 keV  $\text{Ga}^+$  ion hitting perpendicular at the surface. Comparing  $R_p$  with the  $Y$  values reveals that there exist an inverse ratio trend between them. Figure 16 [12, p. 41] shows a SEM image of trenches milled at 1 nA and 25 keV beam using the same pattern conditions. The experimental and simulated data shows the same trend. Different in the behavior of the different materials can be seen in the milled trenches.

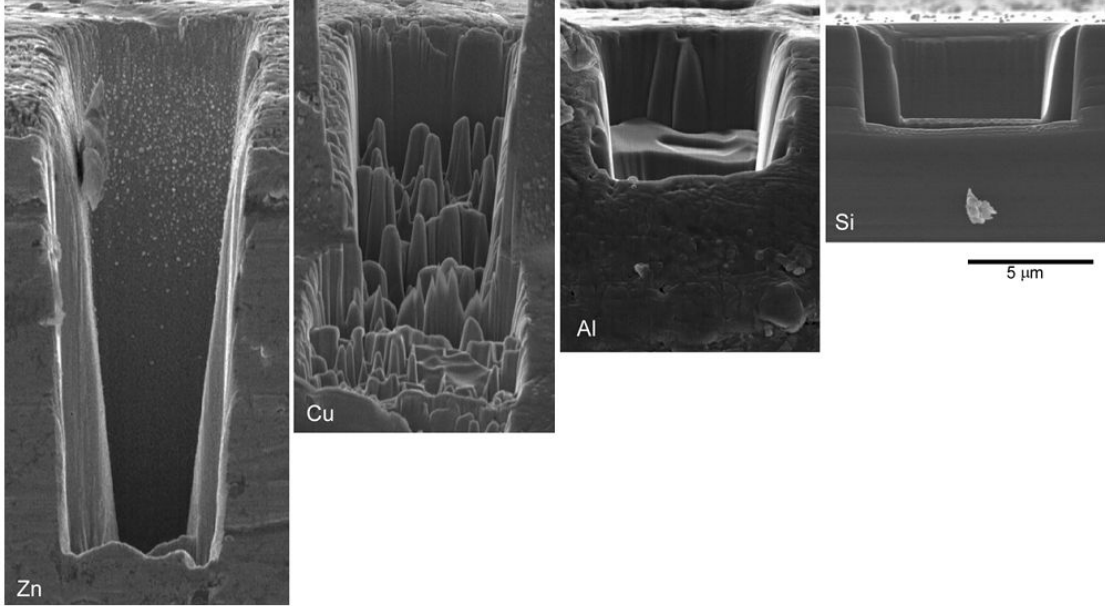
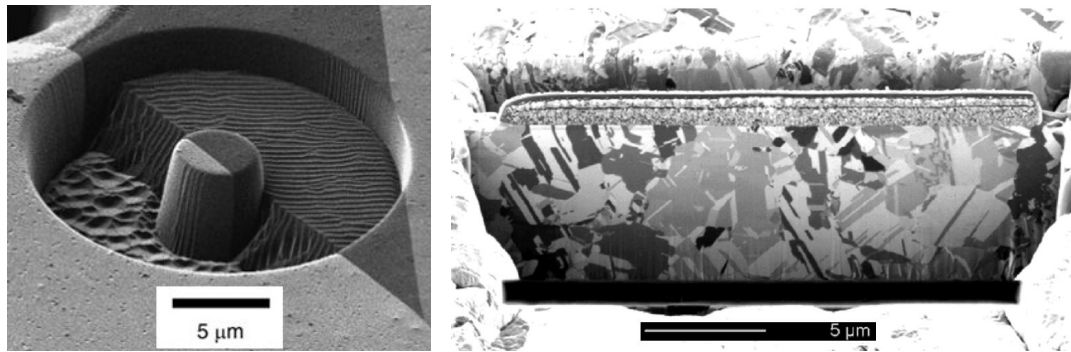


Figure 16: SEM images of FIB milled trenches. A 1 nA and 25 keV  $\text{Ga}^+$  ion beam was used with the same pattern conditions in Zn, Cu, Al and Si. This illustrates how different materials behave when milled. Taken from [12, p. 41].

When geometries with high aspect ratio are milled redeposition of sputtered material becomes of great concern. The FIB milled trenches in Figure 16 are forming a V-shape when the trench gets deep. This is a result of the competition between milling and redeposition. Redeposition rate is highest for materials with a high sputtering yield value. To avoid redeposition the sputtering rate can be reduced, the milled geometry changed to have a smaller height to width ratio or a gas that restrain the redeposition process can be introduced. The sputtering rate is easiest reduced by regulating the incidence angle of the ion beam or reducing the ion beam current. Introduction of a gas that restrains the milling process is another possibility.

When milling in grains with variations in microstructure and grain orientation it is hard to obtain an even sputtering rate. The lowest sputtering rates is observed



(a) Pillar milled at a Cu grain boundary.

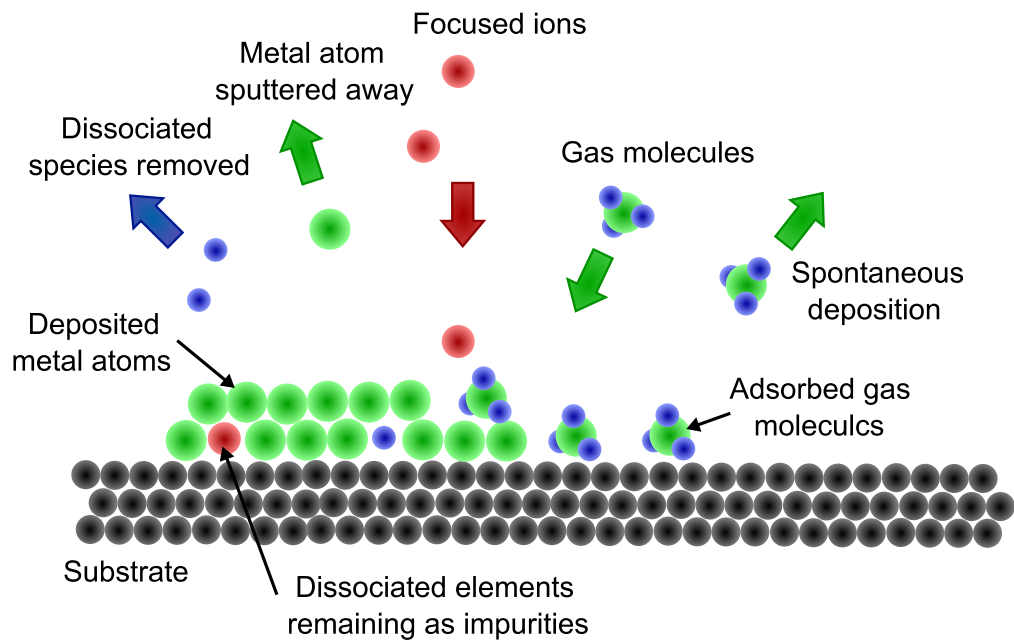
(b) Ion induced SE image of polycrystalline Cu.

Figure 17: Examples of channeling effects. Picture (a) demonstrate the difference milling properties at a grain boundary in Cu [37, p. 393]. Picture (b) shows channeling contrast image produced by ion induced secondary electrons in a FIB polished polycrystalline Cu sample [12, p. 44].

when the ion can freely move between the sample atoms, this was illustrated in Figure 13(a) and is called ion channeling. Figure 17(a) illustrates the same effect during milling at a grain boundary in a Cu sample. The ion channeling effect allows to produce images with clear contrast of the individual grain present, see Figure 17(b) of a FIB polished polycrystalline Cu sample. Before milling in the polished polycrystalline Cu sample a uniform layer of FIB deposited metal is laid at the sample surface (an increased height is seen on top of the polished surface). This procedure reduces a milling rate dependent effect called the "theater curtain" effect leaving an undulating surface. Compared to the current used during imaging the milling is obtained with higher milling current in the region between 28 pA and 21 nA [7, p. 5–92].

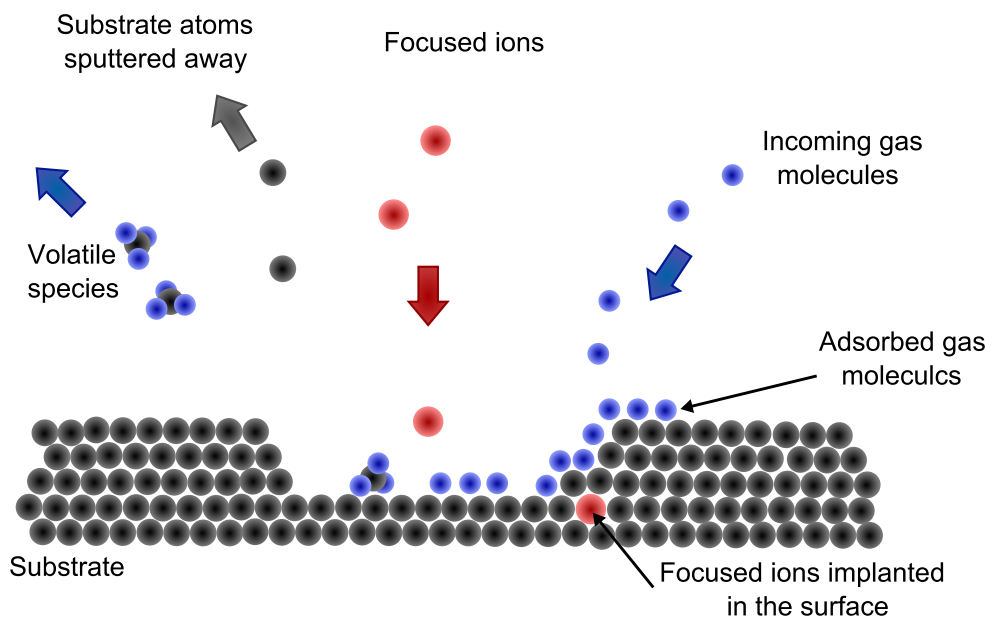
### Deposition and Etching

FIB induced material deposition and FIB enhanced etching processes are similar in several ways. A gas phase precursor is adsorbed on the sample surface. The chemical gas at the sample surface reacts with the ion beam and/or the surface material when the ion beam strikes. The produced reaction product can be more or less volatile than the sample material. For non-volatile reaction products a deposited layer will be formed if the ion beam is removed after the reaction has taken place. If the beam is not removed the reaction products will be milled away during enhanced etching. To optimize the process the chemical reaction must be understood in detail. With different sample materials the reaction can be different,



1. Adsorption of the precursor molecules on the substrate.
2. Ion beam induced dissociation of the gas molecules.
3. Deposition of material atoms and removal of organic ligands.

(a)



1. Adsorption of the gas molecules on the substrate.
2. Interaction of the gas molecules with the substrate to form volatile and non volatile species.
3. Evaporation of volatile species and sputtering of non volatile species.

(b)

Figure 18: Principal showing the (a) deposition and (b) enhanced etching process. Figures is based on pictures found in [14]



which can be taken advantage of in form of selective etching.

During use of standard FIB patterns the ion beam is scanning over an area in a raster pattern. The whole area is then scanned step wise with a predetermined pixel dwell time and step length. Typical step length is one half of the beam diameter to ensure scan overlapping. When the area is raster scanned the beam jumps back to the first point restarting the raster scan. The time of one raster scan is called the raster refresh time.

The quality of the deposition or etching process is usually determined experimentally by varying the FIB current, pixel dwell time, raster refresh time and precursor flux. The optimum parameters are then selected for the specific precursor and sample material.

For the FIB deposition the reaction products are non-volatile. To ensure a good deposition the reaction has to be as complete as possible followed by minimal sputtering of the deposited layer. In Figure 18(a) the material deposition is illustrated. The deposited layer can be a metallic deposition (W, Pt, C or Al) or an isolator ( $\text{SiO}_2$ ). The deposited layer will be contaminated with Ga and other trapped combinations.

During the sputtering process the material removal rate can be retarded or enhanced by selecting the correct precursor. For retarded removal rates the formed reaction products is non volatile and with reduced sputtering rate compared to the sample itself. The mechanism is close to the deposition process but allowing the reacting products to be sputtered away. If the formed reaction products are volatile or with higher sputtering rate than the sample material the process will be enhanced, with corresponding higher sputtering rate. Enhanced etching is a type of enhanced material removal when volatile reaction products forms, see Figure 18[b]. The sputtering rate can typical be increased by one order of magnitude by selecting the correct chemical precursor. The volatile products reduce redeposition products allowing higher aspect ratios to be obtained. Physical sputtering alone can produce unwanted topology caused by different local sputtering rate, especially in crystalline materials, that can be reduced during chemical removal. Typical used gases are  $\text{Cl}_2$ ,  $\text{Br}_2$ ,  $\text{I}_2$ ,  $\text{XeF}_2$  and  $\text{H}_2\text{O}$  [12, pp. 63–70].

### 2.3.2 FIB Preparation of Material Specimens for Loading

In the literature there exists a large variety of FIB prepared tensile, compression and bending specimens. Some of the testing is related to the micro electro mechanical systems (MEMS) where the reduced component sizes have been followed by testing at corresponding reduced length scale. A introduction to mechanical property issues in such devises is found in [1, 8]. Mechanical testing and properties for monotonic, fracture, fatigue and creep are reviewed. Important related issues are the size effect and environmental effects.

In this part the FIB fabricated geometry is the subject. The specimens are typically ranging from several tens of micrometers to sub micrometer scale. Large specimens are time consuming to produce and small specimens are limited by the FIB milling resolution. For crystalline or poly phase materials the specimens can be located in a single crystal, poly crystal or poly phase sample allowing to extract deformation behavior of a specific crystallographic orientation or determine grain boundary effects. Two types of test geometries are discussed in the following part, compression and bending specimens.

### Compression Specimens

Three selected compression geometries can be seen in Figure 19. The most used type is the circular cross section geometry, marked as B in Figure 19, often referred to as pillar or column. Examples of literature with circular pillar geometries can be found in [17, 27, 34, 35, 36]. Quadratic cross section geometries are frequently used, as examples [18, 19] are worth mentioning. This quadratic specimen is illustrated in Figure 19 marked as A. The rectangular cross section specimen marked, as C in Figure 19, was purposed by Uchic and Dimiduk [34] as a extension of the compression specimens to explore the geometrical effect. Trough this work the experience on such rectangular cross section specimens are unknown.

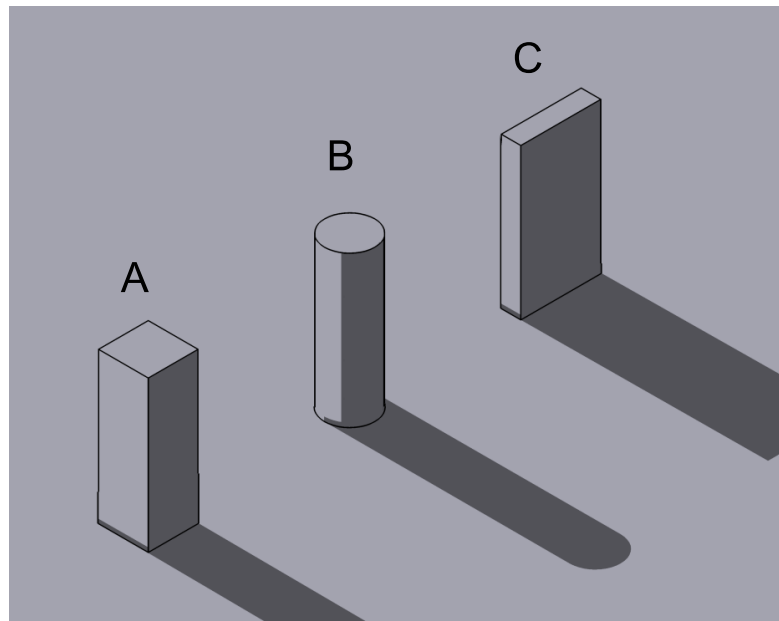
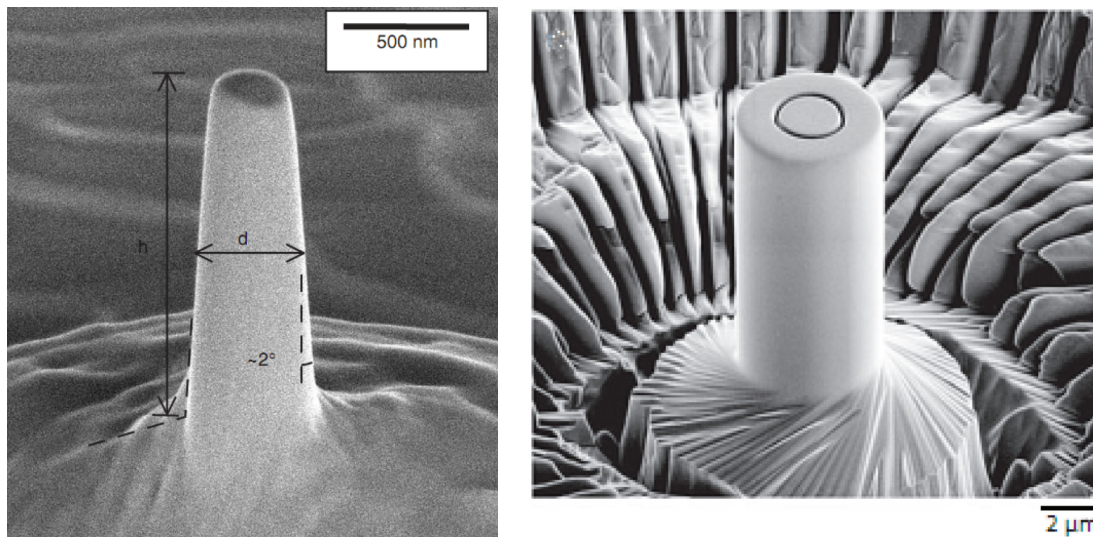


Figure 19: Examples of three compression specimen geometries. A has quadratic, B circular and C rectangular cross section.

The most investigated circular cross section geometry will further be in focus.

The pillar compression specimens can be milled with a FIB beam perpendicular to the surface (Figure 20(a) [36, p. 5570]) or with a lathe milling method where the beam is oblique to the surface (Figure 20(b) [35, p. 363]). Pillars milled perpendicular to the sample surface are easy and fast to produce but result in a varying cross section diameter and a taper angle as seen in Figure 20(a). For a pillar with a height to diameter ratio from 2 to 3 the taper angle is usually ranging from  $2^\circ$  to  $5^\circ$  [35]. Control of the pillar height is another challenge especially when milling in materials with polycrystalline or poly phases where the milling rate is varying within the pillar. Loading of tapered pillars leads to a non uniform applied stress field within the sample that results in an inhomogeneous deformation, which result in inaccurate flow stress determination and an affected high strain hardening rate [35, p. 364].



(a) Pillar milled with FIB beam perpendicular to the surface. Taper angle is about  $2^\circ$ .

(b) Pillar milled by lath milling.

Figure 20: Pillar milled by using (a) FIB beam perpendicular to the surface and (b) using lath milling method. Pictures are respectively taken from [36, p. 5570] and [35, p. 363].

A lot of the problems concerning tapered pillars is reduced by fabricating cylindrical pillars, see Figure 20(b). The lath milling method allowing this was presented by Uchic and Dimiduk [34] and secure a uniform cross section and a controlled pillar height. This way to produce pillars is more time consuming and limits the pillar dimensions to larger than about two micrometer in diameter. Another advantage is the ability to mill in specimens with difference in milling properties,

which is true for polycrystalline or poly phase materials [34, 35].

The micro compression testing has been done on a range of single and polycrystalline metals, both pure metals and alloys. For the pure single crystal metals with face centered cubic (FCC) lattice like Au, Cu, Ni and Al has been tested [35], and recently the body centered cubic (BCC) metals W, Mo, Ta and Nb as well [27]. The pillar yield strength is of both FCC and BCC metals increasing when the diameter decreases. The relationship is scaling as a power law:

$$\sigma_y = Ad^{-n} \quad (2)$$

For FCC pillars the power law exponent ( $n$ ) is ranging between 0.6 and 1 and the BCC pillars from 0.22 to 0.45 [27]. A number of models to describe the pillar size effect has been addressed for the FCC pillars [18] and a promising correlation between  $n$  and dislocation mobility in form of a critical temperature [27].

### Cantilever Bending Specimens

A large variety of cantilever bending experiments have been done at micro cantilevers in the literature. The experiments include cantilever deflection to determine elastic, yield or deformation behavior. Prenotched or precracked cantilevers are tested to determine fracture or deformation behavior close to the notch. The prenotched cantilever specimens will be the main focus in this section.

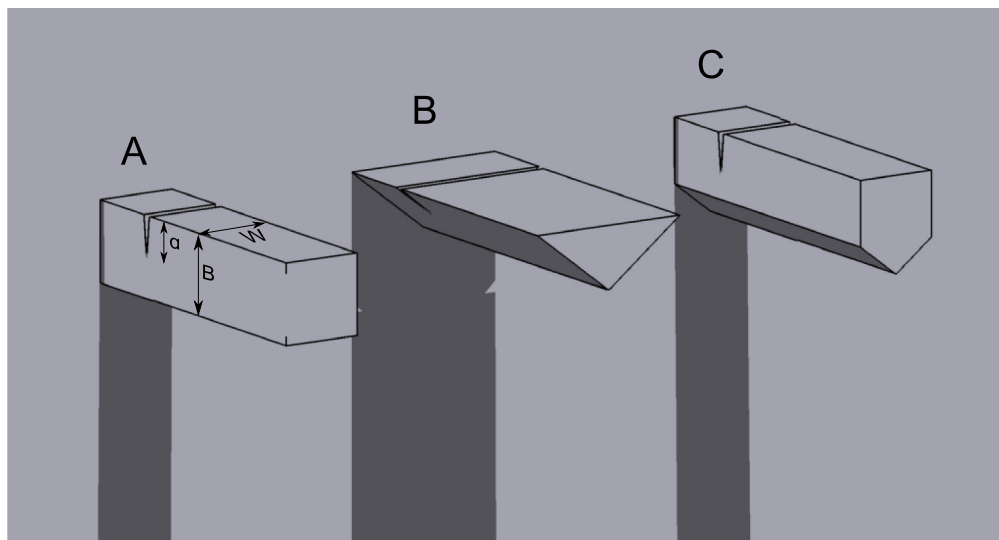


Figure 21: Examples of three fracture mechanical (FM) specimen geometries. A has a quadratic cross section, B has a isosceles triangle cross section and C is a combination of A and B aiming to be approximately quadratic.

Three of the frequently found cantilever geometries are illustrated in Figure 21. The quadratic cross section geometry is used by [22, 31, 32, 33, 39] and is marked with A in the figure. The geometry is usually produced from a thin film with the same beam height ( $B$ ) or dept ( $W$ ) as the finished cantilever, reference [22] has another approach. Such quadratic cantilever geometries should be possible to produce at the sample edge. Geometries B and C have respectively triangular [6, 13] and pentagonal cross sections [3, 40]. This geometry is often preferred since they easily can be made from the sample surface.

The quadratic geometry has a geometry close to the traditional fracture mechanical test samples. Stress intensity solution for the quadratic geometry is given in Equation (3) and (4) [2, p. 348] and is used to calculate fracture toughness values.

$$K_I = \frac{M}{BW^{3/2}} f\left(\frac{a}{W}\right) \quad (3)$$

$$f\left(\frac{a}{W}\right) = \frac{6\sqrt{\tan \frac{\pi a}{2W}}}{\cos \frac{\pi a}{2W}} \left[ 0.923 + 0.199 \left\{ 1 - \sin \frac{\pi a}{2W} \right\}^4 \right] \quad (4)$$

The momentum ( $M$ ) at the notch or crack is easy calculated by multiplying the applied force by the distance between the loading point and crack. Fracture toughness determination of brittle coatings [40] or passivation films [22] gives good measurements.

Takashima *et al.* [31] tested a more ductile Ni-P amorphous alloy thin film to determine the fracture toughness and the anisotropic mechanical properties. The loading was performed by a homemade devise similar to a nanoindenter. To obtain the fracture toughness the plane strain criteria in Equation (5) must be satisfied. If the plane strain criteria is not fulfilled a provisional fracture toughness ( $K_Q$ ) might be obtained for the specific geometry.

$$a, W, B - a \geq 2.5 \left( \frac{K_{IC}}{\sigma_{ys}} \right)^2 \quad (5)$$

The effect of notch radius was discussed by Takashima *et al.* [31]. Cantilever specimens with notch radius of 0.25  $\mu\text{m}$  and grown fatigue cracks [32] were compared. The precracked specimens failed at lower force than the only notched specimens. Fracture at lower loads for the fatigue cracked specimens indicates that there is an effect in the crack sharpness or due to change in material properties at the FIB milled notch. The fatigued crack grows trough the FIB effected layer and into a material that is unaffected by the FIB milling.

Another investigation of Fe-3%Si was done by Taki *et al.* [33] where millimeter sized specimens was compared to micrometer cantilevers. The material is known

to fracture brittle along cleavage plane (100) and the notch was set parallel to this plane. During the production of fatigue precrack the millimeter sized specimen fractured brittle at a fatigue fracture toughness of  $7 \text{ MPa}\sqrt{\text{m}}$ . The micro sized specimens all fractured ductile, something that supports that there exists a brittle to ductile transition when the dimensions are reduced. Assuming plane stress condition at the crack tip the plastic zone for the millimeter sized specimen can be calculated to  $90 \text{ }\mu\text{m}$  by using Equation (6).

$$r_p = \frac{1}{\pi} \left( \frac{K}{\sigma_y S} \right)^2 \quad (6)$$

For  $1.6 \times 2 \times 11.4 \text{ mm}^3$  specimen this satisfies small scale yielding, but for the  $10 \times 10 \times 50 \text{ }\mu\text{m}^3$  sized cantilever plastic deformation occurred through the hole cross section leading to ductile fracture.

Corresponding micro fracture mechanical tests of steel materials have not been found in the literature during this work. The expected plastic behavior might be one of the reasons for this. A way to investigate the elastic plastic fracture behavior is to measure the crack tip opening displacement (CTOD) of the specimen during loading. There exist other methods to determine the crack growth during loading and from that estimate the CTOD. An example of such a method is to measure the electrical resistance through the specimen. When the cross section beneath the crack changes an increased electrical resistance is measured. The unloading compliance method is another approach where the specimen is partly unloaded at frequently intervals during the loading test. The slopes are a measure of how stiff the specimen is. When the crack starts to grow the slope will decrease indicating that the specimen has become more compliant (less stiff). The unloading compliance technique is less sensitive for  $a/B < 0.5$  [2, p. 323].

Examples of other similar experiment performed at micro sized cantilevers of a 304 austenitic stainless steel are presented in [39] and [3]. Zhang *et al.* [39] investigates the fatigue strength of an unnotched cantilever produced from a thin film while Armstrong *et al.* [3] determine the effect of stress corrosion cracking of individual grain boundaries.

The tip used during the testing is a variation between flat ended, spherical and Berkovich tip. Sharp tips will penetrate into the sample while flat ended tip makes it harder to determine the exact loading point.

## 2.4 SEM Compatible Metallographic Techniques

The scanning electron microscope (SEM) has been rapidly accepted in several laboratory disciplines the last decades. The rapid acceptance caused by the wide availability of SEM, ease of sample preparation, fast data acquisition and the access

to complementary information about the microstructure at submicron resolution. Secondary and backscatter electron images provides topography and orientation contrast details, while x-ray energy-dispersive spectroscopy (XEDS) and electron backscatter diffraction (EBSD) gives consequently information of the element distribution and crystallographic information [28, p. 1]. This section will go into the principal of these two metallographic techniques.

### 2.4.1 X-ray Energy Dispersive Spectroscopy

To precisely determine the chemical composition of a sample some of the phenomena involving the local atomic number ( $Z$ ) must be used. The x-ray energy dispersive spectroscopy (often shortened to XEDS, EDX or EDS) involves the energy-shell structure of a atom. The Bohr model of the atom gives a scientific description of the electron-shell structure [10, p. 155], where the electrons are locked to a number of defined orbit radiuses around the nucleus. The electron orbit or electron shell closed to the atom nucleus is called the ground shell and has the lowest energy electrons in the atom. Ground shell is labeled as K and shells with increasing radius from K are denoted L, M and so forth (see Figure 22 [38]) [10, p. 156].

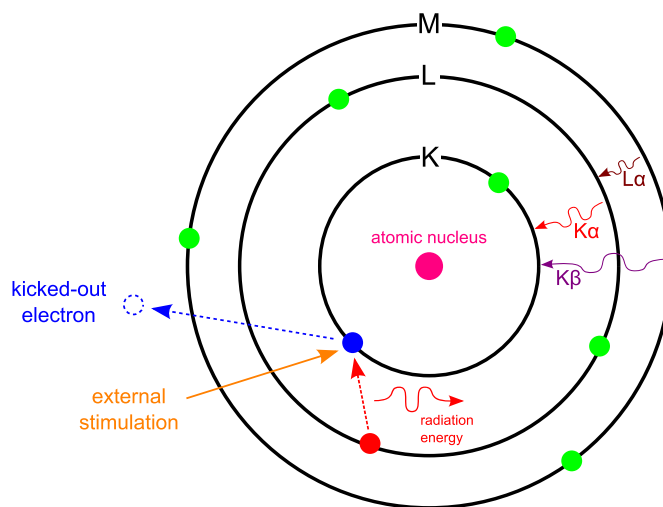


Figure 22: Illustration of the atom with its nucleus and three electron shells K, L and M, out from the center. If an electron in one of the inner shells is stimulated by for instance an incoming electron it might absorb energy and excite to an orbit further away with a higher energy level. This leaves the inner-shell with an electron vacancy that very soon will be filled by an electron that de-excited from a higher energy shell. During the de-excitation the electron must emit a well defined amount of photon energy. Figure is taken from [38]

The Bohr model provides an explanation of the energy differences between the allowed orbits or energy levels. By absorbing a quantized amount of energy the electron can excite to an orbit further away from the nucleus with a higher energy level. In a similar manner a electron can lose a well defined amount of energy by emitting a photon and place oneself in a orbit closer to the nucleus and with a lower energy amount. The electron energy emission, or de-excitation process, might happen in several step length for atoms having several defined shells [10, p. 157]. A de-excitation from the L- to the K-shell is denoted  $K\alpha$  indicating that the jump happens to the K-shell from one ( $\alpha$ ) shell away. If the jump happens two or three shell away the annotation would respectively be  $K\beta$  and  $K\gamma$  after the Greek alphabet.

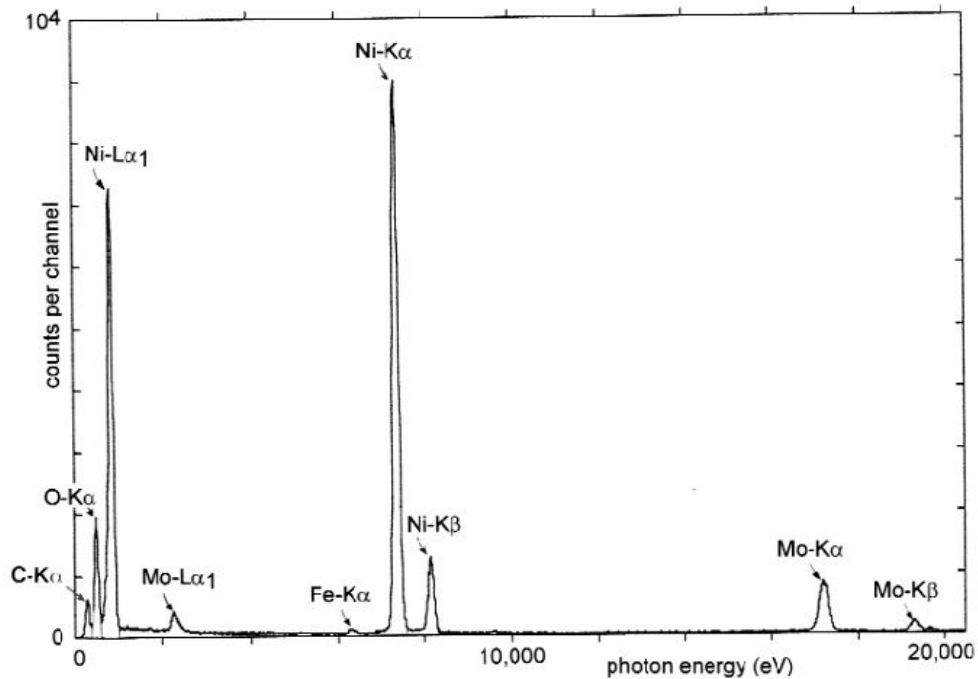


Figure 23: Characteristic x-ray emission energy spectrum from a TEM sample. The sample is a NiO film deposited on a thin C film on a Mo grid. Characteristic peaks due to the elements C, O, Ni, Mo and Fe are found. The figure is attained from [10, p. 159].

When an electron from the SEM enters a specimen it might be scattered inelastically by an inner-shell electron. This can cause the inner-shell electron to undergo a transition to a higher-energy orbit, leaving the inner-shell with an electron vacancy, or electron hole. Within about  $10^{-15}$  s one of the other electrons in



the atom de-excited to fill the vacancy. During the de-excitation a characteristic x-ray photon with a well defined energy emits. The x-ray energy is defined by  $Z$  and the involved shells. For most of the elements the photon energy is above 100 eV and lie in the x-ray region of the electromagnetic specter. The exception it H, He and Li [10, p. 158]. Figure 23 [10, p. 159] shows an x-ray emission spectrum from a transmission electron microscopy (TEM) sample. The sample consists of a thin nickel oxide (NiO) film deposited onto a thin carbon film supported by a molybdenum (Mo) grid [10, p. 159]. X-rays detected for Ni (Ni-L $\alpha_1$ , Ni-K $\alpha$  and Ni-K $\beta$ ) is characteristic for the same three de-excitations illustrated in Figure 22. For oxygen and carbon only one characteristic photon energy is indicated, respectively O-K $\alpha$  and C-K $\alpha$ . The Mo peaks (Mo-L $\alpha_1$ , Mo-K $\alpha$  and Mo-K $\beta$ ) are arises from the TEM grid material and Fe peak (Fe-K $\alpha$ ) is caused by the TEM pole pieces [10, p. 159].

The spectrum in Figure 23 illustrates several features of the XEDS detection. Each element has at least one characteristic peak with defined photon energy. Elements with low  $Z$ -values have often one peak, while higher  $Z$ -value corresponds to several peaks. For spectrum analysis where some of the peaks overlaps each other this is an adequate quality that makes the analysis possible. Ideally the recorded spectrum is defined by the electron beam and the excitation volume at its focus point. Unfortunately stray electrons outside the focus point will always affect the nearby environment [10, p. 160]. Generated x-ray photons beyond the probe region might come from holders or the pole pieces [10, p. 164]. A continuous "bremsstrahlung" background is produced from the excitation volume. This is visible between the characteristic peaks and is ranging across all the energy levels [10, p. 160].

The dispersive device in XEDS is usually a semiconductor diode from a single crystal. When the x-ray photon penetrates to the transition region, between the doped diode materials, it results in electrical conductivity for a brief period of time. The conductivity depends on the x-ray photon energy and allows a current to pulse when a bias voltage is applied [10, p. 161]. To minimize the electrical noise in the diode it is cooled to about 140 K. The cooling is done by coupling the diode to an insulated vessel of liquid nitrogen (77 K) via a metal rod. To protect water vapor and hydrocarbon molecules to condense into the cathode diode a thin window is protecting the diode. The current pulses from the Si diode is amplified and [10, p. 162] the hits are recorded to a set of channels. Typically each channel corresponds to 10 eV range of photon energy and ranges from 0 to 40 keV. Each characteristic peak has a smooth profile caused by statistical variation and have a typically width of 150 eV [10, p. 163].

To detect each peak in the spectrum a significant number of photons must be detected. If the element concentration is going to be measured with 10 %

accuracy, at least 100 hits must be detected for every peak. The record time for a point is typically from about 10 s to several minutes. A quantitative estimate of the concentration ratios are done during these steps:

- The peak areas for every peak in the spectrum are calculated.
- Bremsstrahlung background is measured between the peaks and subtracted from the peak areas.
- Since different materials do not emit equally x-ray ratios [10, p. 165] this is corrected for by comparing peaks in pairs and correct the values with predefined peak intensity ratios [10, pp. 166-167]. The most correct intensity ratios must be determined from standard samples, with known composition ratios, in the available instrument.
- When the composition is predefined a correction of the x-ray absorption and the x-ray fluorescence is corrected for in a iterate process. This ZAF-correction is done by a ZAF program and the x-ray emission spectrum can be displayed [10, p. 167].

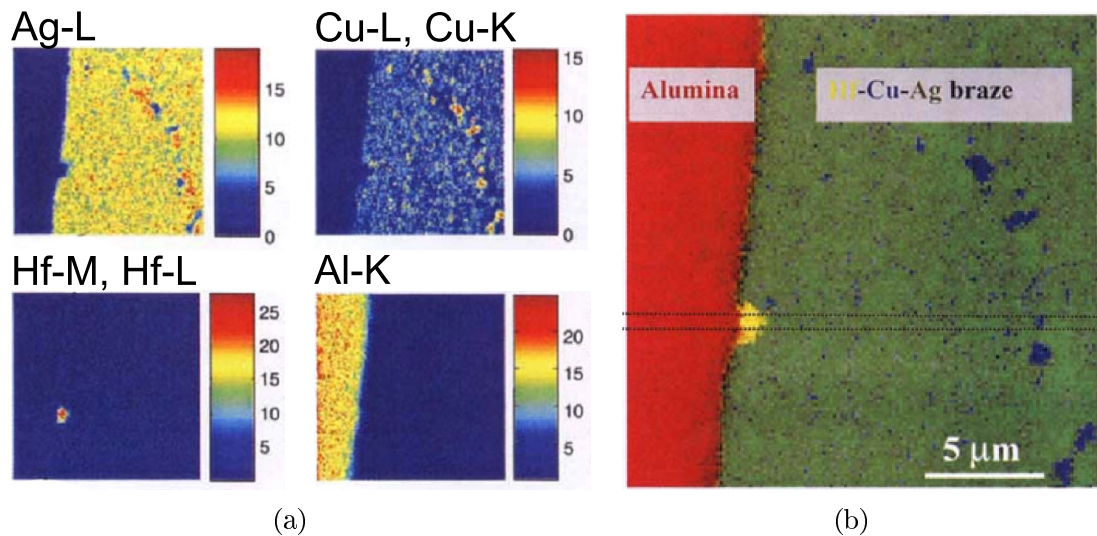


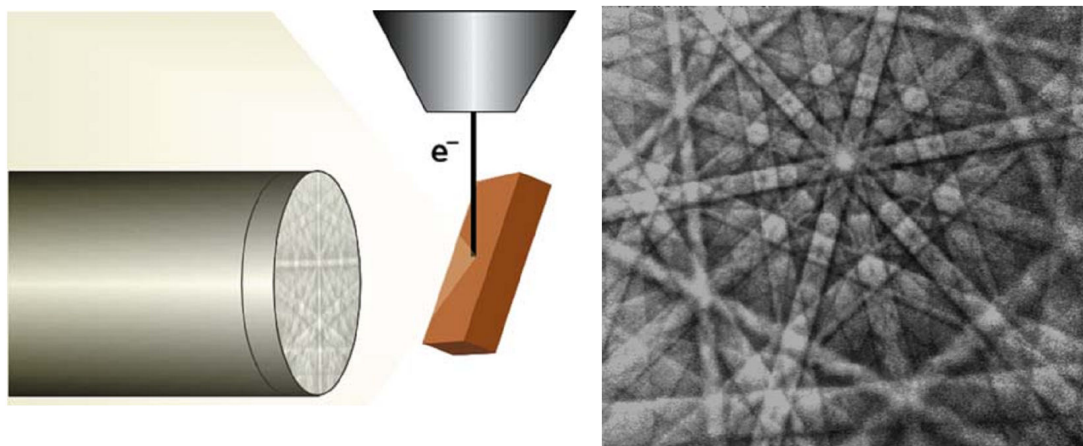
Figure 24: X-ray spectral image analysis of (a) separate elements and (b) combination of all the detected elements. The scale in (a) is the detected amounts of the elements. Pictures is taken from [21, p. 56].

During the steps above the composition of a point in the specimen can be estimated. Doing this for a raster scanned surface area it reveals the differences in

local composition. A comprehensive way to represent the x-ray spectral analysis is to plot the element separate as an image. Figure 24(a) [21, p. 56] shows an example of a transition between alumina and Hf-Cu-Ag, where the Hf-Cu-Ag alloy was brazed onto the alumina sample. The information can be compressed into one image by giving every element a color. Figure 24(b) [21, p. 56] shows such an example where the highest estimated element amount gets its color in the image. The color image might be combined with a SEM image from the same region or combine the overlapping detected elements to form new color combinations [11].

### 2.4.2 Electron Backscatter Diffraction

A well suited method to characterize orientation and phases of a crystalline material is the electron backscatter diffraction (EBSD). The automated characterization can be done by directing a stationary high energy electron beam into a crystalline sample and detect the backscattered electron diffraction on a phosphor screen. The backscatter diffraction pattern (EBSP) generated at the phosphor screen has an arrangement of parallel bright bands on a continuous background. The principal setup of the EBSD system with use of a SEM column is presented in Figure 25(a) [28, p. 4] and a EBSP, or backscatter Kikuchi pattern, produced from a cadmium sample using a 20 keV electron beam is seen in Figure 25(b) [28, p. 2]. By analyzing the backscatter Kikuchi pattern the crystallographic phase and orientation can be determined.



(a) Setup for the electron backscatter diffraction (EBSD). (b) Kikuchi lines, or electron backscatter diffraction pattern (EBSP), from a cadmium sample.

Figure 25: Picture of (a) the schematic EBSD setup and (b) EBSP from a cadmium sample, taken from [28, pp. 3–4].

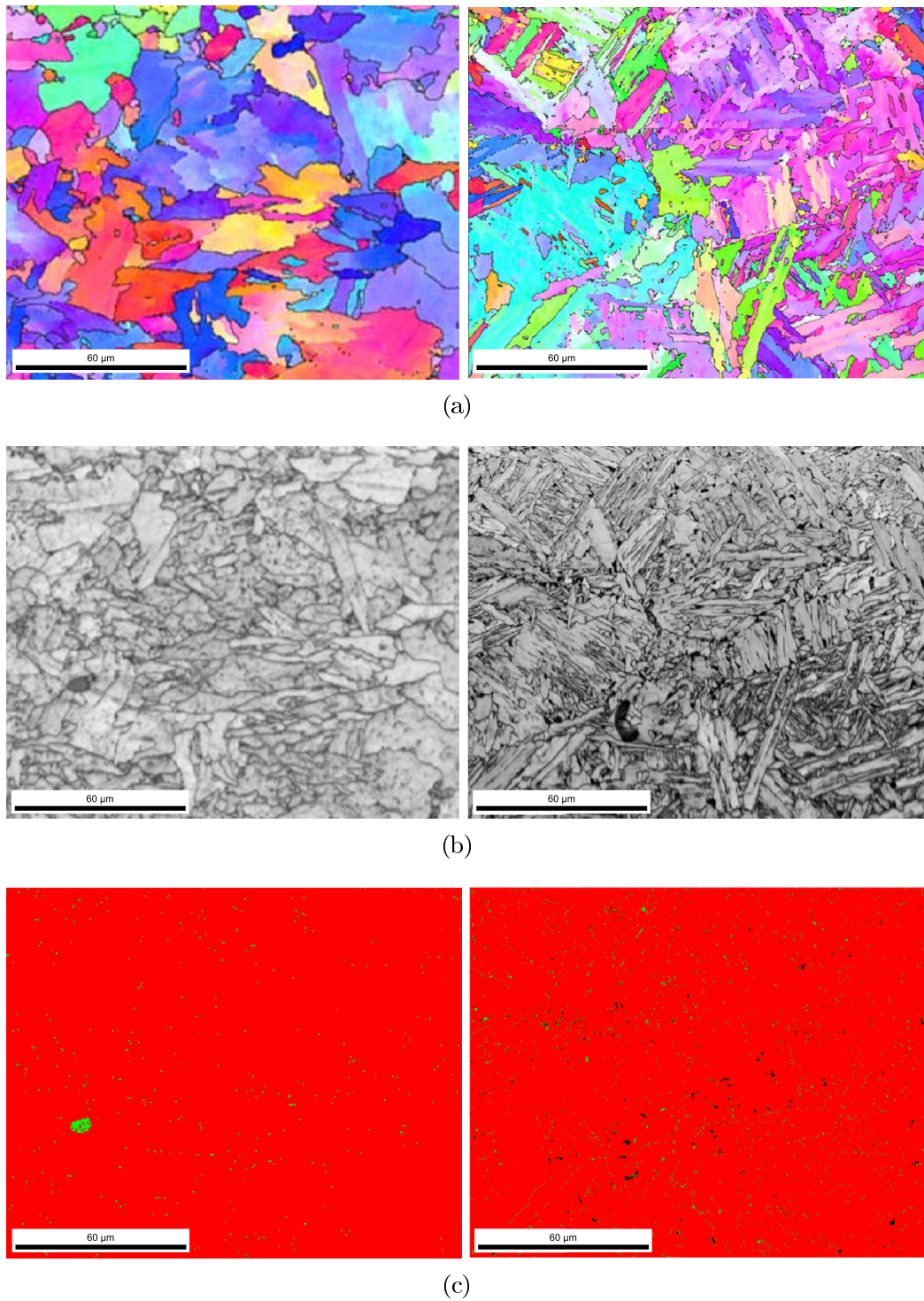


Figure 26: Picture of (a) IPF map (b) IQ map and (c) Phase Map produced in a SEM. The left side is from the base metal [5, pp. 33] and right side is a two cycled weld simulated IC CG HAZ microstructure [5, pp. 37–38]. The same area is displaced in (a), (b) and (c).

During the EBSD characterization the stage and sample surface is highly tilted relative to the incoming electron beam, usually about  $70^\circ$ . This ensures the best backscatter diffraction towards the phosphor screen. The SEM acceleration voltage is directly coupled to the electron wavelength and the EBSP. A low beam voltage gives thin bands in the EBSP.

Beam and sample interaction happens in a small volume at the sample surface and has a lower resolution than the SEM produced image of the same surface. In practice this limits the automated EBSD to materials having a grain size larger than several tenths of nm. The sample should in general be sufficient flat, the surface strains must not be excessive and fulfill SEM requirement.

The location of the transparent phosphor screen detecting the backscattered electrons is in the region of 2 cm from the sample and has a diameter of around 5 cm. As indicated in the principal sketch in Figure 25(a) the screen preferably stands parallel to the incoming electron beam and is capable of minor rotation out or in of the picture plane. The phosphors screen illuminates by the electrons and the lights is viewed with a high sensitivity camera or coupled trough fiber optic bundles, which directs the light to camera sensors [28, ch. 1].

A surface sample area is scanned and mapped in a stepwise pattern. The scan is done by moving either the stage or raster the electron beam. Every point is indexed and the crystallographic information is stored together with parameters describing the index quality (confidence index, image quality and fit). In Figure 26 a set of EBSD maps from the 420MPa Arctic steel quality used in this work is showed. The EBSD pictures are from the base metal plate (left side in subfigure (a),(b) and (c)) found in [5, p. 33] and a two cycled weld simulated sample (right side in subfigure (a),(b) and (c)) microstructure taken from [5, pp. 37–38]. The two cycled weld simulated sample is producing the IC CG HAZ microstructure.

Figure 26(a) shows a crystal orientation mapping of the microstructure. For every pixel in the image the crystallographic orientation is determined and colored according to an inverse pole figure. The inverse pole figure is given in bottom left corner in Figure 27. From the same information the grains and grain boundaries can be defined when a selection of neighbor pixels excides a threshold value. The miss orientation angel defining a grain is usually set to around  $\sim 3^\circ$ . Figure 26(b) is a image quality (IQ) map of the same microstructure. Light parts corresponds to EBSP with clear Kikuchi bands and hence a good indexing. Dark parts are caused by grain boundaries, impurities or surface strains that reduce the indexing quality. The last Figure 26(c) is a phase map of the surface clearly distinguish the faces from each other. The small spots of green colored austenite are easy to distinguish from the surrounding red colored ferrite.



## 2.5 Three Dimensional Reconstruction

Three dimensional (3D) mapping of a microstructure gives a basis to better understand the microstructure and thereby material properties [28, p. 109]. A common way to 3D characterize a sample is by serial sectioning. The surface of interest is prepared and recorded with an appropriate microscopy technique. A thin slice of the surface is then removed, and prepared if necessary, so that the new surface can be recorded. The slicing and recording is repeated until a number of 2D images are representing a 3D volume [28, p. 109]. Software for 3D data analysis can be used to analyze and display the data.

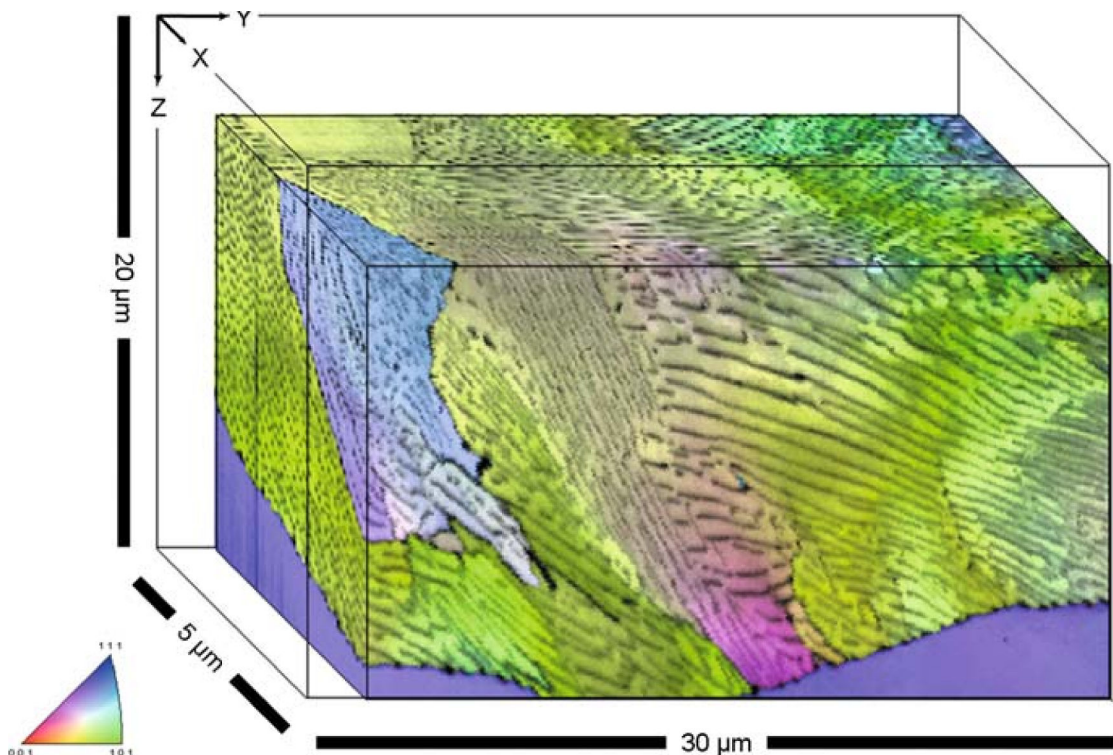


Figure 27: 3D orientation map of a pearlitic microstructure. The image is a combination of the image quality and color coding for the crystallography direction parallel to the sample x-axis. The figure is taken from [28, p. 115]

The 3D characterization can be done by using light microscopy observations, electron microscopy observations or other appropriate methods. Serial sectioning with a use of a FIB/SEM dual beam system has several advantages if they are compared to other serial sectioning methods that are more manually. The sectioning, with precision down to few nanometers, and imaging can be done in the same rigging without manually handling during the characterization [28, p. 110].

The characterized volume during FIB sectioning is varying from some  $1000 \text{ nm}^3$  to several  $\mu\text{m}^3$  with a 30 kV  $\text{Ga}^+$  ion beam. In a dual beam system the produced image can range from electron induced secondary electrons, backscatter electrons, ion induced secondary electron, ion induced secondary ions, element analysis in form of XEDS or crystallographic EBSD analysis. Most of the image modes include sectioning followed by stage tilt or rotation to the imaging position and a backward motion to the sectioning position.

The EBSD representation of the serial sectioning has sowed advantages during the 3D volume reconstruction and analysis of crystalline materials. The crystallographic information allows small misalignments between the images, occurred from the stage motion, to be corrected for [28, p. 112]. The 3D information can be analyzed to reconstruct 3D grains and 3D grain boundaries. Software tools to select a grain and obtain information about volume, shape, size and so on are available [28, p. 113]. In Figure 27 [28, p. 115] 3D orientation map of a perlite microstructure from a high carbon steel sample is showed. The 3D orientation map has been reconstructed from 50 slices of  $30 \times 20 \mu\text{m}^2$  with a distance of 100 nm between the images. A automated 3D reconstruction like this takes about 29 hours [28, p. 114]. One volume pixel on the image is a combination of the image quality and the crystallographic orientation. Spots with a clear and light color have a good image quality which corresponds to a good indexing. The dark spots correspond to a bad or unindexed spot. The lamellar cementite between the ferritic microstructure is unindexed and remains as black lamella. The color coding for the direction parallel to the x-axis is given in the inverse pole figure color triangle at the Figure 27 bottom left side [28, pp. 114–115].

Automated 3D EBSD analysis allows detailed measurement of crystallographic phases and orientations in a volume. The volume pixel resolution is today about  $100 \times 100 \times 100 \text{ nm}^3$  and volumes up to about  $50 \times 50 \times 50 \mu\text{m}^3$  are obtainable [28, pp. 120–121]. The EBSD camera development has lately reduced the pattern acquisition rate from 70 patterns per seconds to almost 200 patterns per seconds which reduces the reconstruction time drastically. The volumes characterized by this method are relative small and statistical data should be use carefully. The high resolution is the largest advantage of this method. A serious problem observed when metastabile residual austenite is FIB milled is that all austenite transforms into ferrite under influence of the ion beam [28, pp. 120–121].





### 3 Experimental Procedure

The experimental part of this work has mainly been to develop good procedures for FIB preparation and loading in the nanoindenter. A sufficient part that is less discussed, is the effort done during training in use of equipment. This experimental part of the report is explaining a useful procedure and important issues and problems related to it.

#### 3.1 Sample Material and Sample Preparation

The material used is a high strength low alloy (HSLA) steel produced by Nippon Steel with a specified minimum yield strength (SMYS) of 420 MPa. Inspection certificate from the producer shows a tested yield strength of 514 MPa and ultimate tensile strength of 606 MPa. The chemical composition is seen in Table 1 [30].

Table 1: Overview of the main chemical composition of the investigated steel [30].

Element	C	Si	Mn	P	S	Cu	Ni	Cr	Nb	N
wt %	0.09	0.19	1.54	0.004	0.002	0.28	0.72	0.02	0.013	0.035

In the experiment base metal plate and a heat treated sample were used. The samples were received from master student Svein Astad that carried out heat treatment, Charpy impact test and metallurgical investigation of this and other heat treated samples during his project work [4]. Light microscopy image in Figure 28(a) shows the base metal plate which has a fine grained acicular ferritic microstructure with small islands of bainite and martensite. Segregation in the material can be seen as bands of more frequently bainite and martensite islands. Left side of Figure 26 supplements with EBSD characterization of the same base metal done during project work by master student Olav Bjering [5]. Macro hardness testing of the base metal sample showed a Vickers hardness of 178HV [5, p. 32].

The heat treatment consists of two parts. First part is done with a Smitweld TCS 1405 that simulates a weld cycle with a heating velocity of 150 °C/s, peak temperature of 1350 °C and cooling from 800 °C to 500 °C in 15.3 s. This cycle corresponds to a weld cycle where a coarse grained microstructure is produced, often referred to as coarse grained heat affected zone (CG HAZ). Second heat treatment was done in a Nabotherm N 17/HR stove by heating the sample to 790 °C where the sample is held in 60 s and cooled suddenly in water. When the sample is held in 790 °C parts of the grains will transform to austenitic microstructure and alloying elements diffuse into the transformed grains. After cooling the earlier austenitic grains transform to grains that includes martensite and retained austenite. The grains are referred to as MA phases or MA grains. The surrounding microstructure

is bainitic [4, pp. 15-17]. The segregation in the material results in bands of MA grains along the sample. Microscopy picture of the used heat treated sample is seen in Figure 28(b). The sample was measured to have a Vickers hardness of about 479HV.025 inside the martensitic grains and a lower hardness of 273HV.025 in the surrounding matrix [4, p. 43].

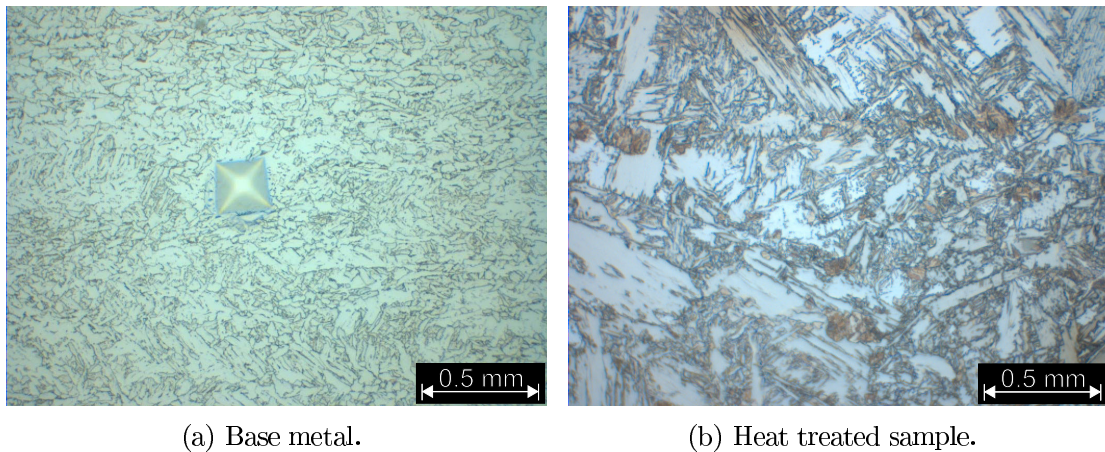
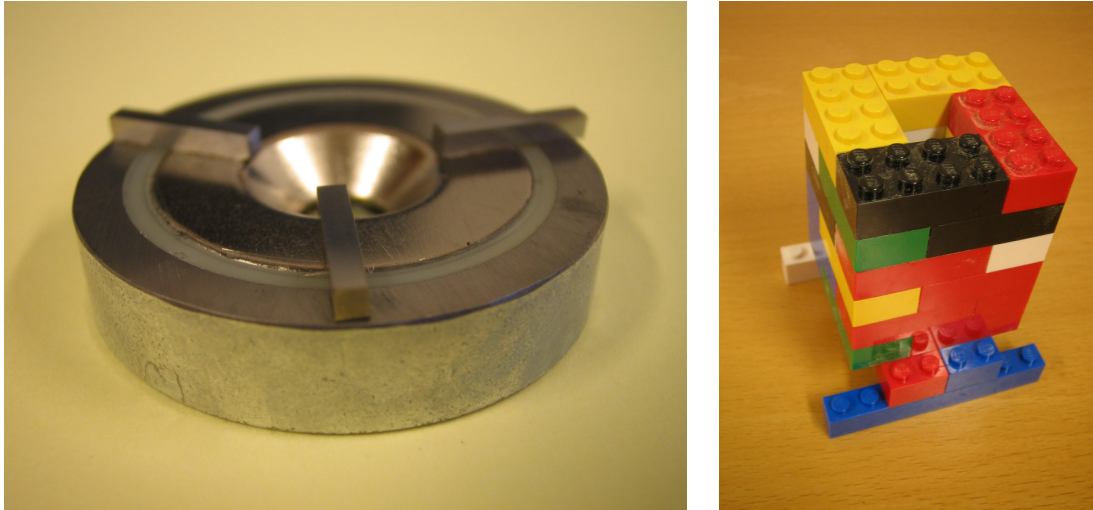


Figure 28: Light microscopy pictures of the two prepared samples. Sample (a) is from the base metal while sample (b) is the heat treated microstructure.

The standard sample holder and stub provided with the FIB was used and are showed in Figure 10 (a) and (b). The sample holders restrict the sample to a height smaller then about 1.9 mm. The desire of FIB milling quadratic fracture mechanical (FM) specimens involved to mill from two sides located perpendicular to each other. The chosen sample geometry ended up as a miniature beam whit the approximate dimnations  $1.8 \times 1.8 \times 10 \text{ mm}^3$  and supplemental specimens for microstructure investigation.

The small beams were first cut out with a thin cutting-off grinding wheel. To be able to prepare the small sized beams, by grinding and polishing, a holder or help jig was needed to carry out a proper preparation. In this case two concepts were tested out. First concept was to use a strong plane niobium magnet as a sample holder, see Figure 29(a). Second concept was to cast-in the sample using thermoset plastic. The sample is placed in a  $90^\circ$  corner of the improvised Lego mold, Figure 29(b). By doing the cast-in the sample beam could be placed in a corner ready to be grinded.

The sample preparation was done manual by grinding and polishing in several steps. The polishing had diamond particles down to a size of  $1 \mu\text{m}$ . The etching was done with a 2 % Nital in 15 to 20 s. The prepared samples that was used later are listed in Table 2.



(a) Plane grinded niobium magnet with three beam samples attached. (b) Improvised mold made of Lego.

Figure 29: Sample holder concepts to be able to do the grinding and polishing of the samples. Concept (a) uses a magnet to hold the sample while concept (b) uses a quadratic Lego mold. Placing the sample into a sharp corner little plastic has to be grinded away. The sample resulting from the Lego mold is seen in Figure 37.

Table 2: Overview of the prepared samples used in further work.

Sample 0	Sample was prepared before the sample holder concept was tested out. Sample is grinded, but not proper polished. Used as a dummy sample. Base metal plate.
Sample I	Base metal plate.
Sample II	Heat treated sample.

### 3.2 Optimizing of FIB Specimen Fabrication

As for the sample preparation the FIB fabrication has been a combination of learning to use the dual beam system and to obtain the best results in a trial and error setting. In total it was prepared seven series of specimens of different variety. The overview is given in Table 3 linking the successful produced FIB specimens series to the prepared samples given earlier in Table 2.

Table 3: Overview of prepared FIB specimens. The specimens in pillar series 300 and FM series 200 were not completely finished.

Specimen series	Sample	Number of specimens
Pillar series 000	0	–
Pillar series 100	I	7
Pillar series 200	I	6
Pillar series 300	II	9
FM series 000	0	6
FM series 100	I	5
FM series 200	II	4

It was early established preparations of the specimens in two stages. First FIB milling with high  $\text{Ga}^+$  current to remove much material followed by low current milling. The low current milling gives a better surface result, less taper angle and introduces less Ga into the specimen surface. The selected pillar geometry is the circular type marked as B in Figure 19. The two stepped procedure for the pillar specimens is illustrated in Figure 30. In some of the cases a step pattern was used to reduce the production time.

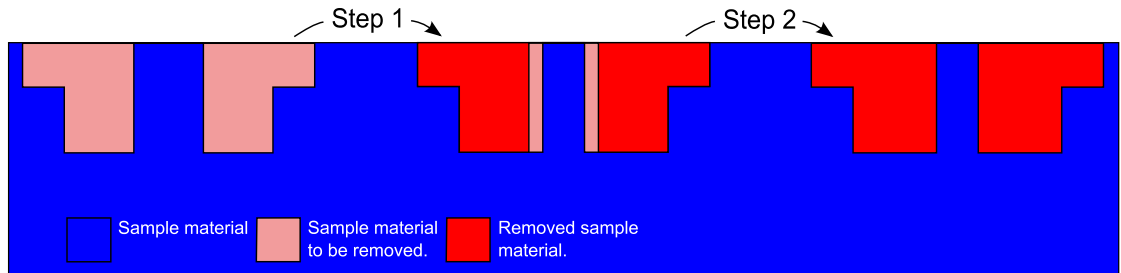


Figure 30: Cross-section drawing of the two stepped milling procedure to produce pillars. The pillars and the removed material are circular.

For the FM specimens the quadratic cross-section geometry in Figure 21, marked A, was used. This geometry is similar to the traditional fracture mechanical specimens. Specimens like this are usually fabricated from a thin film.

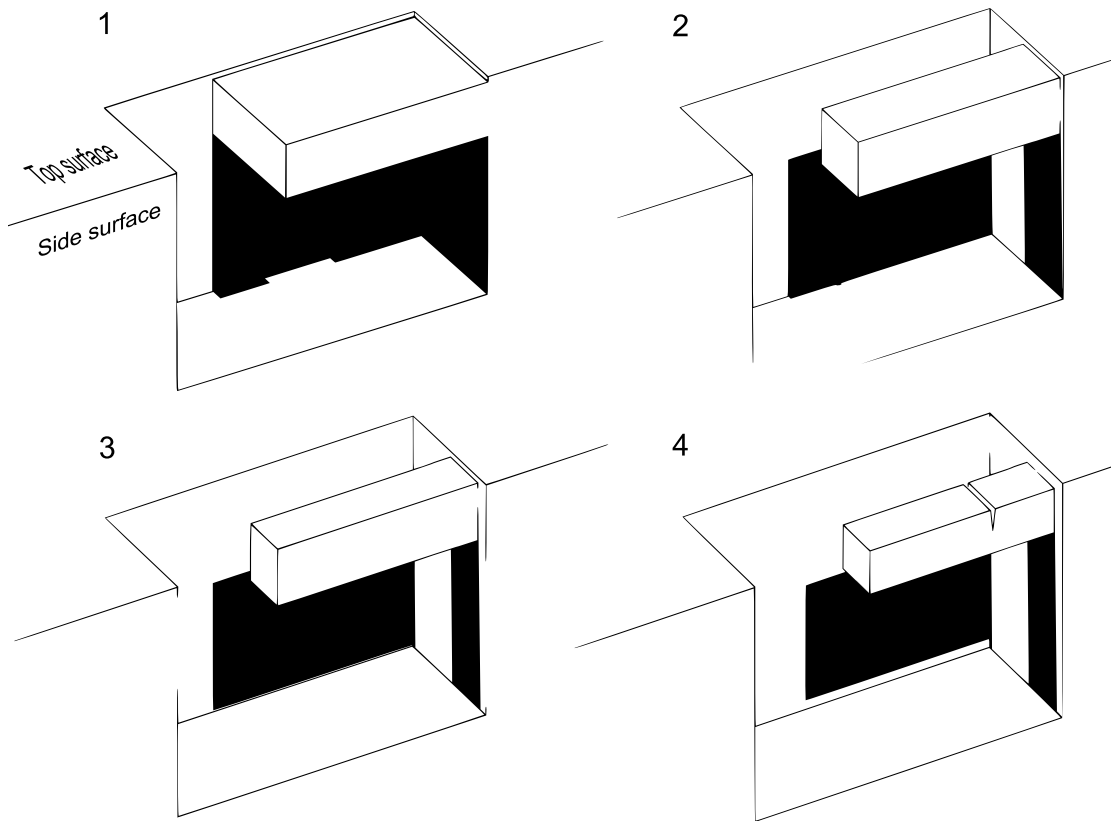


Figure 31: Steps in the quadratic cantilever FIB milling procedure. Notice the necessary milling direction to be able to perform the milling steps. In picture 1 the main material removal happens at high current and high removal rates. The ion beam is directed perpendicular to the specimen side surface. Between picture 1 and 2 the specimen is manually tilted  $90^\circ$  to allow height rate milling with a beam perpendicular to the top surface during picture 2. Picture 3 is milled with a beam from the top, but with a lower beam current to obtain more accurate dimensions and better surface finishing. The specimen is again, between picture 3 and 4, manually tilted back  $90^\circ$  and the low current milling is done from the side surface. The last step in picture 4 is to produce the crack like notch.

In this manner the fabrication can happen in one rigging. Beam geometry was used for the macro sample to examine the possibility to fabricate the cantilever specimens at the sample edge. Unfortunately this needs a manual flipping of the sample and several production steps. The four stepped procedure is visualized in Figure 31. Upper left corner of Figure 31 shows the first step where the main material removal happens. From picture 1 to 2 the sample is manually tilted  $90^\circ$  and the machining is in picture 2 happening from above with high current. After high current machining in picture 2 it is followed by a low current machining in lower left picture 3. Now the geometry is reduced to the final geometry from this direction. Between picture 3 and 4 the sample is again tilted back to the first position and the last low current material removal can happen. The last step in picture 4 is to produce the notch.

### 3.3 Optimizing of Specimen Loading

The nanoindentation testing was partly done at INM Saarbrücken and partly in Trondheim. In Trondheim a Tribo Indenter (TI 750 Ubi) from Hysitron was used. Besides the indentation capabilities the nanomechanical test system has an optic camera to locate the surface of interest. Figure 32 shows pictures taken from the optic camera during point calibration of a  $10\ \mu\text{m}$  diameter flat ended tip. Figure 32(a) is taken before the point indentation into a indium sample and (b) is after. The only difference showed is a point made by the flat ended tip, marked with an arrow in the picture. The point is used to align the tip to the optic image center.

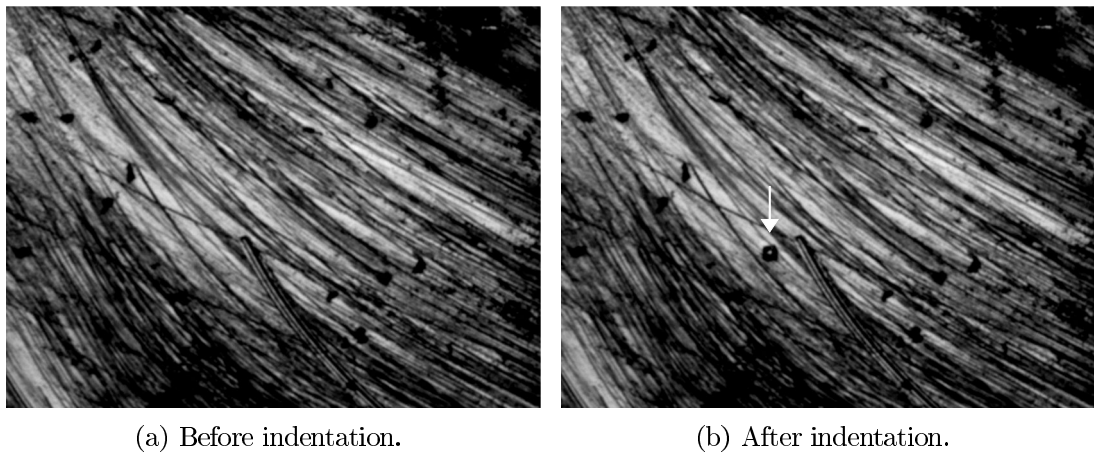
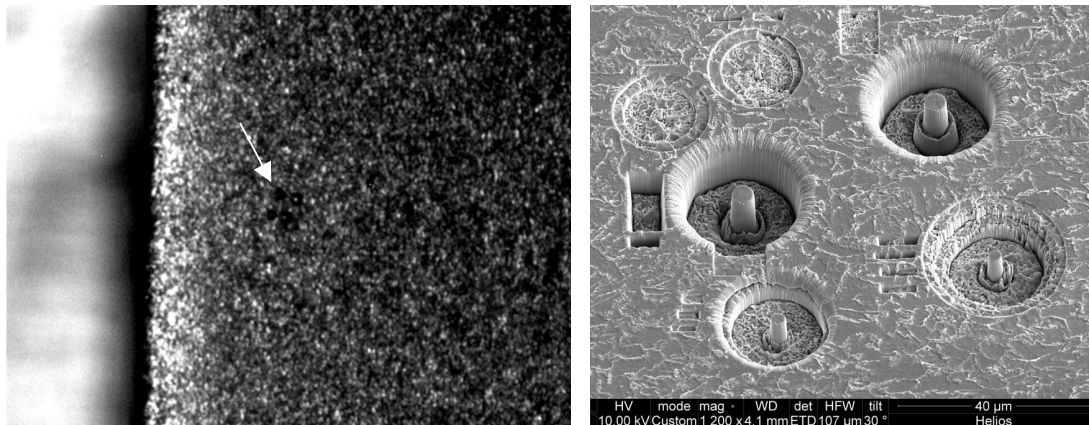


Figure 32: Optic picture taken during point calibration of flat ended tip in indium. Picture (a) is before the indetntation and (b) after. The indented spot is marked with an arrow.

The limited magnification in the optic system requires a sufficient large mark in the surface to easy locate the point of interest. A macro indentation, as in picture 28(a), can work as a identifier. When testing micro sized pillars a crater is FIB milled away around the pillar. A crater of  $30\ \mu\text{m}$  in diameter is easy to locate if the approximate location is known. Figure 33(a) shows optic picture of pillar series 200 at 5 times magnification. The same pillar group, in form of a SEM image at  $30^\circ$  tilt, is compared in Figure 33(b). Take notice of the two smallest pillars in the upper left corner of the SEM picture. The smaller pillars are hard to find in the optic camera picture.



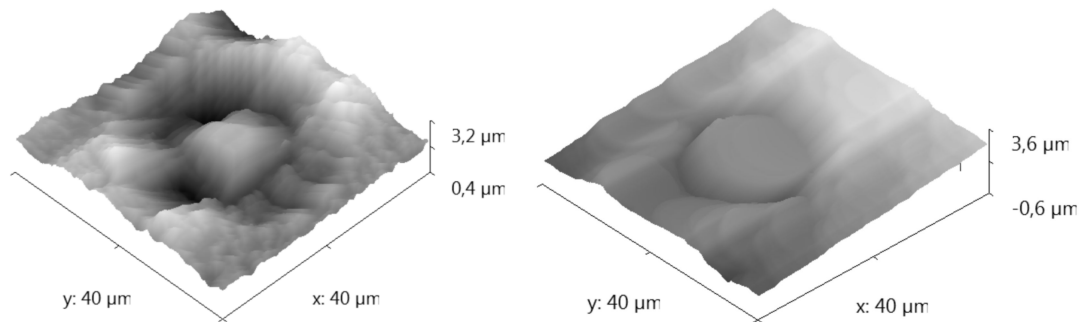
(a) Optic picture of pillar series 200.

(b) SEM image of the same pillar series.

Figure 33: Picture of pillar series 200 taken with (a) optic camera and (b) SEM. Notice the smallest pillars in the upper left corner of the SEM image. The same pillars is hard to locate with the 5 times magnified optic picture in the TI 750 Ubi.

To be sure to hit the exact point on a micro specimen the probe tip is used to scan the surface and register topology data points. The produced image is a combination of the tip itself and the surface topology. Picture 34(a) shows a 3D representation of a pillar made by a Berkovich tip and Figure 34(b) is of the same pillar and scan area, but with a flat ended tip. Illustrations of the Berkovich tip and the flat ended tip are found in Figure 35(a) and Figure 35(b). The large variation of what appears to be the pillar top surface is a consequence of the probe geometry. The sharp ended Berkovich tip reveals the pillar diameter of  $4.5\ \mu\text{m}$  while the picture produced by the flat end tip shows a larger diameter of  $14.5\ \mu\text{m}$ , which corresponds to the sum of the pillar diameter and the  $10\ \mu\text{m}$  diameter tip end face. Only when the specimen is located with the probe scan an indentation impression is certain to be made at the pillar center.

During the specimen loading both open loop and displacement controlled indentation were tried out. A variety of loading rates, hold time, unloading rates and



(a) Pillar topology produced by Berkovich (b) Pillar topology produced by flat end probe scan.

Figure 34: Topological data produced by the indenter probe. In Figure (a) a Berkovich tip is used and in (b) a flat ended tip with  $10\ \mu\text{m}$  end diameter is used. The sharp Berkovich tip produces a pillar top representation with correct pillar diameter while the flat end tip reflects the probe diameter in the topological representation.

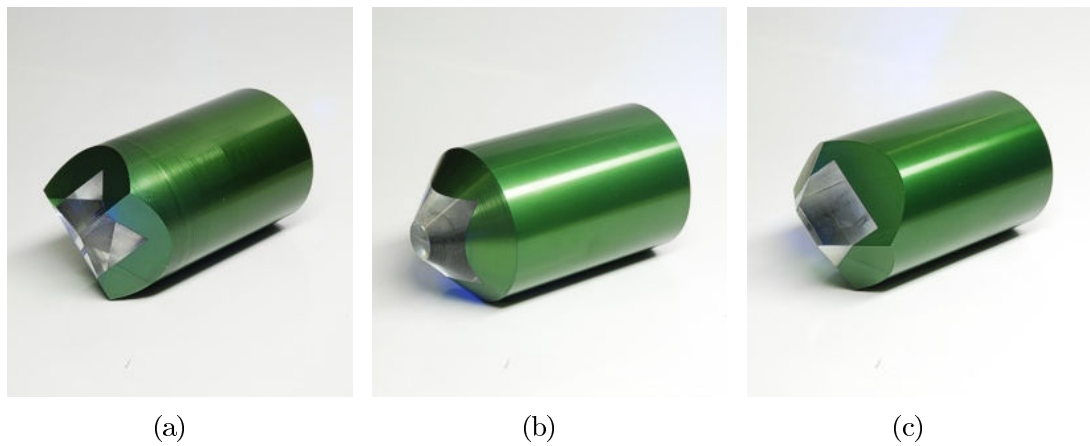
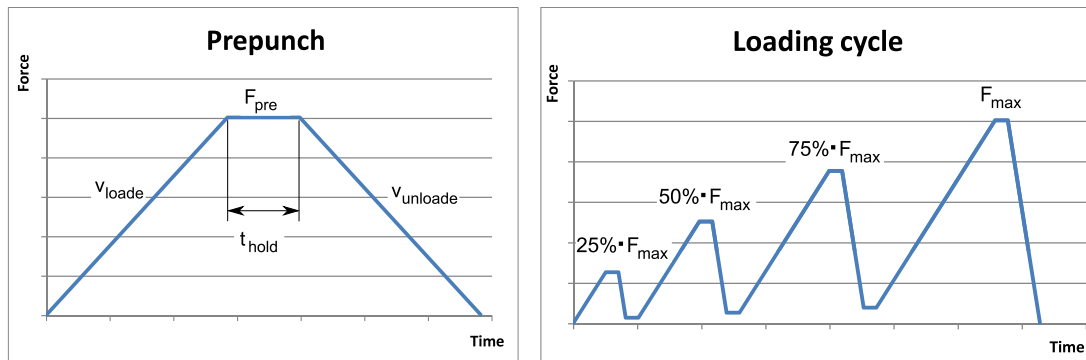


Figure 35: Illustration of three different probe tips where (a) is a Berkovich tip, (b) a flat ended tip and (c) a wedged tip. The pictures is respectively taken from [23, 24, 25].





(a) One cycle open loop punch.

(b) Four cyclic open loop punch with stepwise increasing top force.

Figure 36: Examples of open loop loading curves in the nanoindenter. Other varieties were tested, including load controlled cycles.

different cycle loading conditions was investigated. The objective was to determine the best way to load the specimen. In Figure 36(a) a one cycled open loop punch used several times to prepuce the pillar specimens. Figure 36(b) shows example of a four peaked cyclic open loop punch with stepwise increasing top force.

Similar curves were investigated for the micro fracture mechanical specimens. Since the system is load controlled, and the displacement is measured during testing, a set of parameters describing the regulatory system feedback must be defined to obtain displacement controlled testing. The parameters are the proportion gain, integral gain, derivative gain and adaptive gain.



## 4 Results and Discussion

The results and discussion section will start by going through the choice of sample and sample preparation in Section 4.1 followed by procedure of the FIB specimen preparation (Section 4.2) and procedure for the nanoindenter testing (Section 4.3). The preferred procedure is presented in different parts with a discussion of observed problems and concerns in the end of every part. The results from the testing is presented in Section 4.4, starting with the FIB prepared specimens followed by the deformed specimens and at last the data recorded during loading in the nanoindenter.

### 4.1 Sample and Sample Preparation

The chosen sample material are base metal plate and a heat treated microstructure. The heat treated microstructure consists of large, but artificial, MA phases. The large grained microstructure makes it possible to produce micro sized specimens into one phase, still it is expected to be large variety within a grain. During multipass welding the IC CG HAZ is exposed to a somewhat similar heat treatment. The microstructure in IC CG HAZ produces smaller MA phases due to the short time in two phase region. The smaller MA phases are expected to be harder than the microstructure chosen here.

Small macro samples were grinded, polished and etched while fixed to a thermoset plastic cast-in, see Figure 37. The cast-in concept gave the best results of the two tested concepts. Still the small sized beam sample is hard to prepare at two surfaces perpendicular to each other and another approach should be tried out in later work. If a custom made holder is made for the FIB, a larger sample can be prepared, which would simplify the preparation a lot. The beam sample was during probe surface scan, with the nanoindentation instrument, observed to not have  $90^\circ$  at the edges. A deviation from  $1^\circ$  to  $3^\circ$  was measured during probe imaging of the surface. The observed slope is seen in Figure 34(a) and (b). The incline should be reduced to minimize other problems and test artifacts. The small sample is hard to handle and easy to harm for instance by making unwanted surface scratches. Another possibility for the quadratic fracture mechanical specimens would be to prepare a thin film with the final thickness of the final specimen with or height. This will need a second preparation procedure.

The most critical part of the sample is the edge between two prepared faces. A sharp edge was needed to be able to produce the micro sized fracture mechanical cantilever specimens. This was the main reason why the sample surface was not electrochemical polished, but only mechanically polished. During testing the need of a reliable and good preparation is essential to obtain trustworthy results.

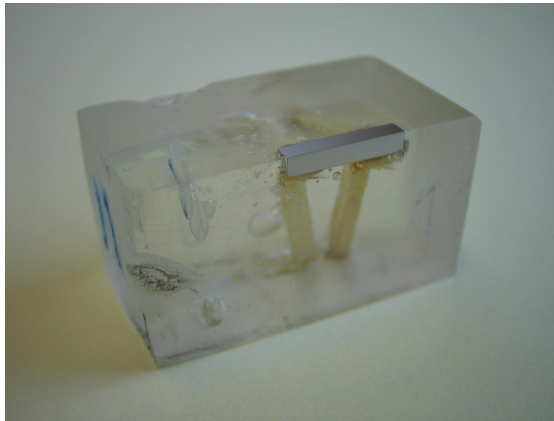


Figure 37: Picture of the sample beam molded into a thermoset plastic. The mold used to produce the samples is seen in Figure 29(b).

## 4.2 Optimized FIB Preparation Procedure

During the semester, 14 days was used to operate the FIB system. Between the visits in NTNU NanoLab the results was evaluated and improved for the next visit. In the coming section a procedure of the pillar fabrication is presented with parameter details. After the procedure, concerns and possible problems is presented and discussed. An analogous procedure and discussion is than presented for the cantilever specimens.

### 4.2.1 Pillar Specimen Preparation Procedure

The steps in pillar preparation were briefly discussed in the experimental procedure and Figure 30 should be recalled. The milling was done in two stages, the first stage with high current  $\text{Ga}^+$  to remove much material in short time. The second stage at lower current is done to obtain a small taper angle, better surface roughness and introduce less Ga implanted into the specimen. Important dimensions during milling are the extreme outer crater diameter  $D$ , pillar diameter after high current milling  $d'$ , pillar diameter after low current milling  $d$  and the pillar height  $h$ . A focused beam is important to obtain distinct edges from the milled out patterns. The smallest beam diameter at the sample surface, for the used beam current, is obtained by using the highest possible beam accelerating voltage, working at a short working distance and a clear focused picture. The used dual beam system is limited to a maximum voltage of 30 kV and the eucentric height.

The crater diameter around the pillar serves several important roles. For the fabrications point of view a large crater reduces the problems due to redeposition of sputtered material and make it possible to image the whole pillar at tilted

mode. To see the hole pillar at  $52^\circ$  tilt, the pillar outer diameter should be at least  $D \geq 2h/\tan 38^\circ + d$ . A more important requirement is stated by the nanoindenter used to punch the pillar later on. As the optic picture in Figure 33(a) showed, it might be tricky to locate very small or few pillar craters by the optic camera. The probe should be able to detect the pillar crater hole. In this experiment a flat ended indenter with end diameter of  $10\ \mu\text{m}$  was used, which limits the smallest pillar craters to  $D \geq 2d_{indenter} + d + \text{"free space"}$ . The  $d'$  should be the final pillar diameter plus machining allowance of at least  $2\ \mu\text{m}$ . Here machining allowance of  $3\ \mu\text{m}$  was used here. Using a circle pattern both the inner and outer diameter can be defined in the same pattern. In Table 4 a set of pillar diameters with corresponding recommended  $D$ ,  $d'$  and  $h$  values are given. The milling time ( $t$ ) is summarized at the bottom row, corresponding to the ion beam current of  $9.3\ \text{nA}$  which was used in the first stage. The material removal rate in these conditions are almost the same as for Si of about  $75\ \mu\text{m}^3/\text{min}$ . A correction of the height and milling rate might be done. This correction is neglected here but is presented in "Pillar Preparation Concerns". The largest pillars take close to three hours to mill out. Figure 30 indicates use of a step profile. By introducing two steps the production time might be reduced to half of the time. This is done by placing overlapping circle patterns with different outer diameter on top of each other. If the milling is done in serial the pattern with smallest outer diameter should start first. Especially for the largest pillars the step profile is reducing the milling time. The material removal rate is higher at edges, so introduction of edges in a step profile gives extra material removal where the patterns boundaries overlap. Figure 38 shows an example of a pillar after high current milling with overlapping patterns. The last pattern in this case has a larger inner diameter leaving unwanted redeposition on the pillar.

Table 4: Overview of important parameters during high current milling at  $9.3\ \text{nA}$ . Final diameter after low current milling  $d$ , inner diameter after high current milling  $d'$ , outer crater diameter after high current milling  $D$ , pillar height  $h$  and high current milling time  $t$  is given in the table. The material removal rate corresponds to about  $75\ \mu\text{m}^3/\text{min}$ .

$d\ [\mu\text{m}]$	1	2	3	4	5
$d'\ [\mu\text{m}]$	4	5	6	7	8
$D\ [\mu\text{m}]$	26	28	30	32	37
$h\ [\mu\text{m}]$	2.5	5	7.5	10	12.5
$t\ [\text{min}]$	17	40	68	102	171

When the main material removal has been done, during the high current removal, a lower current milling is used to produce the final shape. This second

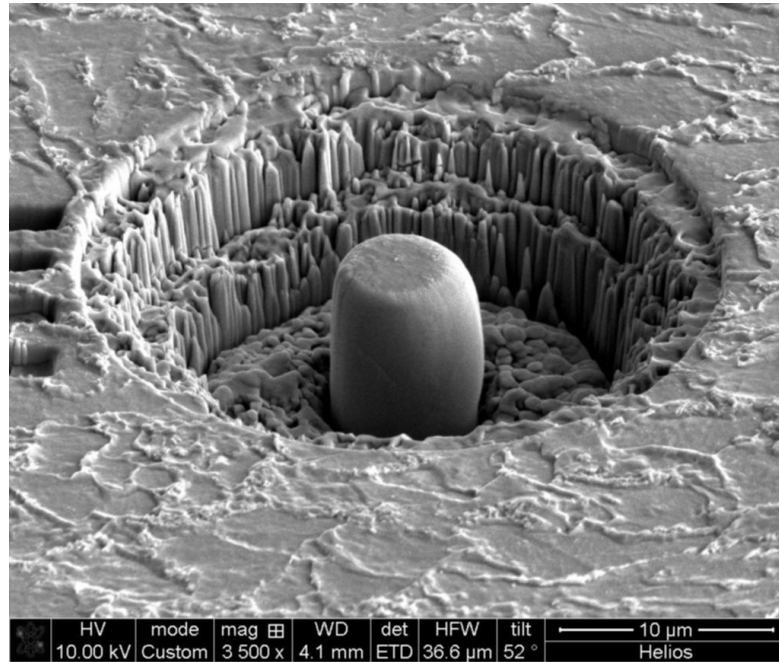


Figure 38: Picture of Pillar204 after high current milling. A step profile was used to reduce the fabrication time and the pillar is still visible at 52° tilt.

stage is more manually than the high current milling stage, and involves several manual pattern fitting. The main steps and parameters are summarized in Table 5 for pillars with 1, 3 and 5  $\mu\text{m}$  in diameter. The procedure is the same for all the different pillar sizes except for the data given in Table 5. The route to a finished pillar is explained for the 1  $\mu\text{m}$  diameter pillar. The same route is achieved for a larger diameter sample by adjusting the parameters according to Table 5.

Figure 39 shows a set of images taken by the FIB during milling of Pillar201. Corresponding SEM images, at 52° tilt, is given in Figure 40. The first pattern used is a circle pattern and beam current ( $I$ ) of 0.28 nA. The outer pattern diameter ( $D_p$ ) is adjust to the inner diameter from the high current milling at 4  $\mu\text{m}$  and the inner diameter ( $d_p$ ) is set to 1.5  $\mu\text{m}$  which is one halve micrometer larger than the finished pillar diameter ( $d$ ). The start condition is pictured in Figure 39(a) and Figure 40(a). The pattern is started with small  $z_p$  values, 0.1  $\mu\text{m}$  might be enough. At the tapered pillar side the material removal rate is much higher than at the pillar top surface. This is due to the large angel between the local surface and the  $\text{Ga}^+$  ion beam direction. It is desired to obtain an as defined dept as possible. To do this the local high spots must be ignored for a short while, and the local lowest spots should be in focus. The pattern must be started several times and when the local lowest parts are reaching the dept milled out during

Table 5: Showing important parameters during low current milling. The parameters is the pillar diameter after high current milling  $d'$ , final pillar diameter  $d$ , circle pattern outer diameter  $D_p$ , pattern inner diameter  $d_p$ , pattern milling dept  $z_p$  and Ga<sup>+</sup> ion beam current  $I$ .

$d'$ [ $\mu\text{m}$ ]	$d$ [ $\mu\text{m}$ ]	$D_p$ [ $\mu\text{m}$ ]	$d_p$ [ $\mu\text{m}$ ]	$z_p$ [ $\mu\text{m}$ ]	$I$
4	1	4	1.5	0.1	0.28 nA/93 pA
		Stepwise reduction of $D_p$ to 2. At least 5 steps are expected. Use polygon pattern to remove high standing parts.			
		1.5	1	0.1	93 pA
6	3	6	3.5	0.5	0.92 pA/0.28 nA
		Stepwise reduction of $D_p$ to 4. At least 5 steps are expected. Use polygon pattern to remove high standing parts.			
		3.5	3	0.5	0.28 nA/93pA
8	5	8	5.5	0.7	2.8 nA/0.92 nA
		Stepwise reduction of $D_p$ to 6. At least 5 steps are expected. Use polygon pattern to remove high standing parts.			
		5.5	5	0.7	0.92 nA/0.28 nA

the high current milling it is time to reduce  $D_p$ . The reduced  $D_p$  is adjusted to a proper diameter by looking at FIB and SEM snapshot images. The milling and  $D_p$  reduction is repeated until the pillar starts to take the correct shape. Figure 39(b) and Figure 40(b) shows how it might look like after several steps and reductions of  $D_p$  to 2  $\mu\text{m}$ .

The large variation in grain orientation, phases and elements produces a rough surface with local high points. To flatten the surface a polygon pattern is used. The polygon pattern is fast to adjust around the local high spots to flatten out the surface. Figure 39(c) shows a example of a polygon pattern and Figure 40(c) shows SEM image of the pillar after flatting the high spots.

The pillar has now started to obtain the correct shape and it is time to reduce the ion beam current to 93 pA. The last finishing is done by adjusting the inner diameter of the circle pattern to the final pillar diameter of 1  $\mu\text{m}$ . The outer pattern diameter should be about 1.5  $\mu\text{m}$ . The outer diameter might be adjusted to slightly smaller values to obtain a pillar as straight as possible. Document the finished pillar by taking a picture with height and diameter measurements.

### Pillar Preparation Concerns

The pillar preparation procedure presented above is trying to obtain a pillar with a close as possible cylindrical form. A certain pillar tapering and rounded top are minimized, but unavoidable with this procedure. A defined pillar height is aimed

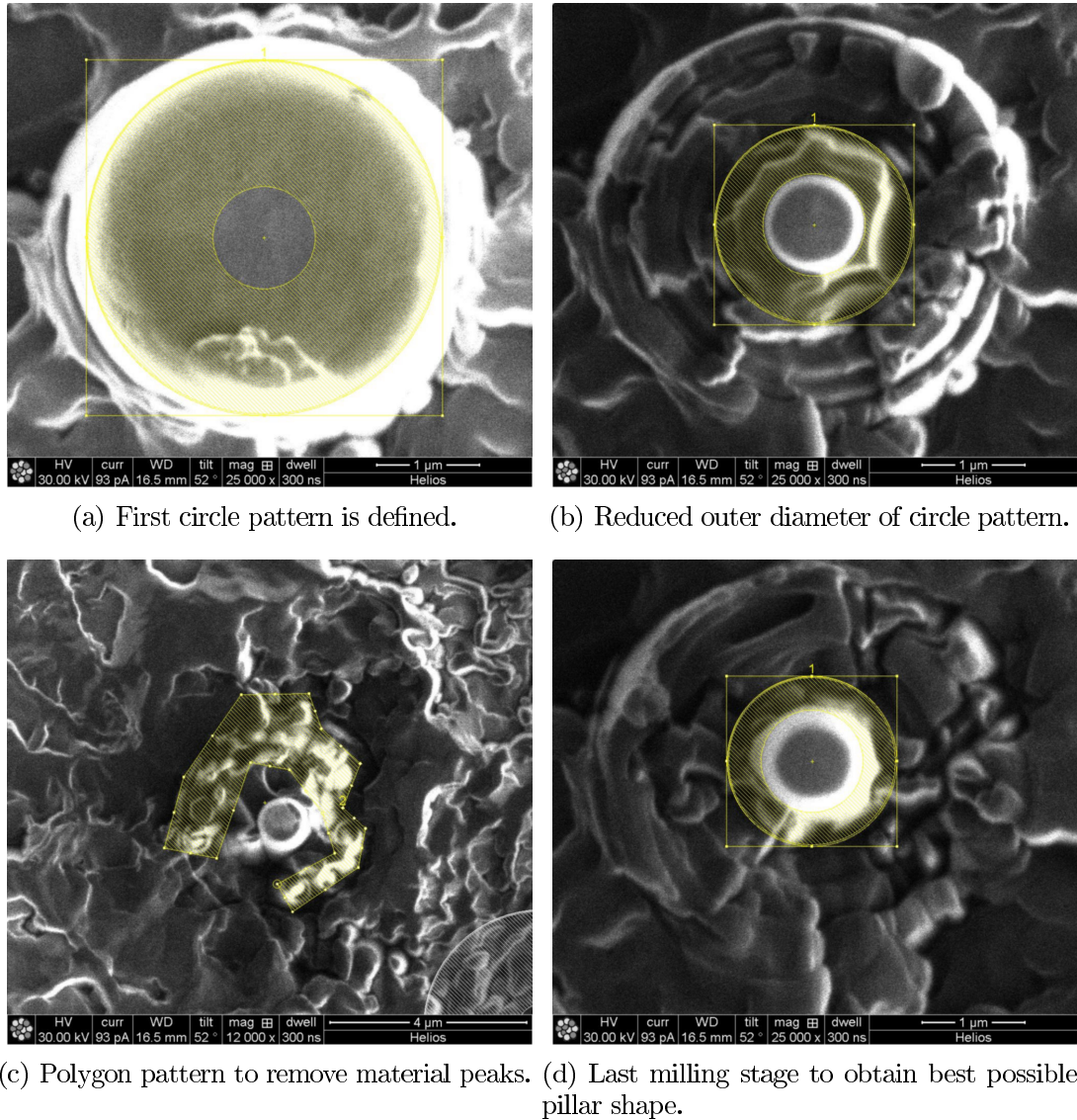


Figure 39: FIB pictures of different stages during low current milling of Pillar201. Picture (c) is from Pillar202 and picture (d) should have slightly smaller pattern diameters.



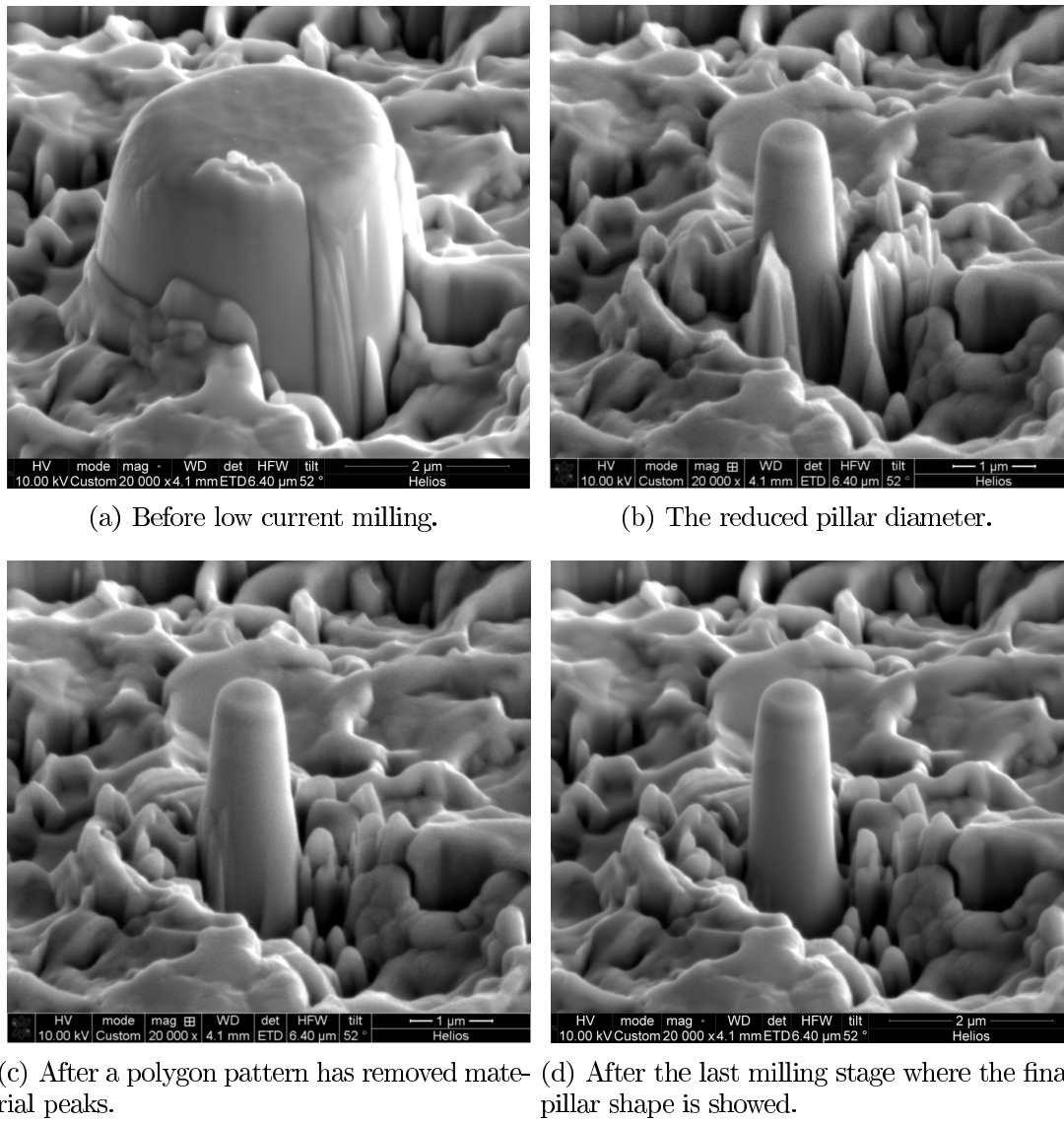


Figure 40: SEM pictures of different stages during low current milling of Pillar201.

for. In Figure 41 the high and straight Pillar105 is showed. The last milling step was done with to high  $z_p$  value and a crater close to the pillar was made. The crater makes it hard to determine the actual pillar height, which is causing wrong strain values to be calculated from the nanoindenter measurements. In this situation a large height to diameter ratio resulted in pillar buckling during compression, something that is unwanted.

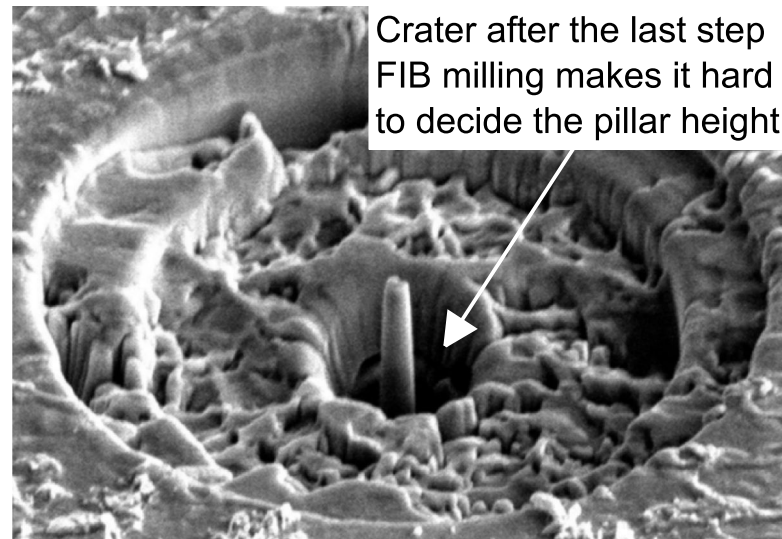


Figure 41: Picture of Pillar105. Before the procedure above was made and used. Lack of milled dept control during the low current milling makes it hard to define the pillar height. During loading buckling will be a problem because of the large height to diameter ratio.

The pillar height is measured by the measuring tool in the FIB/SEM instrument. The measurement is predefined to take care of the tilt angel and measure distances at the surface. The pillar height will not be correct when measuring directly. The measuring tool might be manually defined. If the tilt is defined to  $0^\circ$  tilt the projected height ( $h'$ ) as illustrated in Figure 42(a) will be measured. By using the geometrical equation given in the figure the correct height is obtained. Manually defining the tilt angel to  $38^\circ$  will give a correct value from the FIB/SEM system. Figure 42(b) supplements with a simplified taper angle consideration.

During FIB milling in a sample having varying properties the so-called "theater curtain" effect might appear. Figure 43 shows Pillar206 exhibiting this artifact. The curtain effect appears from soft and hard spots in the sample that results in grooves and ridges in the surface. As described in Section 2.3.1 the ion-solid interaction, and hence the milling properties, are affected by grain orientation differences, topology and the nucleus mass. The surface cut is most sensitive to the

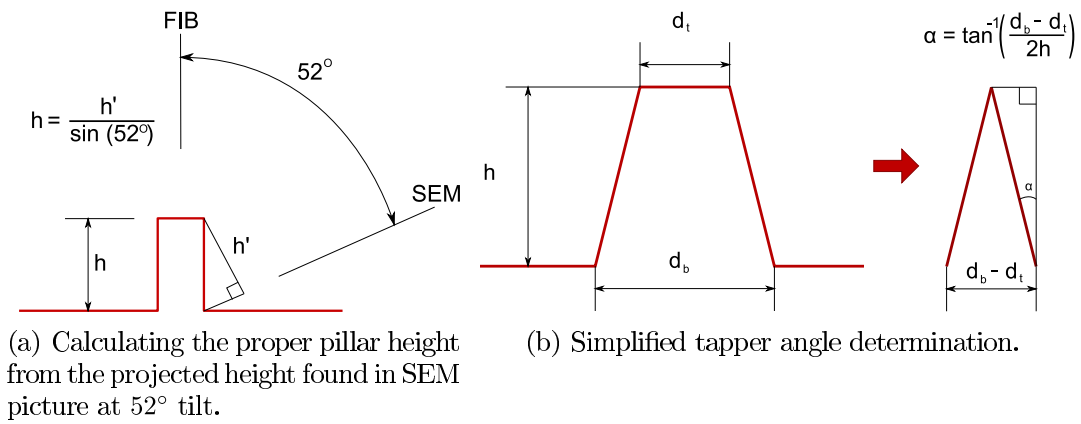


Figure 42: Determination of (a) pillar height and (b) pillar taper angle.

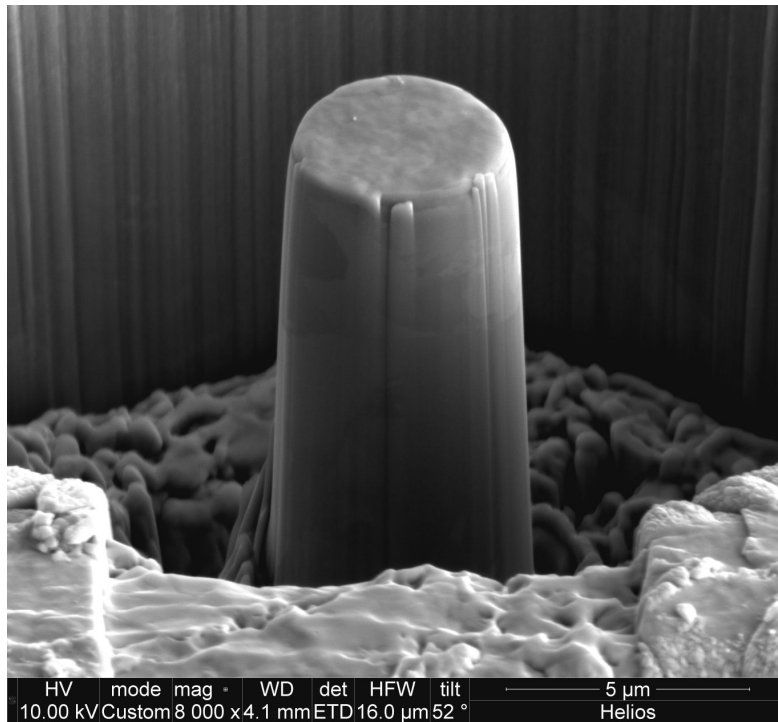


Figure 43: Striations in the Pillar206 side surface are probably caused by harder microstructure at the grain boundary.

striations and several advices can be found to reduce the "curtain", or "waterfall", effect. Changing the milling parameters, employing a higher ion beam dose, small adjustments of the ion beam angle or deposition of a uniform hard protective surface FIB-deposited layer are a selection of the found advises [12, p. 128, p. 178, pp. 161–162]. For all the base metal pillars with diameter larger than  $3.5\ \mu\text{m}$  striations are observed along the surface. Smaller pillars seems to obtain a smother surface without this kind of artifact. The pillars were systematic placed in center of large surface grains the pillars with the largest diameters are probably reaching harder phases at the grain boundary. This interpretation indicates that here is a relation between the observed striations, pillar diameter and grain size.

During the milling of cantilever specimens the specimens are manually tilted  $90^\circ$ , as described in Section 3.2. The dept milled out before tilting can easily be measured from the SEM or FIB image. This was done to compare the milled dept with the system defined  $z_p$  dept value for Si. From the literature it was found that Fe has a larger TRIM simulated sputtering yield than for Si and Al, and some less than for Cu and Zn, see Figure 15. Pictures of milled Si, Al, Cu and Zn trenches, using the same pattern conditions during milling, are seen in Figure 16. By comparing the sputtering yield and the depth of the milled trenches, the milled dept of Fe is expected to be about 19 % deeper than for Si. It must be emphasized that this is an interpolated value and the TRIM simulation it selves does not account for variations in grain orientation or topological effects. In the examined steel different phases and elements are expected to be present. For the base metal the milled dept was observed to be around 7 % deeper than for Si. In the heat treated sample, within the MA grains, the measured dept was about 29 % deeper than for Si.

#### 4.2.2 Cantilever Specimen Preparation Procedure

Figure 31 introduced the steps in the cantilever specimen fabrication. The same procedure is presented here with more detailed information. The most fabricated cantilever geometry had dimensions close to  $3 \times 3 \times 12\ \mu\text{m}^3$  and the notch located  $3\ \mu\text{m}$  from the fastened cantilever end. Same geometry is used to describe the cantilevers fabrication steps beneath. A summarized description is given in Table 6. The same procedure is possible to apply for other geometries by adjusting the parameters, where  $I$  is the most important parameter to adjust.

When a good location for the cantilever is found at the edge, a polygon pattern should be stretched around the coming cantilever. A disabled rectangular pattern, that is given the final cantilever dimensions, might be handy to use as construction lines for the polygon pattern and other patterns to be used later. Figure 44(a) shows a example of a polygon pattern and a rectangular pattern used as construction lines. There should be a machining allowance of about one micrometer to

allow later material removal at lower ion beam current. The polygon  $z_p$  is set to  $6\ \mu\text{m}$  and  $I$  is set to  $6.3\ \mu\text{m}$ . SEM picture of the resulting crater is seen in Figure 44(b) and corresponds to upper left illustration in Figure 31.

The sample is brought out of the vacuum chamber and manually tilted  $90^\circ$ . When the micrometer specimen is located a cleaning cross section (CCS) pattern is used to remove much material fast. The pattern should start from the open end at the left side and move to the right side in Figure 44(c). Figure 44(d) is a SEM image after the cleaning cross section pattern with  $z_p$  of  $1.5\ \mu\text{m}$  and  $I$  of  $6.3\ \text{nA}$ . The picture illustrates the redeposition problems related to the high milling rate. To clean away some of the redeposited material and clean around the cantilever a polygon pattern is again stretched around the cantilever, see FIB image in Figure 44(e). An appropriate  $z_p$  is now  $2\ \mu\text{m}$  at still  $6.3\ \text{nA}$  current. Figure 44(f) shows the result that appears after about two minutes. At this stage the cantilever is starting to obtain its final shape corresponding to the upper right illustration in Figure 31.

$I$  is reduced to  $2.8\ \text{nA}$  and a set of three CCS patterns are defined around the cantilever. Figure 45(a) shows a picture of this, but only one pattern is yellow and active. The pattern should move towards the cantilever and mill almost to final shape. In this stage the CCS pattern should be started with small depths and multiple times. Before every restart the distant pattern border should be adjusted as close as possible to the cantilever boundary. When the cantilever side surfaces is smooth as in Figure 45(b) the steps done at  $2.8\ \text{nA}$  can be repeated with  $I$  of  $0.28\ \text{nA}$ . This last reduction is shaping the cantilever to its final shape in three of its edges which corresponds to the lower right illustration in Figure 31. The cantilever width and length should be measured before the sample is taken out of the vacuum chamber and manually tilted  $90^\circ$  back to its first position.

When the cantilever is located again after the tilting the steps in the previous paragraph is repeated. The cantilever is now ready to become a micro fracture mechanical specimen by introducing a notch. The notch should be located  $3\ \mu\text{m}$  from the fastened cantilever end and has a notch depth smaller than half of the cantilever depth. Ion beam current of  $0.28\ \text{nA}$  can be used to mill out the main notch, but the last part should be milled out with a current of  $93\ \text{pA}$  or even as low as  $28\ \text{pA}$  to get a sharp crack like notch as possible. The finished micro fracture mechanical specimen should be documented with appropriate measurements.

Table 6: Table of important parameters during FIB preparation of  $3 \times 3 \times 12 \mu\text{m}^3$  fracture mechanical specimens. Example of pattern milling time  $t$  is indicated, but more the time must be accounted to set up and adjust patterns.

FIB $\perp$ to	Pattern	$I$	$z_p$ [ $\mu\text{m}$ ]	$t$ [ $\text{min}$ ]	Description
Side face	polygon	9.3 nA	6	30	Remove material around the cantilever. Pattern should be similar to pattern in Figure 44(a).
Top face	CCS	9.3 nA	1.5	2	Remove material around the cantilever. Pattern should start from right side and mill to the right, see Figure 44(c).
Top face	polygon	9.3 nA	2	6	Make a nicer crater around the cantilever. Mainly done for cosmetic reasons, see Figure 44(e).
Top face	CCS	2.8 nA	$3 \times 0.5$	2	Form the cantilever close to its final shape. The outer CCS boundary should be put stepwise closer to the cantilever, see Figure 45(a).
Top face	CCS	0.28 nA	$3 \times 1$	10	Stepwise reduction as in the step above until the cantilever reaches its final shape.
Side face	CCS	2.8 nA	$3 \times 0.5$	2	Form the cantilever close to its final shape. The outer CCS line should be put stepwise closer to the cantilever.
Side face	CCS	0.28 nA	$3 \times 1$	10	Stepwise reduction until the cantilever reaches its final shape.
Side face	CCS	0.28 nA	$3 \times 1$	10	Mill out the notch. A thin CCS pattern is used close to the notch final dept.
Side face	CCS	28–93 pA	3	1	The last cut to make the notch as sharp as possible. A thin CCS pattern of 50nm is possible for the 28pA current.

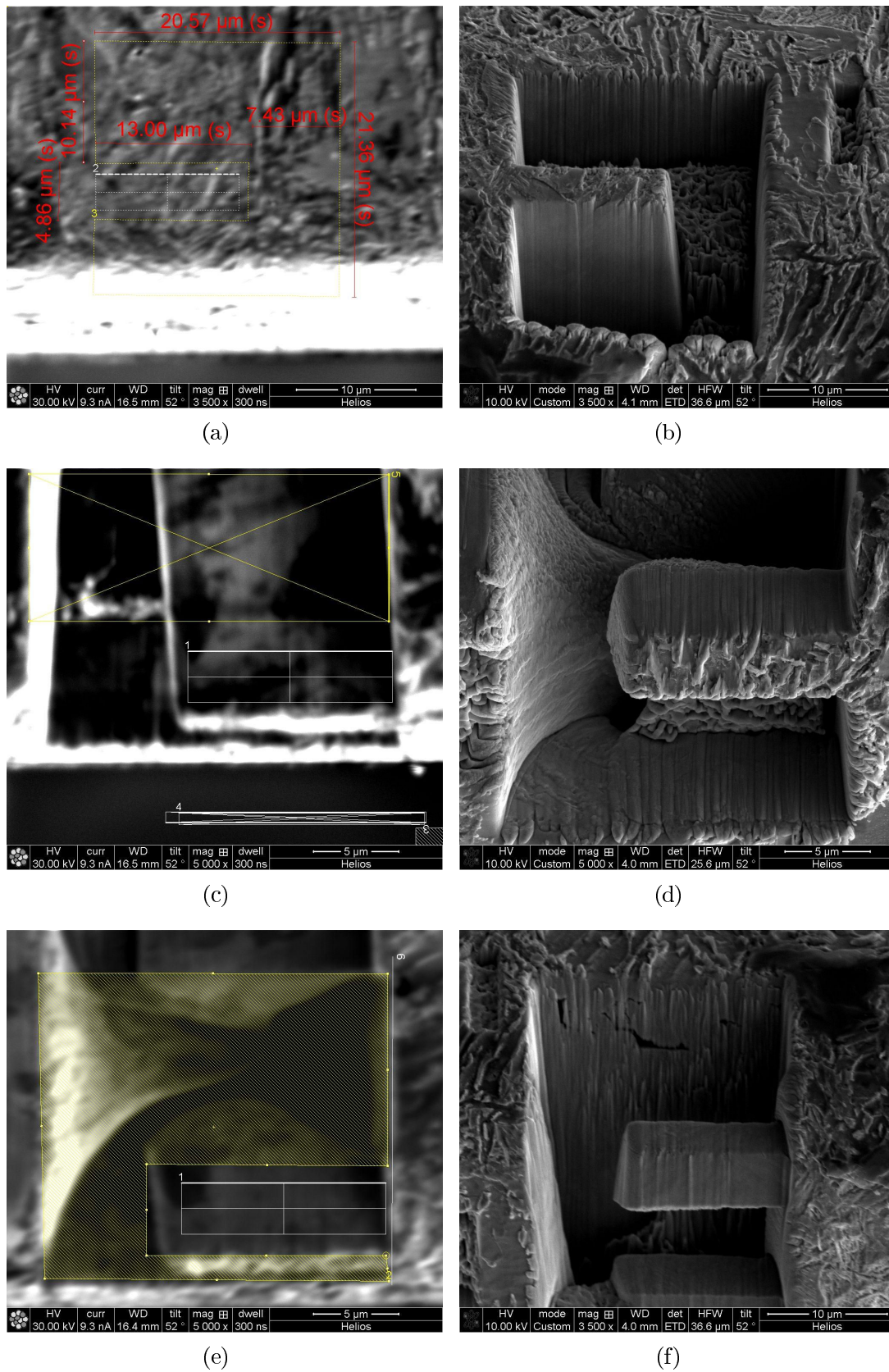


Figure 44: Pictures of the first steps during  $3 \times 3 \times 12 \mu\text{m}^3$  fracture mechanical specimen preparation.



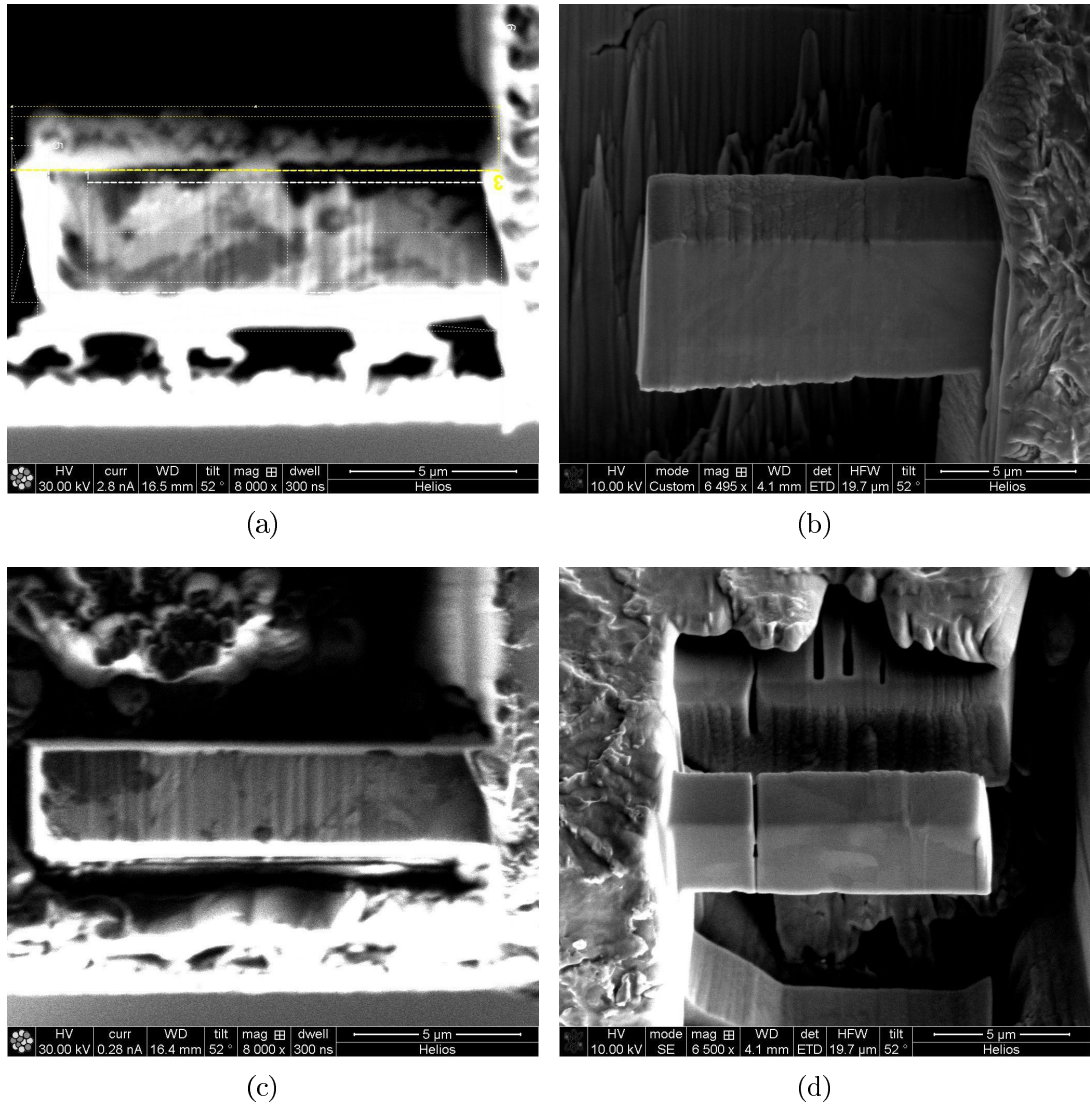


Figure 45: Pictures of the last steps during  $3 \times 3 \times 12 \mu\text{m}^3$  fracture mechanical specimen preparation.



### **Cantilever Preparation Concerns**

The prepared fracture mechanical cantilever specimen is located at the sample edge. The edge of the sample is hard to prepare during sample preparation and has a rounding off that might include residual stresses. An edge radius forces the cantilever to be located a small distance from the edge that might complicate the nanoindentation loading later on. The cantilever should be as close as possible to the surface. A distance as small as one half micrometer makes it hard to find the cantilever during probe scanning in forehand of the nanoindentation loading. If the free space around the cantilever is not sufficient the nanoindenter might stroke the surrounding material and affect the experiment.

The small specimens and the manual sample tilting are not a good way to do the specimen preparation. Several times during sample handling micro-sized cantilever specimens were destroyed.

### **4.3 Optimized Nanoindentation Testing Procedure**

Two series of pillars (pillar series 100 and series 200) and one series of FM specimens (FM series 100) were tested. This corresponds to 13 pillars and 5 cantilevers. The testing was partly done in INM Saarbrücken (pillars series 100 and FM series 100) and partly at NTNU in Trondheim (pillar series 200). Pillar series 100 and FM series 100 were tested with a flat ended tip of 5  $\mu\text{m}$ . It was early concluded that the cantilever specimen should be tested with use of another tip geometry. Examples of tips that might be suitable for the cantilever loading are a sharp tip as the Berkovich tip in Figure 35(a) or some kind of wedged tip as Figure 35(c) shows an example of. The earlier prepared dummy sample with FM series 000 was tested with use of a Berkovich tip. The results were mixed with positive and negative observations. The slightly tilted surface and a jump, from the sample surface and down to the cantilever specimen, were in some situations exceed the transducer working depth for the nanoindenter instrument. The variations in local height makes it hard to provide with a good surface scan and during sample loading the tip might touch the surrounding sample, something that makes it hard to interpret the logged data. A wedged tip could load the specimen along a line at the cantilever end. If the wedge is located perpendicular to the beam length this will give a defined and stable loading. Below is a procedure that describes the pillar and the cantilever loading presented. The pillar procedure has been tested several times, but the cantilever specimen loading is at this time a made up procedure. It is therefore expected that changes must be done to the cantilever procedure in the future.

### 4.3.1 Pillar Specimen Testing Procedure

The nanoindentation system should be provided with a flat ended tip with at least the diameter of the pillar specimens to be tested. Standard calibration to align the optic to the tip center and air calibration should be done. With a large probe tip it can be hard to produce an indentation visible by the optic camera, which is necessary during the calibration. In this experiment a soft indium sample was used during calibration, see Figure 32.

The pillars are first located by the optic camera as in Figure 33(a). When the sample boundary is defined and the optic picture center is aligned to the chosen pillar center, the probe scan can start. Scan rate between 0.25 and 0.5 Hz and a setpoint load of 1  $\mu\text{N}$  are suitable start conditions. If the pillar is small it might be damaged by a high setpoint load. The first scan is revealing the pillar position like in Figure 46(a). By adjusting the scanned area the pillar is moved to the scan center as in Figure 46(b). If several circles exist on the pillar top the largest should be aimed for. Smaller circles might be small local heights at the pillar top that provides an image of the indenter end surface.

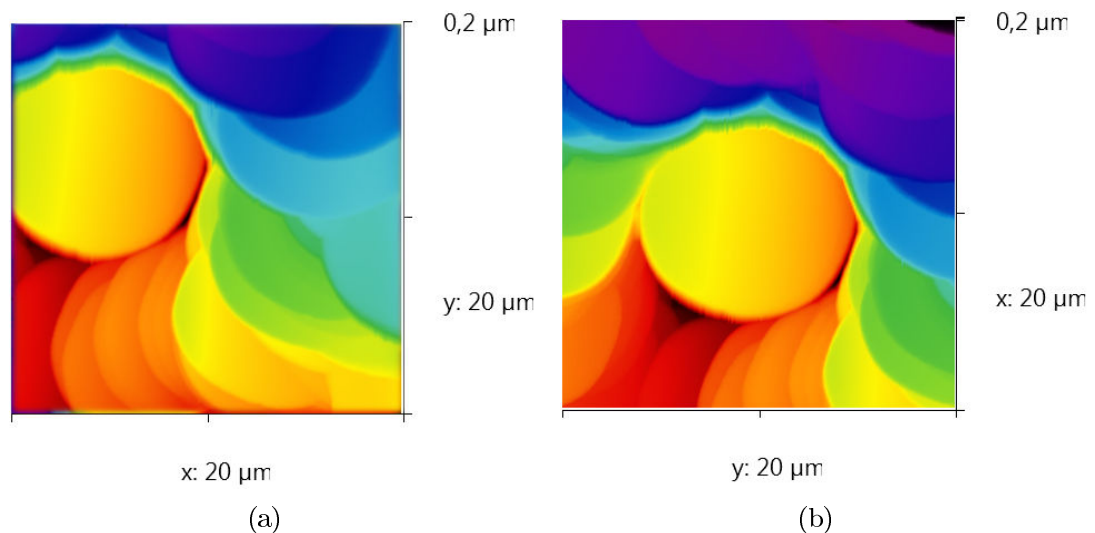


Figure 46: Colored picture from a probe scan. In (a) the pillar is out of the center and in (b) the pillar is adjusted to the center of the scan.

A load function must be defined before the loading can start. For the pillar specimen the open loop loading is a good choice. Figure 36(a) and (b) gives two examples of cyclic open loop load functions. The one cyclic open loop punch was used to prepunch the pillar. The imperfect pillar top is during the punch smoothed out and a more cylindrical pillar top is created. The prepunch maximum force was typical set to half of the expected pillar yield force. After one or

several prepunch a four cycled open loop punch up to the expected yield force was started. If yield did not occur the same four cycled open loop was restarted with a higher maximum force. Typical parameters during the load cycle are given in Table 7. The unloading rate ( $v_{unloade}$ ) used was typical two times larger than the loading rate ( $v_{loade}$ ). The expected yield force was estimated from the bulk sample properties and later from tested pillars. Expected yield force values in the table were estimated from the first pillar compression tests.

Table 7: Parameters during base metal pillar loading.

d[ $\mu\text{m}$ ]	$v_{loade}$ [ $\mu\text{N/s}$ ]	Expected $F_{yield}$ [ $\mu\text{N}$ ]	$0.5F_{yield}$ [ $\mu\text{N}$ ]
1	2.5 – 4	275	140
3	20 – 30	2475	1240
5	60 – 70	6870	3435

### Pillar Testing Concerns

During pillar compression testing there were problems related to the slightly tilted sample surface. If a large surface area is scanned, in the  $40 \times 40 \mu\text{m}^2$  range, and a pillar is present the transducer work distance is easily exceeded. The lack of misalignment, larger than  $1^\circ$ , between the flat ended tip and the pillar top surface has been reported to lead to a number of artifacts as underestimation of the yield point and elastic modulus, change to the strain-hardening response and buckling [35, p. 365]. This reveals the importance of a flat and aligned surface in future experiments.

Another concern is the high surface roughness produced during mechanical polishing and etching of the sample. To minimize the surface roughness the surface should be electrochemical polished and only etched if necessary. The etching looks necessary to identify the microstructure during optical and SEM investigation. In the future an EBSD scan might be used to identify the grains of an unetched surface. The large surface roughness is a possible concern that might produce test artifacts similar to the sample misalignment.

It is known that there exists a certain deformation in the sample beneath the pillar. The displacement data is sometimes corrected according to the formula given in Equation (7), taken from reference [36, p. 5570]. The elastic modulus can be obtained by standard nanoindentations within the same grain as the pillar is produced within and act as a reference value to compare with the slope of the later pillar compressions data.

$$\Delta x = \Delta x_{means} - \frac{F(1 - \nu^2)}{dE} \quad (7)$$

A more general observation, is the highly sensitivity the nanoindenter system has to vibrations. During testing of pillar 204 there was maintenance work in the building that affected the test result. The stress and strain curve in Figure 67(b) shows signs of this in form of large and varying system drift and vibrations.

### 4.3.2 Cantilever Specimen Testing Procedure

The cantilever procedure is similar to the pillar loading procedure. The system should be calibrated with a Berkovich tip and the surface spot where the cantilever specimen is placed should be located with the optic camera. When the work space is defined the optic picture should be located at the specimen side of the cantilever geometry. This ensures that the probe scan starts at the sample surface and not in a deep FIB milled out hole, or even hit outside the sample edge. If the scanned area is about  $40 \times 40 \mu\text{m}^2$  the cantilever geometry is soon located by moving stepwise toward the edge. When the  $3 \times 3 \times 12 \mu\text{m}^3$  fracture mechanical specimen is located as in Figure 47(a) and the free end is identified the probe scanned area must be reduced and centered at a point about  $2 \mu\text{m}$  or  $3 \mu\text{m}$  from the free beam end and as close to the beam center as possible.

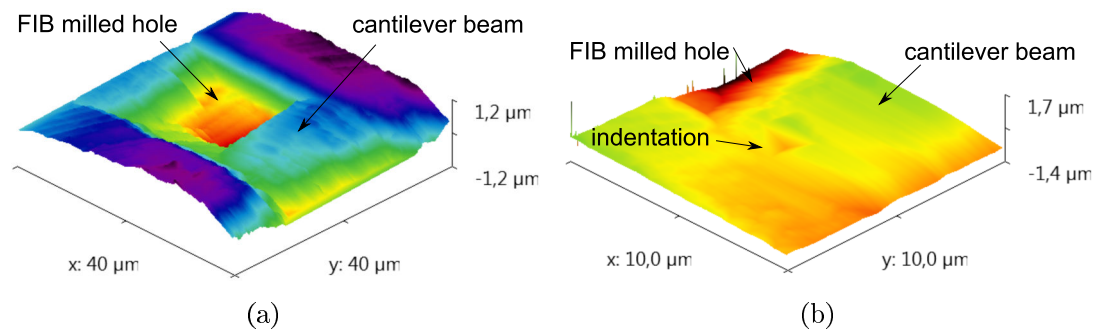


Figure 47: Colored 3D picture of the cantilever scan. Picture (a) shows the scanned cantilever with sounding FIB milled out hole and (b) shows a zoomed view at the pillar end with an indentation. This cantilever was not loaded to failure.

The load function should now be defined. A displacement controlled load function is a good alternative for the cantilever specimens. The necessary load to be applied before the cantilever start to deform plastic is much harder to define than for the pillar specimen. Small variations in the crack dept might give large variations in such estimates. Since the nanoindentation system is applying load and measuring the displacement a set of parameter describing the regulatory feedback must be defined. The used parameters are listed in Table 8 and were not tried to optimize further. Stepwise load function with steps of 50 nm or 100 nm and loading rate around 4 nm/s or 5 nm/s is a good starting point.

Table 8: Parameters describing the regulatory feedback during displacement controlled loading in the nanoindenter.

Proportion Gain	Integral Gain	Derivative Gain	Adaptive Gain
0.09	0.8	0.09	0.4

### Cantilever Testing Concerns

The cantilever specimens are generally harder to locate than the pillar specimen. The rounded off edge reflect the light from the optic camera in unwanted directions, something that makes it hard to obtain a good optic picture. The large height variations and large step down to the cantilever specimen are reaching the probe working range and complicates the scan. To locate the cantilever specimen sufficient material around the specimen must be removed. This is to allow the probe to detect the FIB milled out hole that defines the cantilever. Figure 47(a) shows a scanned cantilever with too little gap around the cantilever beam. In such cases it is hard to locate the beam edges and easy to hit neighboring material during the indentation tests.

When indenting with a flat tip, the probe loading point is hard to define accurate. On the other hand, if a sharp probe is used the measured displacement will be a combination of cantilever deflection and an indentation displaced into the surface. The indentation dept into the material can be a substantial part of the displacement and such indentation from a Berkovich tip is seen in Figure 47(b). The tip displaced dept into the sample can be corrected for by subtracting the displacement, as a function of force, for the same microstructure.

The naniondentation system, is provided with a cyclic curve creator that might be used to prefatigue the FIB notched specimen. From Takashima *et al.* [31] it is known that the notch sharpness have an effect of the measured fracture curve and stress intensity for micrometer sized specimens.

During traditional elastic plastic fracture mechanical testing one of the most important parameters are the crack tip opening displacement (CTOD) which is a physical measurement of the distance the crack is opening at the crack tip. Ideally this should be measured during testing of micro sized fracture mechanical specimens. Unfortunately, no method to do this has been found. Other proposed methods to measure the crack growth during testing are by measuring the electrical resistance over the cross section area under the crack or by measuring the unloading slope during testing [2, p. 323]. The last method is called the unloading compliance method where the load and displacement curve is partly unloaded at regular interval during the test. As the crack grows the cantilever becomes less stiff in form of a reduced slope.

## 4.4 Test Results

The test results are divided into three parts. The FIB prepared specimen is first summarized with pictures of the prepared specimens in the different series and discussed. An analogous presentation of the loaded and deformed specimens are then given. At last some of the data obtained during compression testing is plotted and discussed.

### 4.4.1 FIB Prepared Specimens

During the FIB preparation, as Table 3 indicated, there were prepared 22 pillars and 15 cantilever specimens. The specimens, as they were after FIB preparation, are summarized in Figure 48 to Figure 51. The specimens in pillars series 300 and FM series 200 were not finalized and are not pictured.

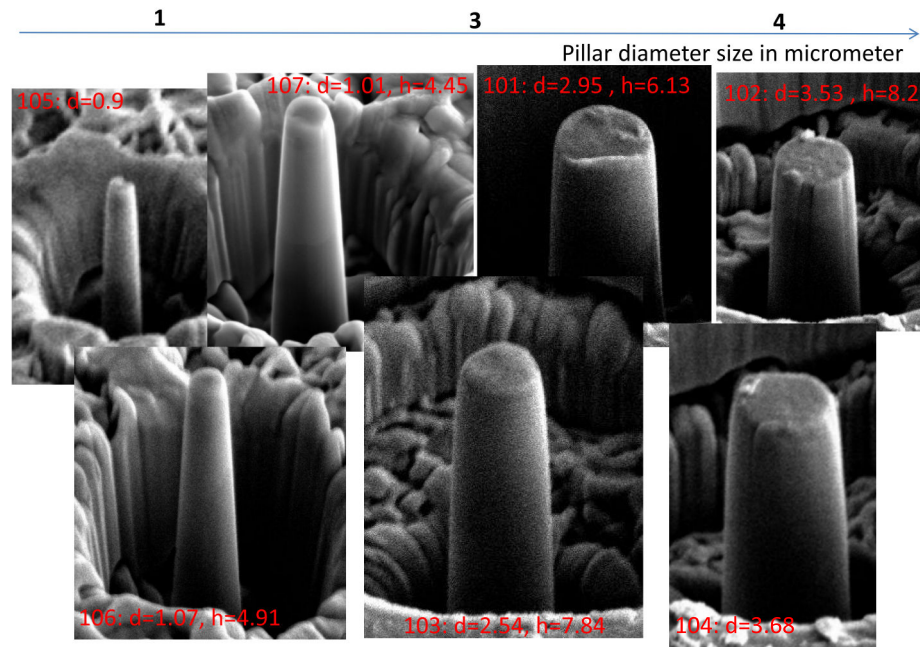


Figure 48: Pillar series 100 before testing.

Pillar series 100 was the first pillar series made in the base metal, see Figure 48. The pillar diameter is ranging from right under  $1\ \mu\text{m}$  to about  $3.5\ \mu\text{m}$  and all the samples have deep craters close to the pillar. The crater complicates the measurement of the pillar heights and the values found are not accurate. The height to diameter ratio is found to range between 2 and 5. A ratio between 2 and 3 is desired.

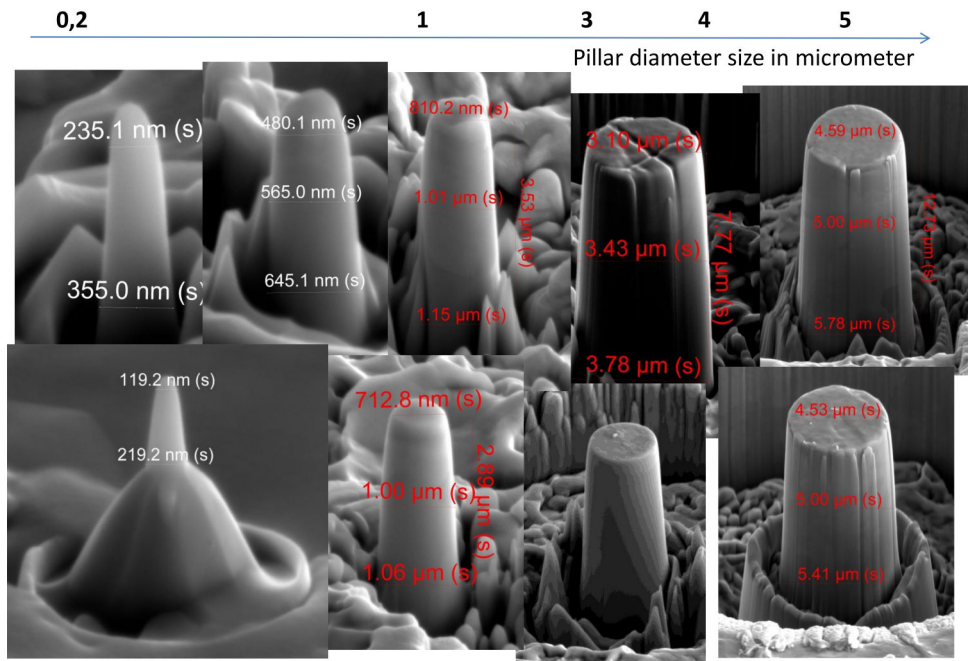


Figure 49: Pillar series 200 before testing.

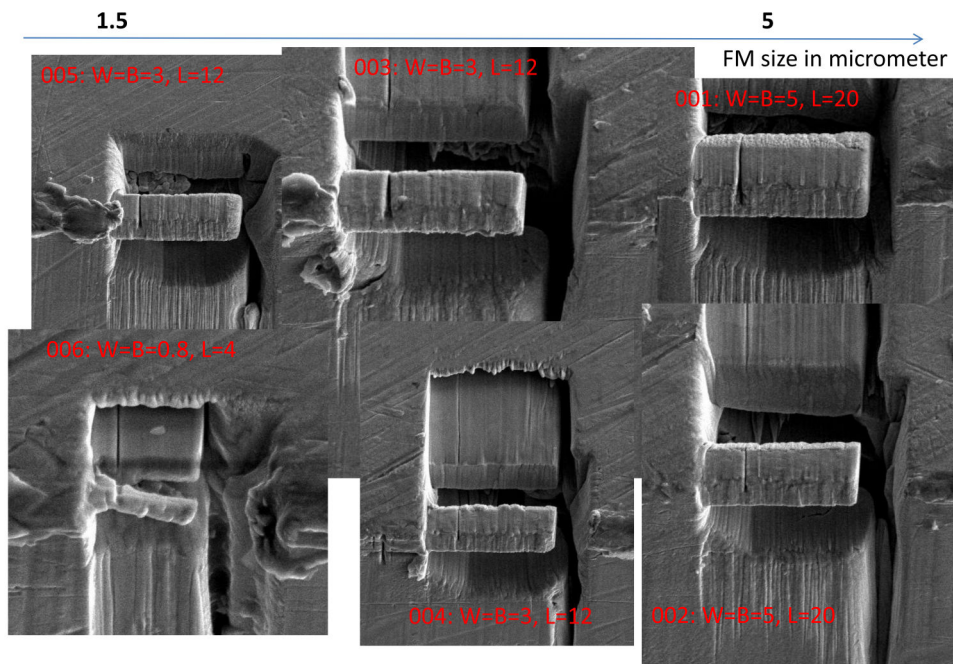


Figure 50: FM series 000 before testing.



Pillar series 200 is the second pillar series produced in the base metal. A larger dataset, a more defined height and a better height to diameter ratio were attempted. At the same time a small taper angle and an as cylindrical shape as possible was aimed for. Diameter range was extended from diameters at about 150 nm and up to 5  $\mu\text{m}$ . The smallest pillars investigate the lower limit of how small specimens that are possible to produce. The height in this series is better defined than the earlier pillar series 100. Height to diameter ratio was ranging from 2 to 5, but there was observed a better height controlled for the pillars larger than 1  $\mu\text{m}$  in diameter.

Pillar series 300 was planned made inside MA grains of the heat treated sample. The milling of 9 pillars were started, but not finished.



Figure 51: FM series 100 before testing.

Cantilever specimen series 000 was made from a dummy sample to test out the concept, see Figure 50. The FM specimens were aiming for a geometry where the ratio between  $B$ ,  $W$ , and  $L$  is  $B : W : L = 1 : 1 : 4$  and the notch depth  $a$  of  $B/2$ . The produced geometries had a  $W$  of around 1  $\mu\text{m}$ , 3  $\mu\text{m}$  and 5  $\mu\text{m}$  and the ratio described above. FIB milling parameters were investigated to produce correct geometries and a sharp notch.

In FM series 100 the same ratios as in series 000 were aimed for, but only the geometry with  $W = 3\mu\text{m}$  was tried out (see Figure 51 for the results). A better experience with the FIB milling showed results in form of more correct dimension



and less surface roughness. The milled out notches were not done in the last step and low current milling after the notch initiation gives a groove besides the notch caused by a higher milling rate at this premilled spot.

The last FM series 200 was started but not finished. Total 4 cantilever specimens with same geometry as FM series 100 were made inside MA grains of the heat treated sample, but not finalized.

#### 4.4.2 Specimens After Loading

A selection of the pillars and FM specimens presented above were loaded with a nanoindenter. The geometries after testing are presented in Figure 52 to Figure 53 beneath and discussed.

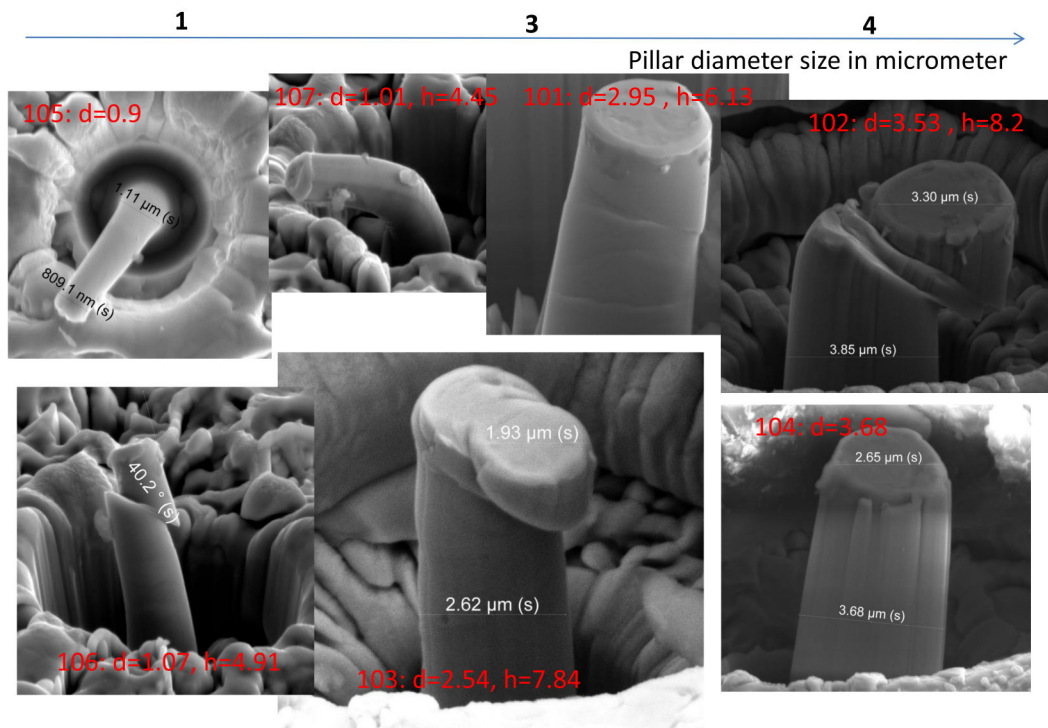


Figure 52: Pillar series 100 after testing.

Pillar series 100 in Figure 52 was loaded during the visit in Saarbrücken with a  $5 \mu\text{m}$  flat ended tip. The pillars are deforming during buckling (105, 107 and probably 104 and 106), slip planes through the pillar (101, 102, 103 and 106) and wavy deformation (103) in the pillar. The buckling happened for the pillars with smallest diameter of around  $1 \mu\text{m}$ , with one exception (104). The small pillars were pillars with ratios between 4.2 and 5.3. The larger Pillar 104 had a bigger diameter

and a smaller ratio, it is uncertain if buckling was the observed deformation type for this pillar. Deformation beneath the pillar is a possibility since the deep crater makes it hard to investigate the pillar bottom part. In general it is known that a large ratio gives unwanted buckling of pillars. Pillars deforming through slip planes across the sample diameter seems to happen through one specific slip system for Pillar102, 103 and 106. In Pillar101 it is uncertain if only one or several slip systems are active. There might be a grain boundary present allowing slip system to be activated in more than one grain at the same time. The pillars undergoing slip have diameters in the hole range and have a ratio between 2.1 and 4.2. Only Pillar103 shows signs of wavy deformation in addition to the slip deformation.

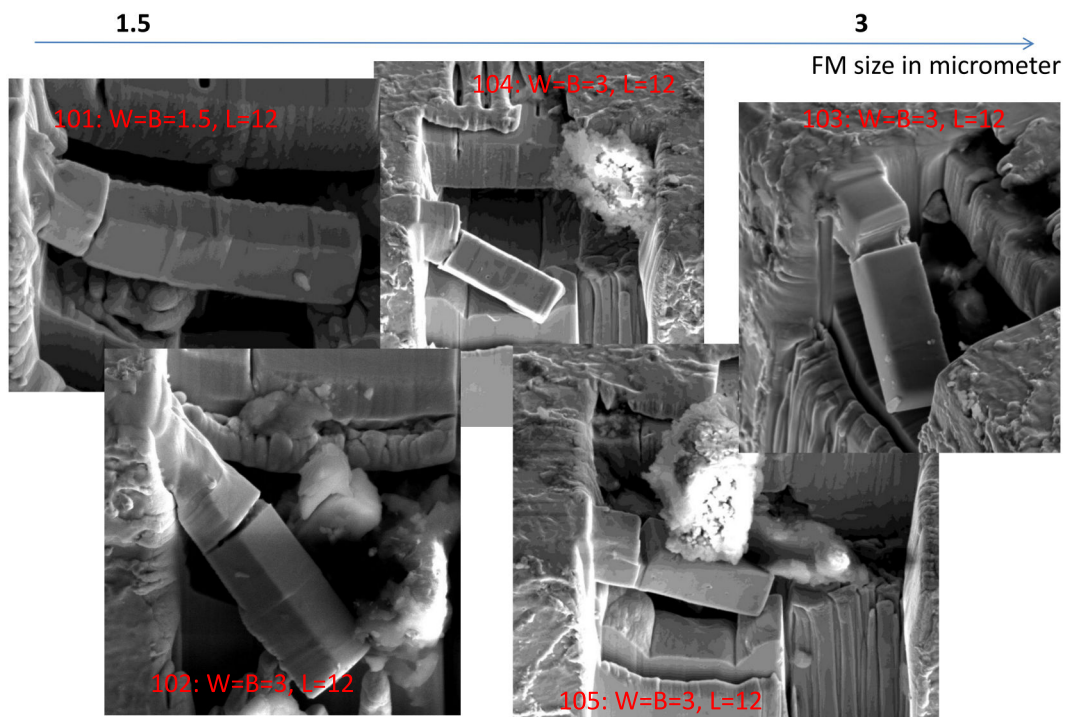


Figure 53: FM series 100 after testing.

FM series 100 after loading with a 5  $\mu\text{m}$  flat ended tip is shown in Figure 53. The large probe makes it hard to define the exact loading point. The surrounding sample might interfere with the indenter tip and produce an artifact test and artificial load data. Only FM103 deformed as expected by ductile fracture at the notched spot. A small part of the crack surface seems to have fractured brittle. It was attempted to calculate the  $K_Q$  of the cantilever. The other samples have deformed ductile at the notch or at the fastened beam end. FM102 and 104 seems to have rotated away from the sample side, this might be due to the small gap

allowing the flat ended tip, with  $60^\circ$  taper angle, to touch the sample at other spots than the wanted cantilever. A more defined loading point is obtained with a sharper loading tip. If more material is removed around the cantilever the tip will not reach the sounding material.

#### 4.4.3 Data From the Specimen Loading

The stress and strain curves for the tested pillars were plotted and are found in Appendix C and D. A table describing selected measured parameters is found in the end of the same appendixes. A simplified stress and strain curve was made to better compare the dataset of the 9 successful tested pillars. Figure 54 shows the results of the simplified plot where only increasing values are plotted. The curve should not be used for detailed analysis, but gives an outline of the performed tests.

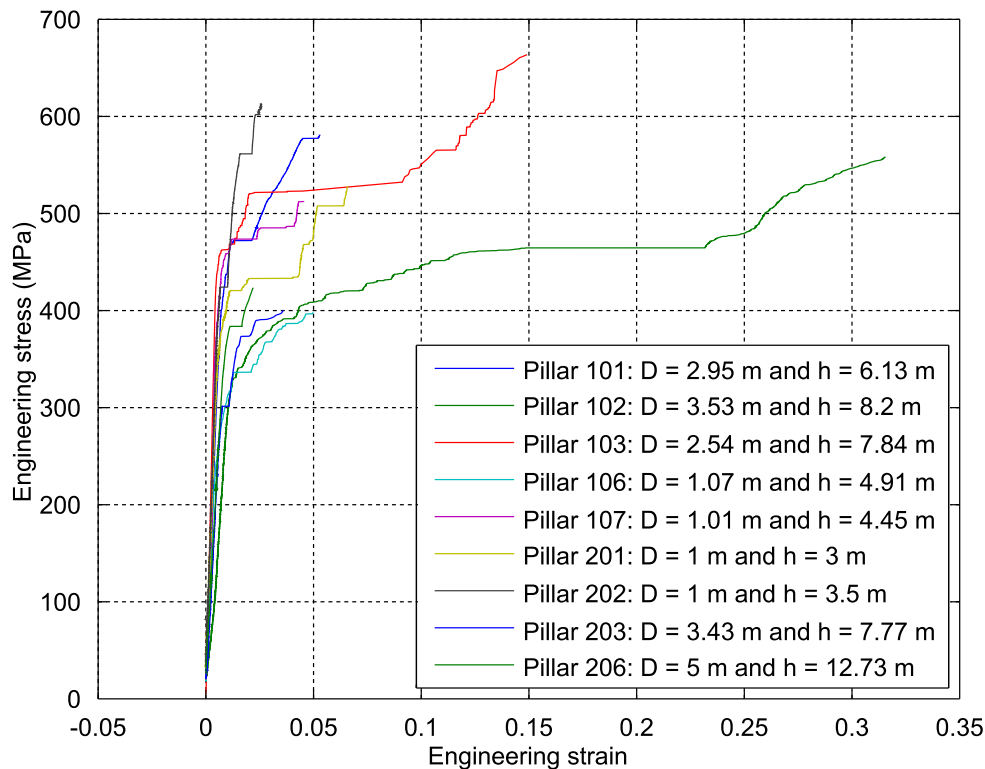


Figure 54: Showing the increasing trend on pillar series 100 and 200. The stress and strain curve shows only increasing values.

To determine if there is a trend in stress and pillar size the stress at 2% strain

was selected and plotted in Figure 55. The stress is scattering from 300 MPa and up to 560 MPa and at first sight no clear size effect is found. There exist two open symbols at Pillar204 and 205 indicating that the stress values are not at 2% strain. Pillar204 was compressed during maintenance work in the building that disturbed the measurements. Stress at 2% strain was not possible to determine, instead 2% plastic strain was used. Pillar205 has a diameter of 5  $\mu\text{m}$  and was compressed by the maximum indenter load of 10 mN without yielding. The stress value at 2% strain is therefore at a higher value than the plotted value.

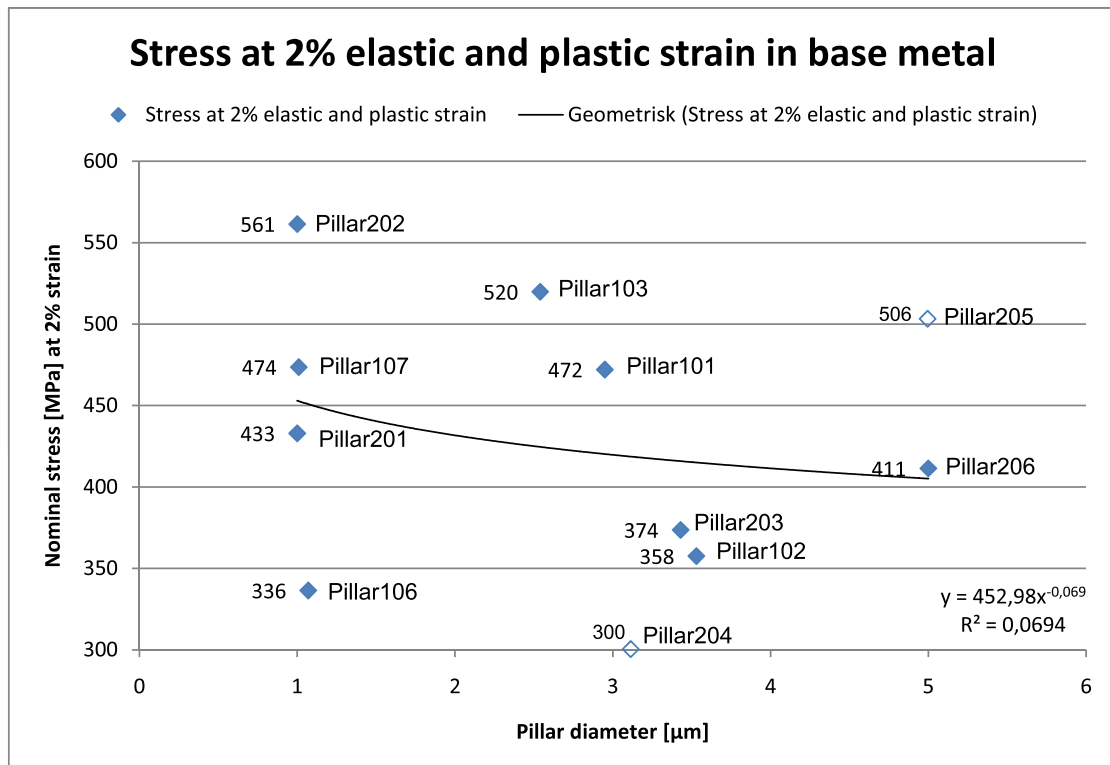


Figure 55: Stress at 2% strain for different pillar diameters from pillar series 100 and 200.

During the pillar preparation there was observed a phenomena called "theater curtain" effect for base metal pillars larger than 3.5  $\mu\text{m}$  in diameter. This might indicate that the largest grains have a size close to this value and pillars larger than 3.5  $\mu\text{m}$  might include grain boundaries and be grain boundary strengthened. Kheradmand *et al.* [17] showed that FCC nickel was strengthened by including one grain boundary vertical inside the pillar. Another fact is that the size effect is less clear for BCC metals than for FCC metals [27]. To determine the size effect for the investigated steel it should be attempted to test submicrometer pillars. To reduce

scatter in data it should be performed a EBSD mapping of the grain orientations so that pillars produced from grains with same crystallography can be compared.

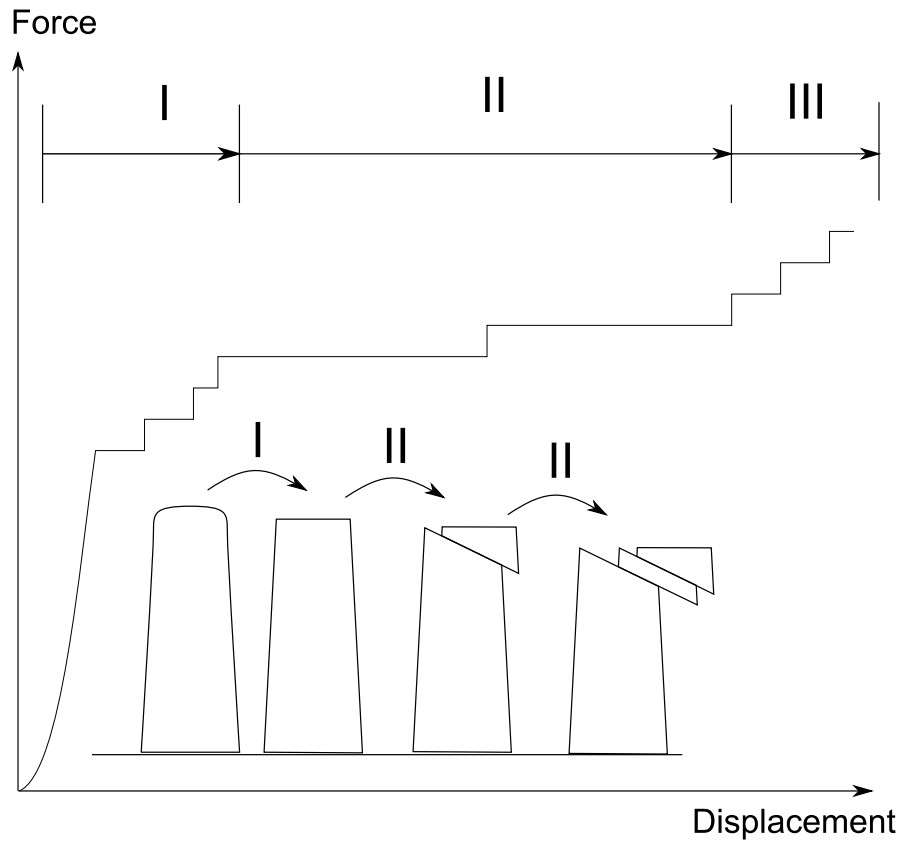


Figure 56: Pillar deformation model. After some elastic deformation small pop-in happens in stage I of the curve to form a flat pillar top. When the top is flattened larger deformation motions are mobilized and large pop-in or constant load deformation events are observed in stage II. The deformation in stage II can be wavy-deformation or slip plane deformation as shown in the figure. When the lowest energy deformation mechanism has moved as long as possible new mechanisms are started in stage III. The new deformation happens at a larger cross section or with higher required deformation energy.

The observed pillar deformation was summarized in a pillar deformation model, trying to describe more general the deformation of the pillar. Figure 56 illustrates the model and sectioning the deformation into three stages. In the beginning stage, stage I, a tapered pillar with a rounded top exists. During loading the pillar exhibits deformation in the pillar top surface in form of small local deformations.

When the top surface is flat and has a cross section close to the underlying pillar cross section, larger deformation mechanisms must be activated. Stage II starts when the larger deformation mechanisms are activated and start to move. This might be motion along slip planes or wavy deformation. When the deformation motion has moved the available distance new deformation mechanisms with higher energy or cross section are starting to mobilize.

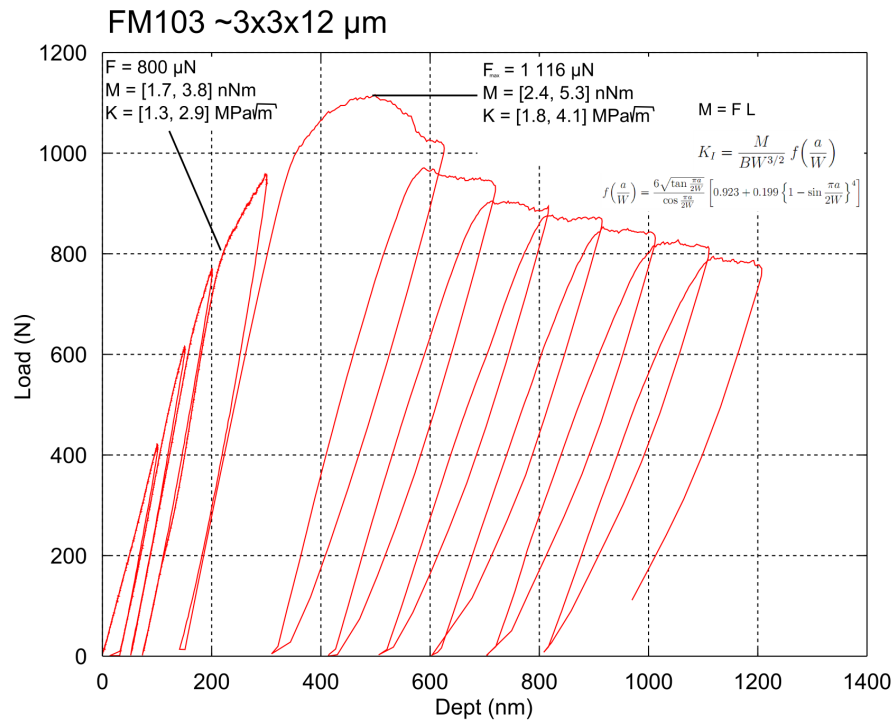


Figure 57: Load and displacement curve from FM103. The stress intensity at two points are indicated.

Only one of the cantilever bending tests gave a promising test result. This was specimen 103 in FM series 100. The load and displacement curve shows a yield point and a maximum load before the load starts to decrease, see curve in Figure 57. By applying the formula in Equation (4) and (3) the provisional fracture toughness  $K_Q$  was calculated to be between 1.3 and 2.9  $\text{MPa}\sqrt{\text{m}}$  if the observed yield load at 800  $\mu\text{N}$  is used and between 1.8 and 4.1 if the maximum load of 1116  $\mu\text{N}$  is inserted. The large variation in the values are mainly caused by the uncertain loading point.

## 5 Conclusion and Further Work

Focused ion beam (FIB) was applied on a high strength low alloy steel for Arctic conditions. Samples from the base metal and heat treated metal were prepared and used to FIB prepare micro sized specimens. The heat treated microstructure was chosen to investigate hard and brittle martensitic grains that are observed in the heat affected zone close to the weld bead. Specimens from the base metal plate were loaded in a nanoindentation system with a flat ended tip. Procedures describing the FIB preparation and nanoindentation loading were made for pillar and cantilever specimens.

The prepared pillar specimens had a middle diameter ranging from 150 nm and up to 5  $\mu\text{m}$ , while the cantilever fracture mechanical specimens had a length from 4  $\mu\text{m}$  to 20  $\mu\text{m}$ . Only the base metal prepared specimens were loaded in the nanoindentation device. During the loading force and displacement data was recorded and for the pillar specimens converted to stress and strain curves. Before and after the test there were taken SEM images of the specimens which were used to evaluate the deformation of the specimens.

The aim was to determine if the FIB method can be used to determine local behavior and material properties of a complex commercial steel. Material models, such as the double-barrier model, indicates that locale properties have a key role to understand brittle fracture mechanisms that occurs for steels under specific conditions. FIB fabrication done in this study has showed that it is possible to produce micro sized specimen from a small grained commercial steel. Specimens within martensitic containing grains were prepared but not tested. The varying microstructure complicates the milling process, but specimens are clearly possible to prepare.

If the work done in this thesis should be extended further development of a better preparation procedure, including appropriate jigs and holders, should be made. Use of crystallographic techniques such as EBSD mapping will give important supplementary information of the tested microstructure and reveal possible variations and reduce scatter due to crystallography. The instrumentation during nanoindentation loading is currently not able to do testing at  $-60\text{ }^{\circ}\text{C}$ . When testing at lower temperature is possible in the nanoindentation system the ductile-to-brittle transition can be documented at microsized specimens. In a wider setting the FIB techniques have showed large range of application in form of simple contrast images to advanced 3D characterization with EBSD mapping and 3D reconstruction.





## References

- [1] S. M. Allameh. An introduction to mechanical-properties-related issues in MEMS structures. *Journal of Materials Science*, 38(20):4115–4123, 2003.
- [2] T. L. Anderson. *Fracture Mechanics. Fundamentals and Applications*. Boca Raton, Fla.: Taylor and Francis, 3 edition, 2005. 621 p.
- [3] D. E. J. Armstrong, M. E. Rogers, and S. G. Roberts. Micromechanical testing of stress corrosion cracking of individual grain boundaries. *Scripta Materialia*, 61(7):741–743, 2009.
- [4] S. P. Astad. Mikrostruktur og mekaniske eigenskapar i eit aktiskt stål. Project work, Norwegian University of Science and Technology, 2009.
- [5] O. K. Bjering. Muligheter for bruk av in-situ testing av sprekkvekst i stål. Project work, Norwegian University of Science and Technology, 2009.
- [6] Y. L. Chan, A. H. W. Ngan, and N. M. King. Use of focused ion beam milling for investigating the mechanical properties of biological tissues: A study of human primary molars. *Journal of the Mechanical Behavior of Biological Materials*, 2(4):375–383, 2009.
- [7] FEI Company. *Helios NanoLab 400/400S/400 ML/600 System User's Guide*, pn 4022-262-95793-a edition.
- [8] T. Connolley, P. E. McHugh, and M. Bruzzi. A review of deformation and fatigue of metals at small size scales. *Fatigue & Fracture of Engineering Materials & Structures*, 28(12):1119–1152, 2005.
- [9] C. L. Davis and J. E. King. Cleavage Initiation in the Intercritically Reheated Coarse-Grained Heat-Affected Zone: Part I. Fractographic Evidence. *Metallurgical and Materials Transactions A*, 25:563–573, 1994.
- [10] R. F. Egerton. *Physical Principles of Electron Microscopy: An Introduction to TEM, SEM, and AEM*. Boston, MA: Springer Science+Business Media, Inc., 2005. 202 pages.
- [11] F. Eggert. Some Information about Element Distributions Mapping, Element-Imaging and ColorSEM. Downloaded 20. May 2010. <http://microanalyst.mikroanalytik.de/info7.phtml>.
- [12] L. A. Giannuzzi. *Introduction to Focused Ion Beams: Instrumentation, Theory, Techniques and Practice*. Boston, MA: Springer Science+Business Media, Inc., 2005. 357 pages.

- [13] J. Gong and A. J. Wilkinson. Anisotropy in the plastic flow properties of single-crystal  $\alpha$  titanium determined from micro-cantilever beams. *Acta Materialia*, 57(19):5693–5705, 2009.
- [14] IBM. Focused ion beam. Hentet fra nettside 28. april 2010. [http://www.absoluteastronomy.com/topics/Focused\\_ion\\_beam](http://www.absoluteastronomy.com/topics/Focused_ion_beam).
- [15] IBM. Focussed Ion Beam (FIB). Hentet fra nettside 10. april 2010. [http://www.almaden.ibm.com/st/scientific\\_services/materials\\_analysis/fib/](http://www.almaden.ibm.com/st/scientific_services/materials_analysis/fib/).
- [16] N. Kheradmand. Micropillars Compression Test. Master’s thesis, Universität des Saarlandes, 2007.
- [17] N. Kheradmand, A. Barnoush, and H. Vehoff. Investigation of the role of grain boundary on the mechanical properties of metals. *Open Access proceedings Journal of Physics: Conference series*, 2009.
- [18] D. Kiener, C. Motz, and G. Dehm. Dislocation-induced crystal rotations in micro-compressed single crystal copper columns. *Journal of Materials Science*, 43(7):2503–2506, 2008.
- [19] D. Kiener, C. Motz, and G. Dehm. Micro-compression testing: A critical discussion of experimental constraints. *Materials Science and Engineering A-Structural Materials: Properties, Microstructure and Processing*, 505(1-2):79–87, 2009.
- [20] A. Lambert-Perlade, A. F. Gourgues, J. Besson, T. Sturel, and A. Pineau. Mechanisms and Modeling of Cleavage Fracture in Simulated Heat-Affected Zone Microstructures of a High-Strength Low Alloy Steel. *Metallurgical and Materials Transactions A*, 35:1039–1053, 2004.
- [21] R. E. Loehman and P. G. Kotula. Spectral imaging analysis of interfacial reactions and microstructures in brazing of alumina by a Hf-Ag-Cu alloy. *Journal of the American Ceramic Society*, 87(1):55–59, 2004.
- [22] K. Matoy, H. Schoenherr, T. Detzel, T. Schoeberl, R. Pippan, C. Motz, and G. Dehm. A comparative micro-cantilever study of the mechanical behavior of silicon based passivation films. *Thin Solid Films*, 518(1):247–256, 2009.
- [23] SYNTON MDP. Micro Diamond Points. Downloaded 2. June 2010. <http://www.synton-mdp.ch/images/produkte/berkovich.jpg>.
- [24] SYNTON MDP. Micro Diamond Points. Downloaded 2. June 2010. <http://www.synton-mdp.ch/images/produkte/flattop.jpg>.

- [25] SYNTON MDP. MICRO DIMOND POINTS. Downloaded 2. June 2010. <http://www.synton-mdp.ch/images/produkte/keilschliff.jpg>.
- [26] B. R. Rogne and C. Thaulow. Preparation of pillars and fracture mechanics steel specimens with FIB and testing in nanoindenter. In *Nanobrücken Nanomechanical Testing Workshop And Hysitron User Meeting*, INM Saarbrücken, Germany, February 25–26, 2010.
- [27] A. S. Schneider, D. Kaufmann, B. G. Clark, C. P. Frick, P. A. Gruber, R. Moenig, O. Kraft, and E. Arzt. Correlation between critical temperature and strength of small-scale bcc pillars. *Physical Review Letters*, 103(10), 2009.
- [28] A. J. Schwartz, M. Kumar, B. L. Adams, and D. P. Field. *Electron Backscatter Diffraction in Materials Science*. Boston, MA: Springer Science+Business Media, Inc., 2 edition, 2009. 403 pages.
- [29] E. Østby. State-of-the-art of models and treatment of brittle fracture in steels. *SINTEF Report*, 2007. 43 s.
- [30] Nippon Steel. *Inspection Certificate*. 2008.
- [31] K. Takashima, M. Shimojo, Y. Higo, and M. V. Swain. Fatigue Crack Growth of a Ni-P Amorphous Alloy Thin Film. In C. L. Muhlstein and S. B. Brown, editors, *Mechanical Properties of Structural Films ASTM STP 1413*, pages 52–61. West Conshohocken, Pa.: ASTM, 2001.
- [32] K. Takashima, M. Shimojo, Y. Higo, and M. V. Swain. Fracture Behavior of Micro-Sized Specimens with Fatigue Pre-Crack Prepared from a Ni-P Amorphous Alloy Thin Film. In C. L. Muhlstein and S. B. Brown, editors, *Mechanical Properties of Structural Films ASTM STP 1413*, pages 72–81. West Conshohocken, Pa.: ASTM, 2001.
- [33] E. Taki, Y. Kawakami, M. Otsu, and K. Takashima. Fracture Behavior of Micro-Sized Fe-3%Si Alloy Single Crystals. *Journal of Solid Mechanics and Materials Engineering*, 1(6):779–786, 2007.
- [34] M. D. Uchic and D. A. Dimiduk. A methodology to investigate size scale effects in crystalline plasticity using uniaxial compression testing. *Materials Science and Engineering A—Structural Materials: Properties, Microstructure and Processing*, 400:268–278, 2005.
- [35] M. D. Uchic, P. A. Shade, and D. M. Dimiduk. Plasticity of Micrometer-Scale Single Crystals in Compression. *Annual Review of Materials Research*, 39:361–386, 2009.

- [36] C. A. Volkert and E. T. Lilleodden. Size effects in the deformation of sub-micron au columns. *Philosophical Magazine*, 86(33–35):5567–5579, 2006.
- [37] C. A. Volkert and A. M. Minor. Focused Ion Beam Microscopy and Micro-machining. *MRS bulletin*, 32:389–395, 2007.
- [38] Wikipedia. Energy-dispersive X-ray spectroscopy. Downloaded 18. May 2010. <http://upload.wikimedia.org/wikipedia/commons/9/9f/EDX-scheme.svg>.
- [39] G. P. Zhang, K. Takashima, and Y. Higo. Fatigue strength of small-scale type 304 stainless steel thin films. *Materials Science and Engineering A–Structural Materials: Properties, Microstructure and Processing*, 426(1–2):95–100, 2006.
- [40] X. Zhao, R. M. Langford, J. Tan, and P. Xiao. Mechanical properties of SiC coatings on spherical particles measured using the micro-beam method. *Scripta Materialia*, 59(1):39–42, 2008.

## Appendix

### A Poster Abstract

Nanobrücken – February 25-26, 2010

#### POSTER - NO 26

#### PREPARATION OF PILLARS AND FRACTURE MECHANICS STEEL SPECIMENS WITH FIB AND TESTING IN NANOINDENTER

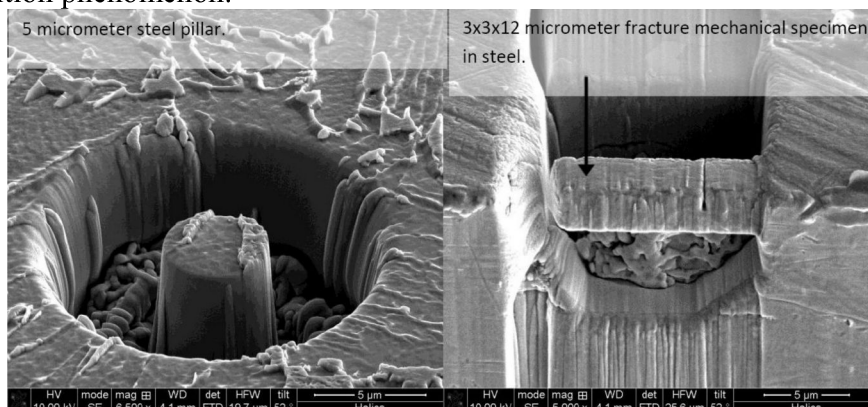
Bjørn Rune Rogne and Christian Thaulow

Norwegian University of Science and Technology, Trondheim, Norway

Through the master's thesis we will investigate the machining and subsequently loading of micro sized pillars and fracture mechanical specimens in HSLA steel for Arctic and cold conditions. The goal is to investigate the local material properties of steel and their brittle phases, and also to determine the need of this type of steel investigation in the future. In the last years fabrication of micro sized pillars by using FIB (Focused Ion Beam) is extensive in use, mainly in pure metals. By using a nanoindenter to load the pillars, micromechanical parameters can be obtained.

The same procedure is also possible for fracture mechanical specimens, gaining micro fracture mechanical properties. At this time effort in qualifying high strength low alloy (HSLA) steel for Arctic and cold conditions are being done. The heat treatment due to welding combined with low temperatures makes the steel brittle. Fracture mechanical samples with different geometries and weld simulated microstructure are tested to quantify the fracture toughness properties. Existence of hard and brittle phases, mainly martensite, in a ductile surrounding material is one of the expected reasons for the brittleness. To understand the role of brittle phases, detection of acoustic emission (AE) is being used simultaneous with the fracture mechanical testing.

Currently FIB preparation of steel specimens seems feasible and the first specimens have been made. Still further optimizing of fabrication is necessary. Loading of pillars will be done with a flat punch tip in the nanoindenter, hopefully with simultaneously AE monitoring. Fracture mechanical specimens are loaded with a Berkovich tip. The local material properties will be compared with the macro properties in order to gain insight in the Brittle-to-Ductile transition phenomenon.



5 micrometer steel pillar

3x3x12 micrometer fracture mechanical specimen in steel.

## B Load Estimate

The nanoindenter used is limited to a max load of 10 mN. The material is also expected to locally have high yield strength values compared to idealized micro structures that mostly are investigated in the literature. Yield strength and ultimate tensile strength of the base metal plate of the investigated steel is respectively 514 MPa and 606 MPa [30]. This estimate should quantify the dimensional limit where the nanoindenter is not able to load the specimen until yield. For simplicity no work hardening or size effects is accounted for.

### B.1 Pillar

The pillars expect to start deforming when the stress reaches yield. This happens when  $\sigma_{ys} = \frac{4F}{\pi D^2}$ . In Figure 58 the equation is plotted for yield stresses of 300, 400, 500, 600 and 700 MPa. At  $F = F_{max}$  the maximum expected pillar diameter of

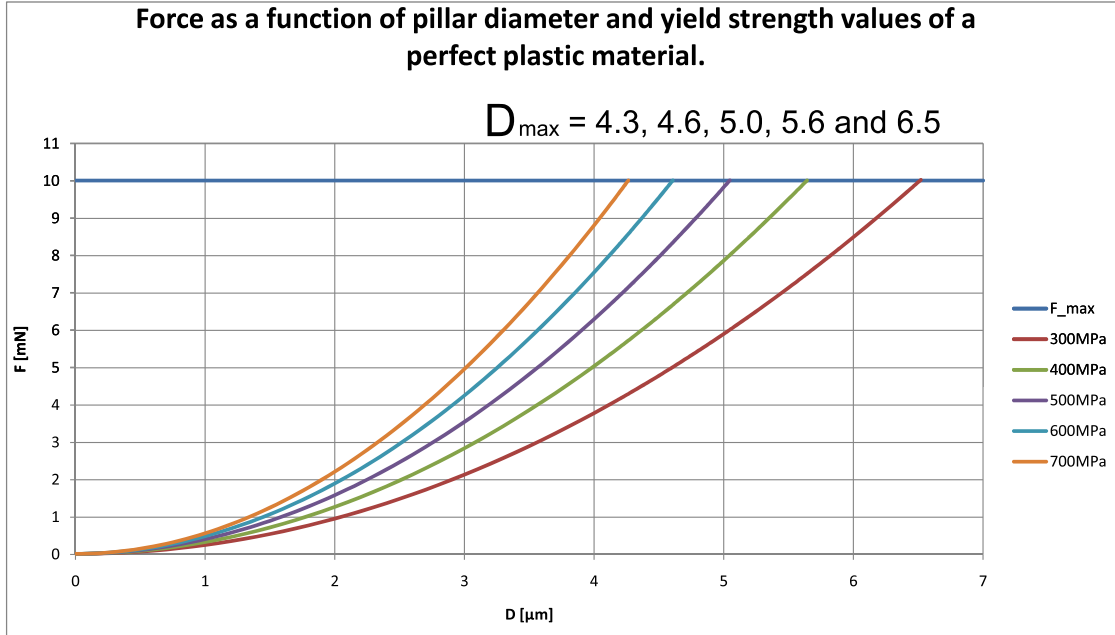


Figure 58: Pillar load curves for yield stresses of 300, 400, 500, 600 and 700 MPa. The max load of 10 mN is limited by the nanoindenter loading capacity.

the current yield stress is obtain. The diameter limits of the different yield stresses can be seen in the Figure 58. Doing the same calculations for the yield strength of 514 MPa and the ultimate tensile strength of 606 MPa the respectively maximum diameter values found is 5.0 and 4.6  $\mu\text{m}$ .

## B.2 Cantilever

Cantilever specimen geometry is defined in Figure 59. In the estimate the param-

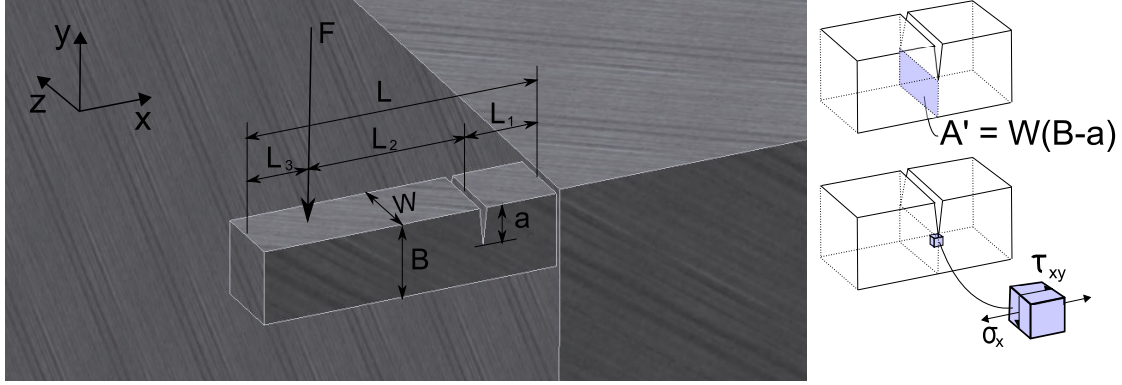


Figure 59: Illustration of the cantilever geometry and loading point.

eters is reduced by setting  $B = W$ ,  $a = W/2$ ,  $L_1 = W$ ,  $L_2 = 2W$  and  $L_3 = W$ . This gives a total length of  $L = 4W$ . Further it is assumed that yield occurs at the crack tip when  $\sigma_{\text{Mises}} = \sigma_{ys}$ . The plane stress relation is given in Equation (8).

$$\sigma_{\text{Mises}} = \sqrt{\sigma_x^2 + \sigma_y^2 - \sigma_x\sigma_y + 3\tau_{xy}^2} \quad (8)$$

The stress at a small element at the crack tip will examine a plane stress condition defined in Equation (9). By combining Equation (8) and Equation (9), Equation (10) is obtained.

$$\sigma_x = \frac{M}{I_x} y_{\text{CrackTip}} = \frac{6FL_2}{W(B-a)^2}, \quad \sigma_y = 0, \quad \tau_{xy} = \frac{F}{A'} = \frac{F}{(B-a)W} \quad (9)$$

$$\sigma = \sqrt{2316} \frac{F}{W} \quad (10)$$

The results of the calculations is plotted in Figure 60.  $W_{max}$  is the maximum  $W$  at  $F_{max}$  for a corresponding yield strength value. Yield strength of 300, 400, 500, 600 and 700 MPa gives respectively the corresponding 26.2, 28.3, 31.0, 34.7 and 40.1  $\mu\text{m}$  maximum width. The same calculations for the base metal yield strength and ultimate tensile strength gives  $W_{max}$  values of 30.6 and 28.2  $\mu\text{m}$ .

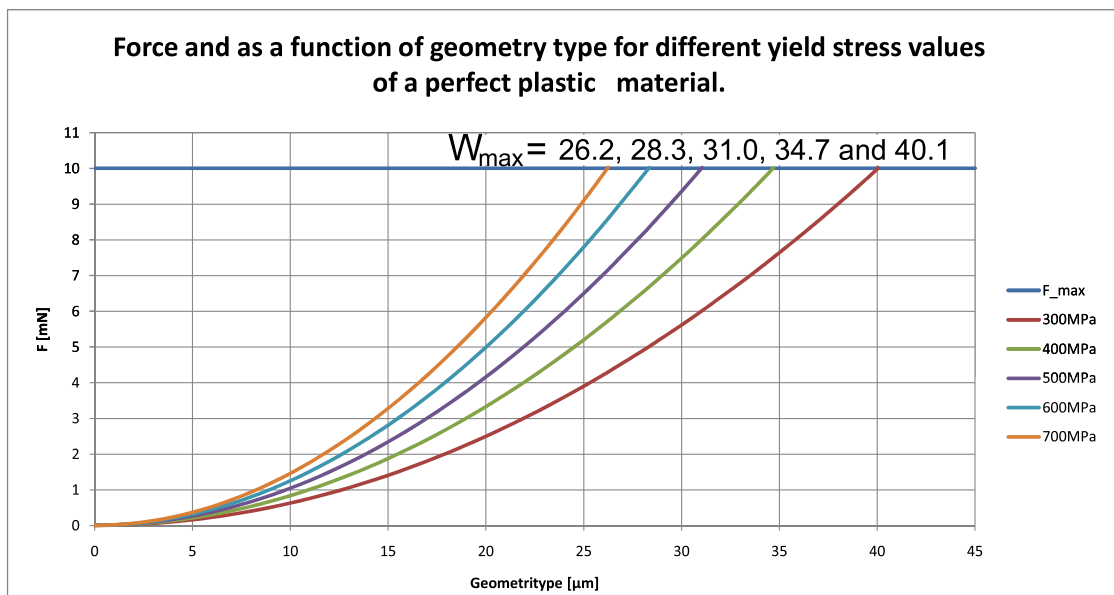
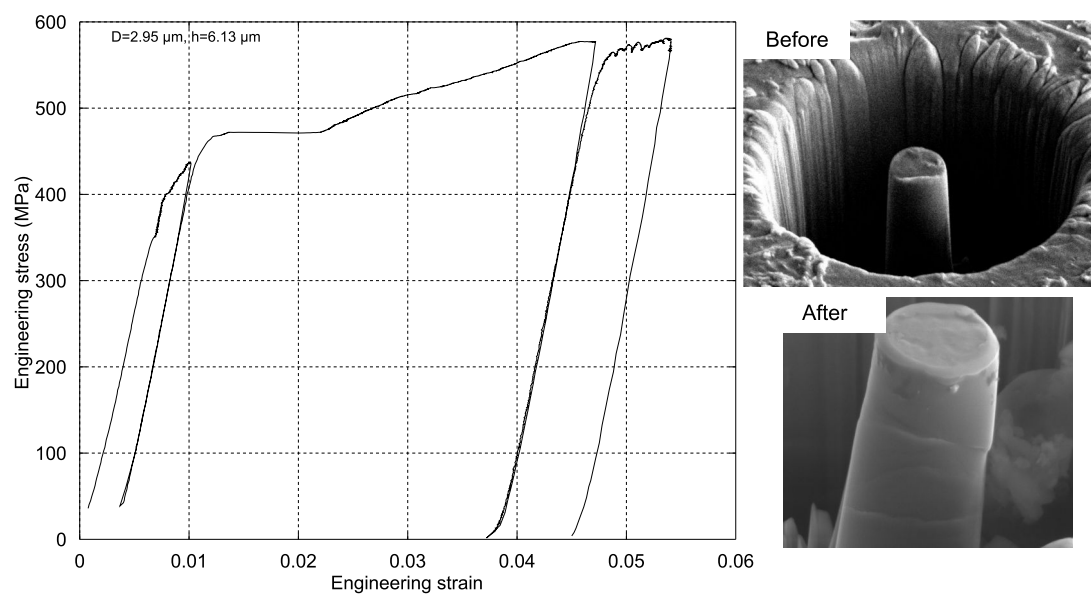


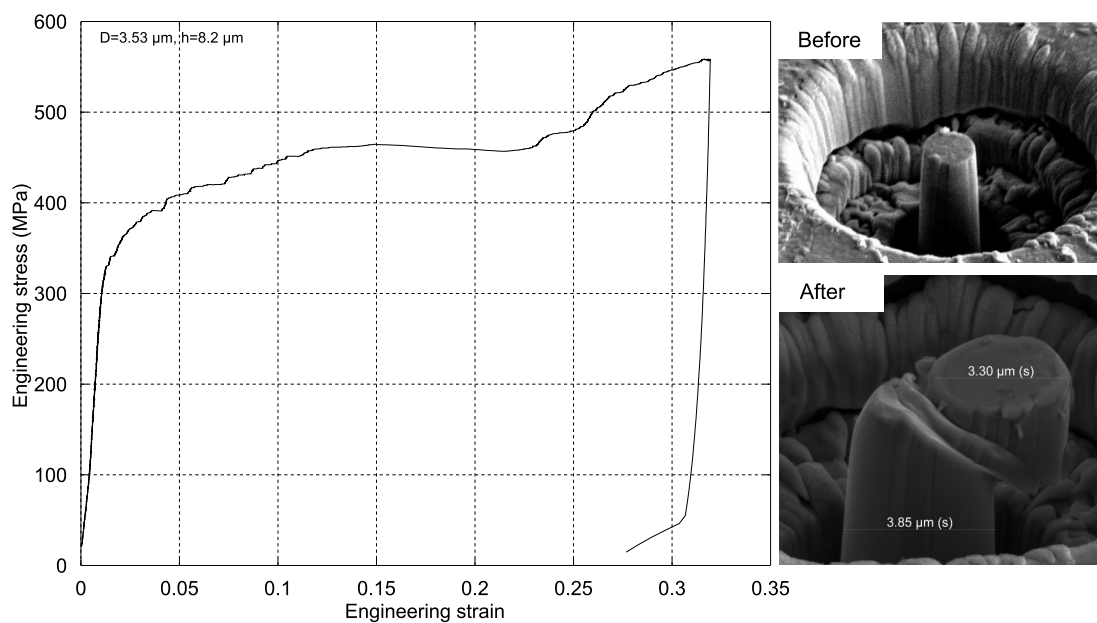
Figure 60: Cantilever load curves for yield stresses of 300, 400, 500, 600 and 700 MPa. The max load of 10 mN is limited by the nanoindenter loading capacity.



## C Test Data of Pillar Series 100

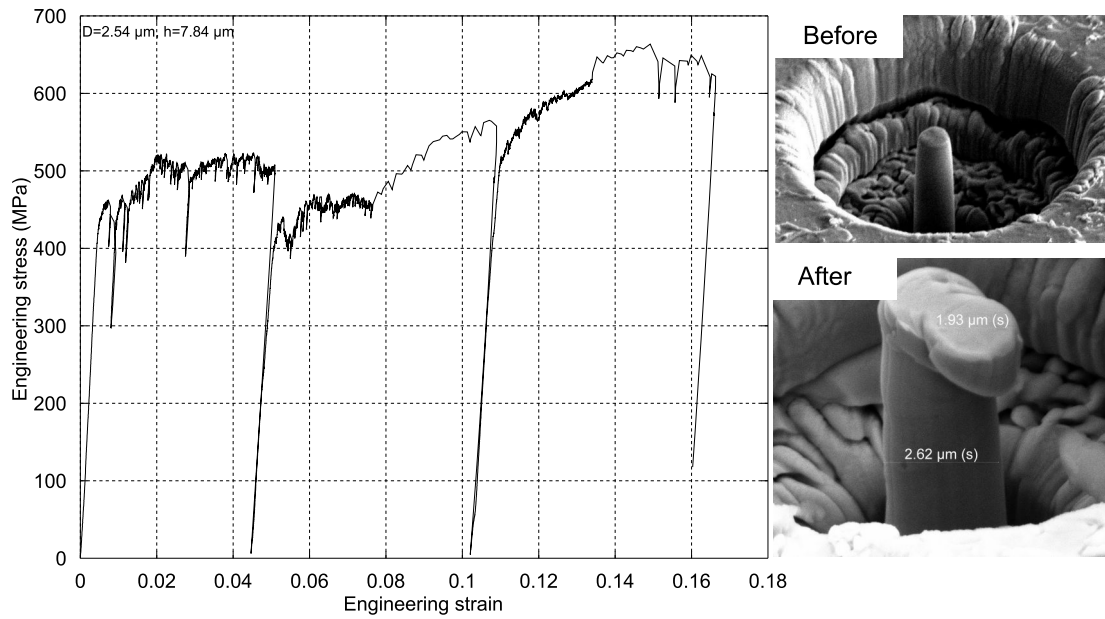


(a) Pillar 101.

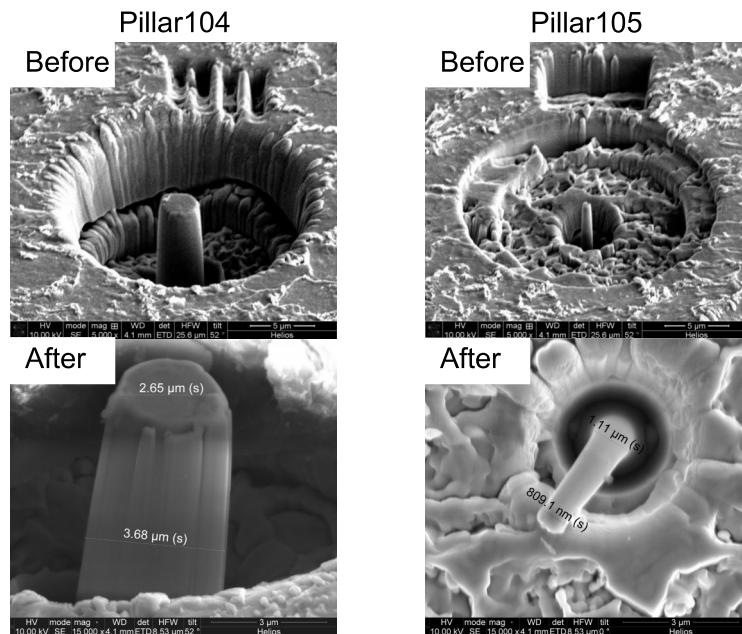


(b) Pillar 102.

Figure 61: Pillar 101 and 102.

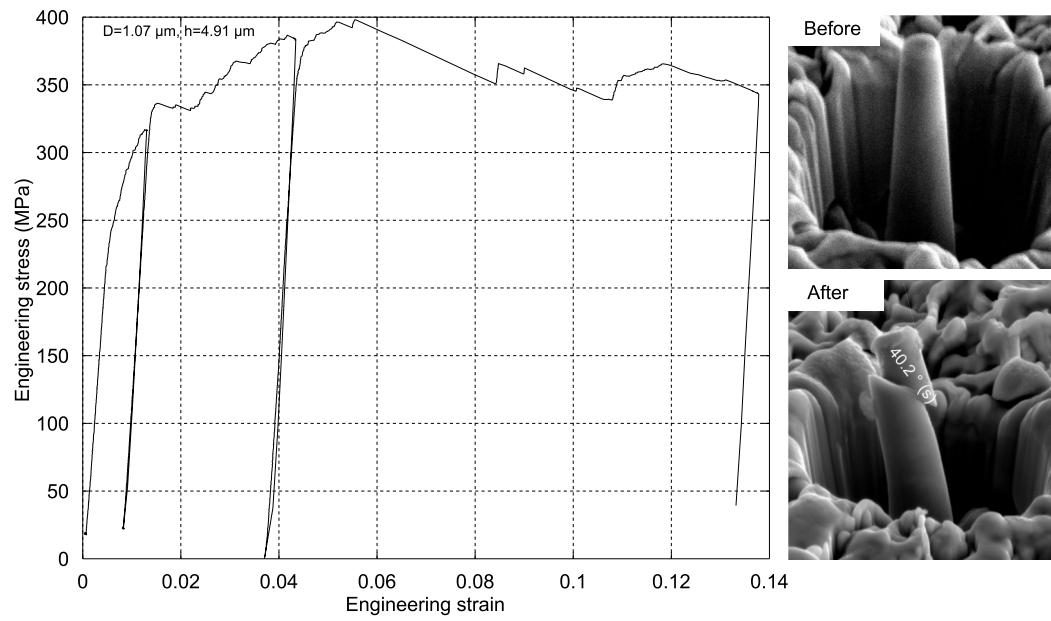


(a) Pillar 103. Displacement controlled test.

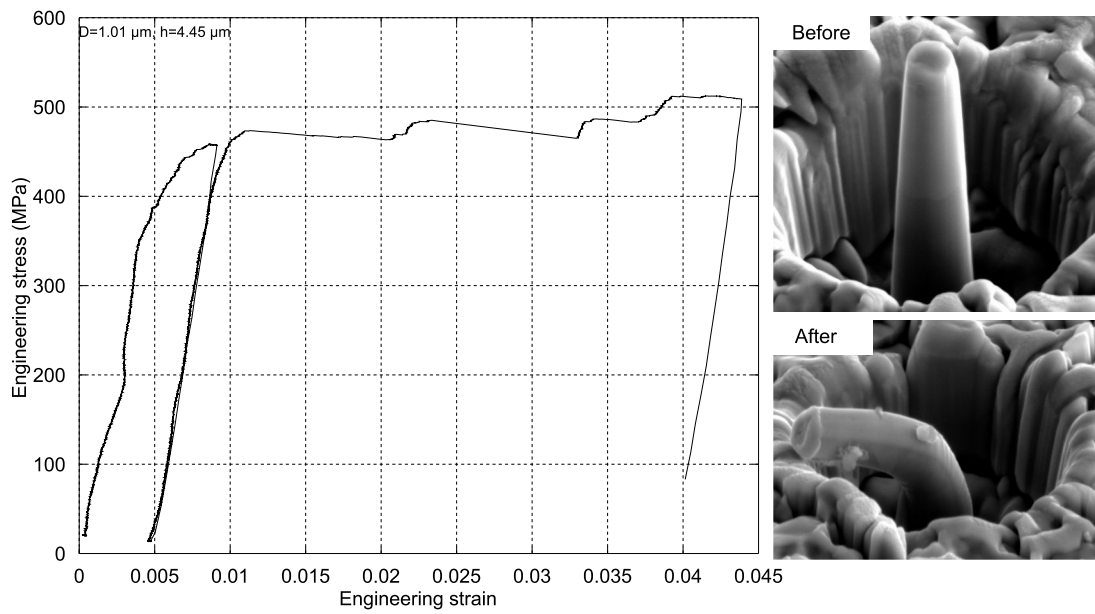


(b) Pillar 104 and 105.

Figure 62: Pillar 103, 104 and 105.

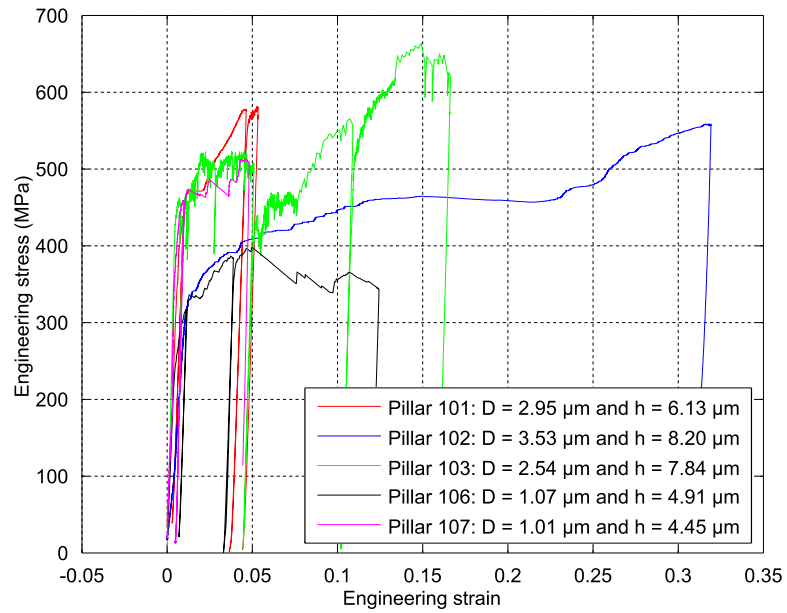


(a) Pillar 106.

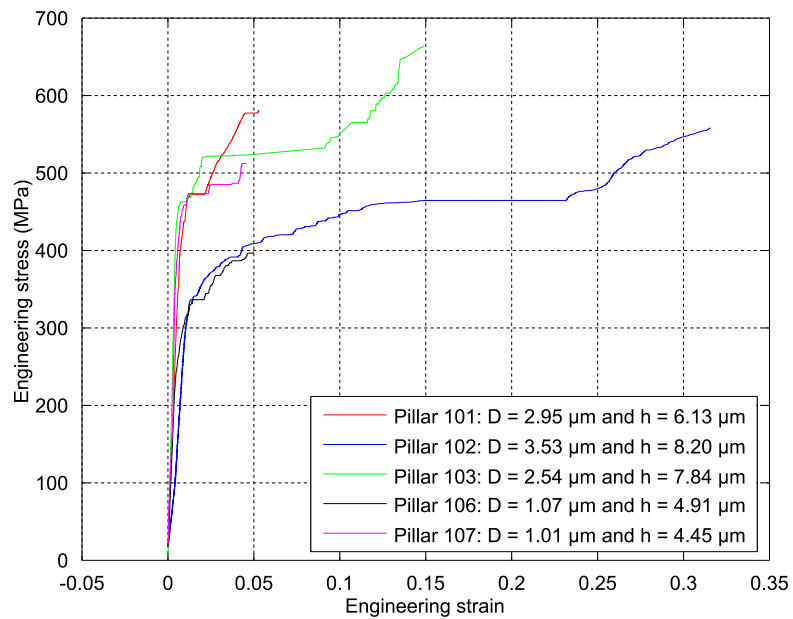


(b) Pillar 107.

Figure 63: Pillar 106 and 107.



(a) Pillar series 100 overview.



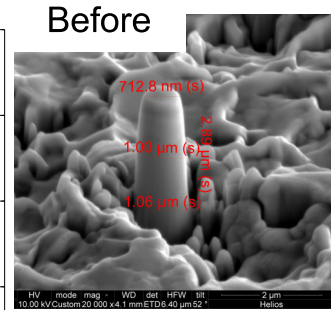
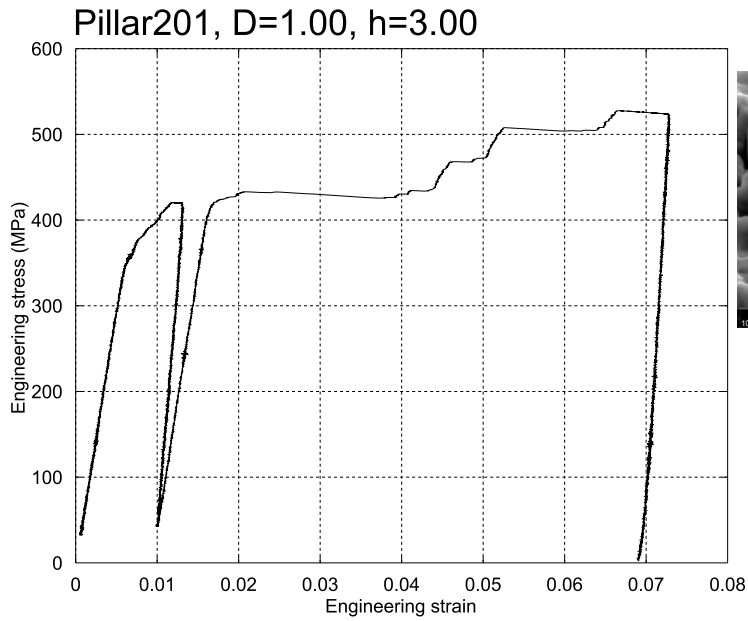
(b) Pillar series 100 overview. Showing increasing trend.

Figure 64: Pillar overview showing increasing trend. Decreasing values are removed from the plot.

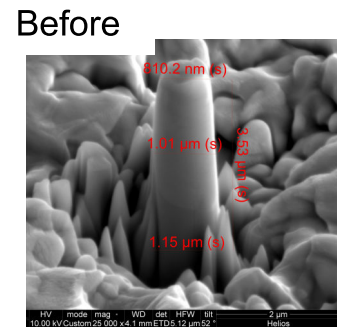
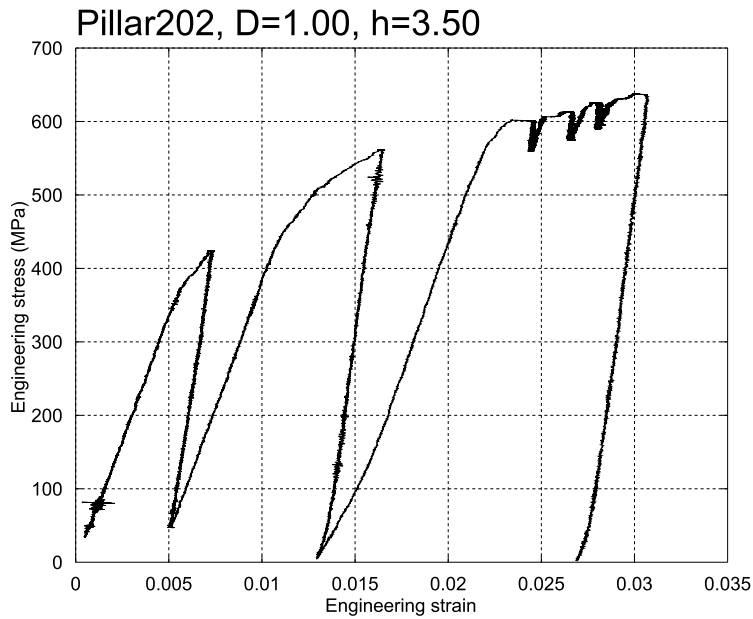
Figure 65: Pillar series 100 data.

Pillar	101	102	103	104	105	106	107	Maksimum	Minimum	Average
D [ $\mu\text{m}$ ]	3.0	3.5	2.5	3.4	0.87	1.1	1.0	3.5	1.0	2.2
H [ $\mu\text{m}$ ]	6.1	8.2	7.8	8.3	4.6	4.4	4.9	8.2	4.448	6.3
H/D	2.1	2.3	3.1	2.4	5.3	4.2	4.9	4.9	2.1	3.3
Area [ $\mu\text{m}^2$ ]	6.83	9.79	5.07	-	-	0.899	0.801	9.79	0.801	4.68
Surface area [ $\mu\text{m}^2$ ]	16.10	20.88	13.05	-	-	4.26	3.97	20.88	3.97	11.65
Volume [ $\mu\text{m}^3$ ]	41.90	80.25	39.73	-	-	4.00	3.93	80.25	3.93	33.96
Slope 1	55 575	34 451	96 482	-	-	48 679	82 039	96 482	34 451	63 445
Slope 2	62 701	-	78 746	-	-	56 119	98 277	98 277	56 119	73 961
Slope 3	62 125	-	67 112	-	-	58 411	-	67 112	58 411	62 549
0.1 % plastic strain	414	315	446	-	-	254	388	446	254	364
2 % elastic and plastic strain	471	357	515	-	-	333	465	515	333	428
2 % plastic strain	514	386	498	-	-	352	474	514	352	445
4 % elastic and plastic strain	554	391	519	-	-	384	511	554	384	472
4 % plastic strain	567	410	506	-	-	388	-	567	388	468
Stress [MPa] Defined at:										

## D Test Data of Pillar Series 200

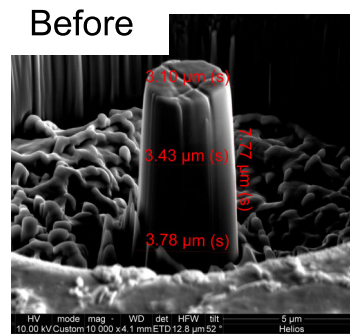
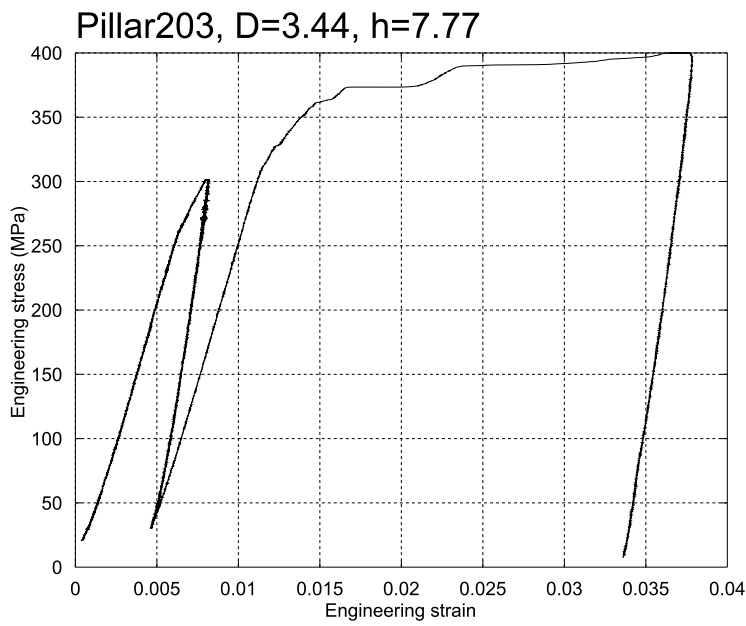


(a) Pillar 201.

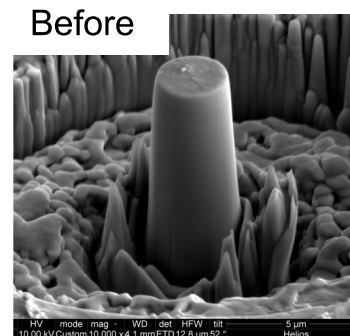
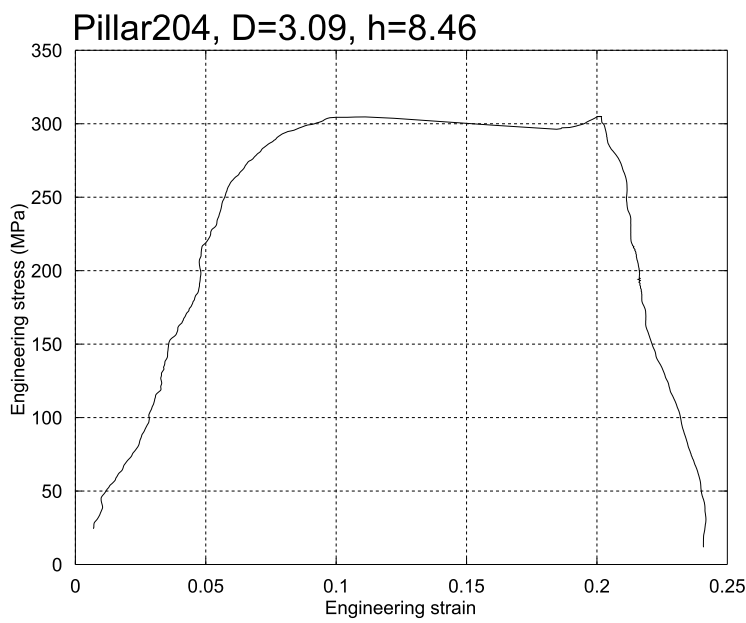


(b) Pillar 202.

Figure 66: Pillar 201 and 202.

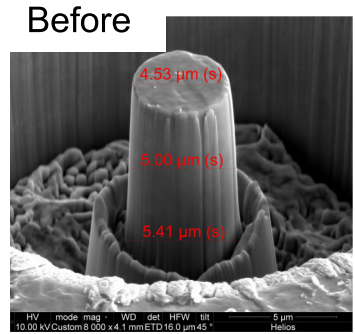
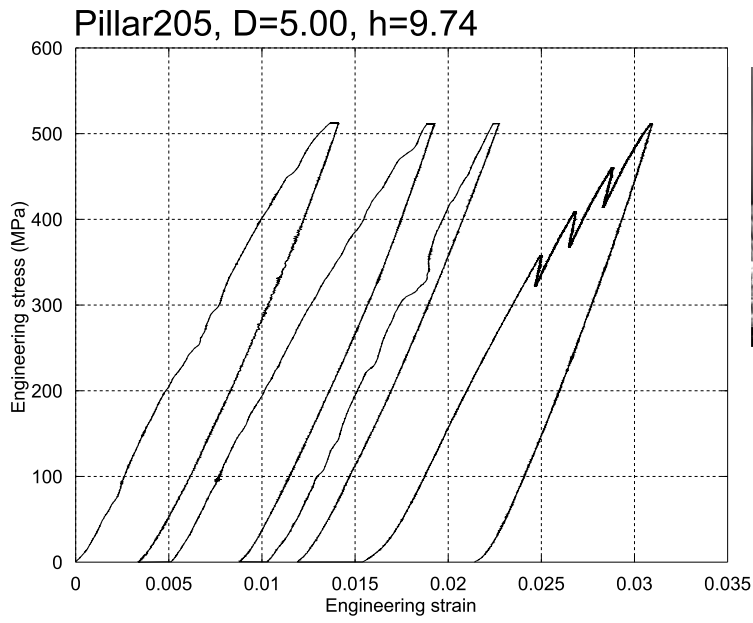


(a) Pillar 203.

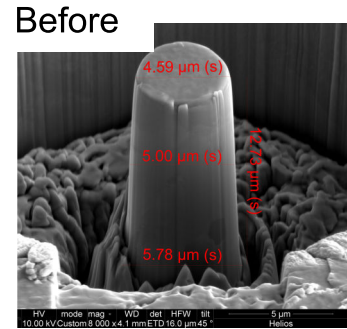
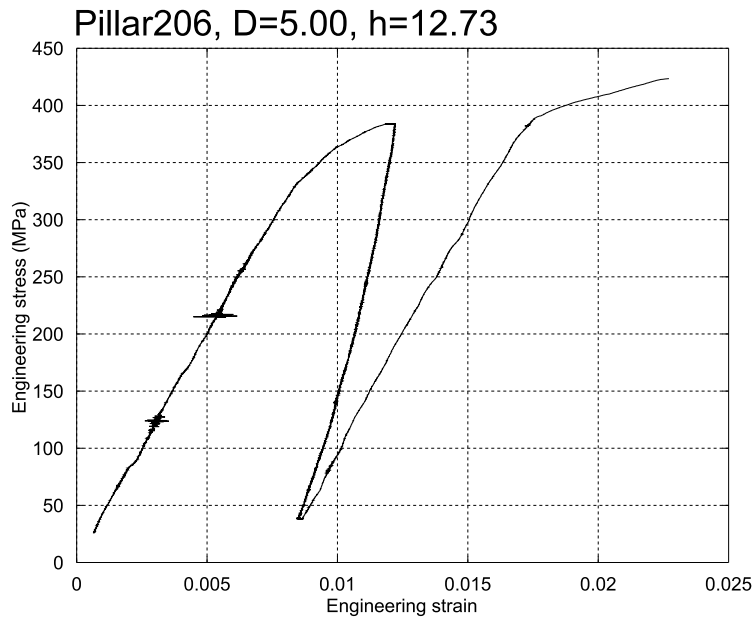


(b) Pillar 204.

Figure 67: Pillar 203 and 204.



(a) Pillar 205.

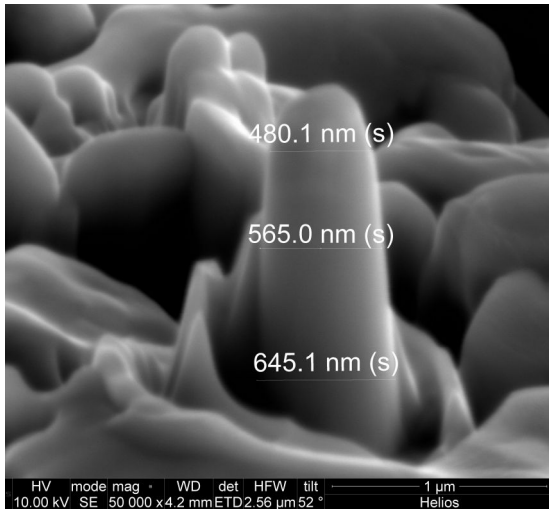


(b) Pillar 206.

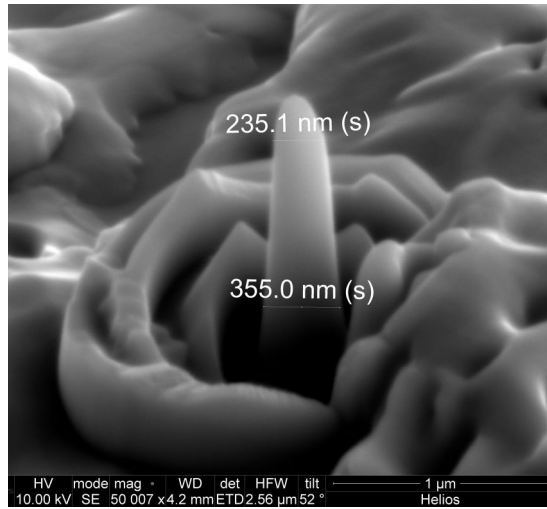
Figure 68: Pillar 205 and 206.



Pillar207



Pillar208



Pillar210

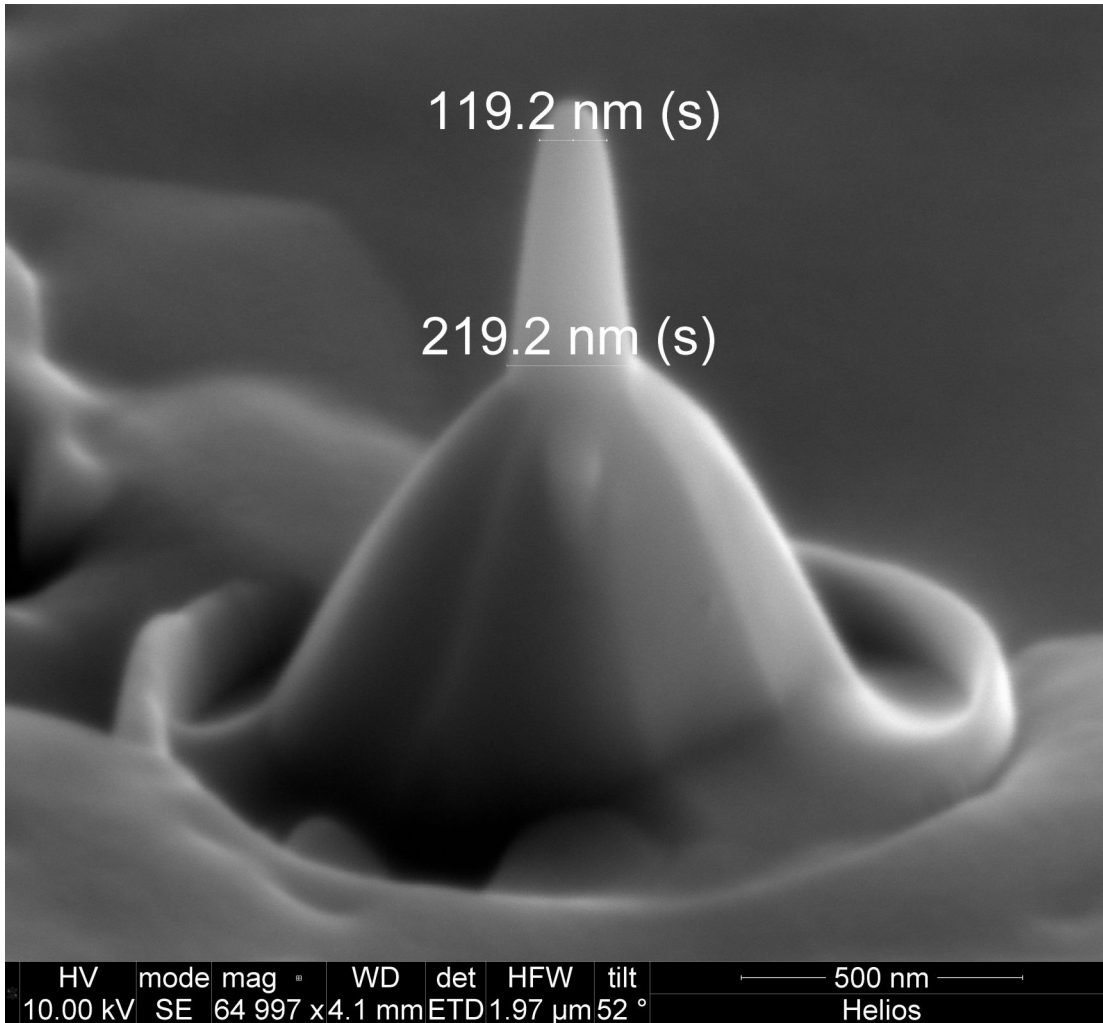
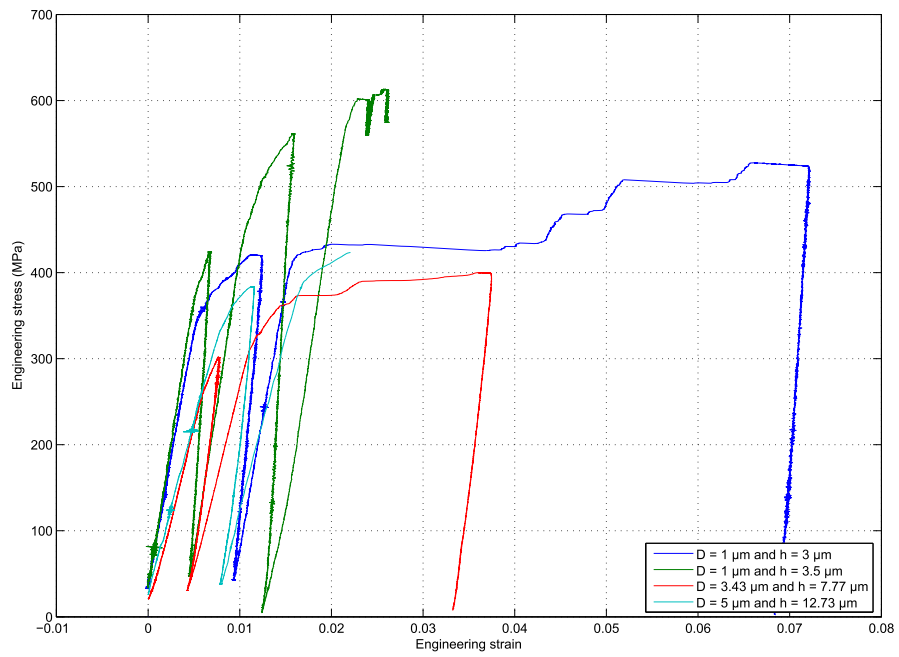
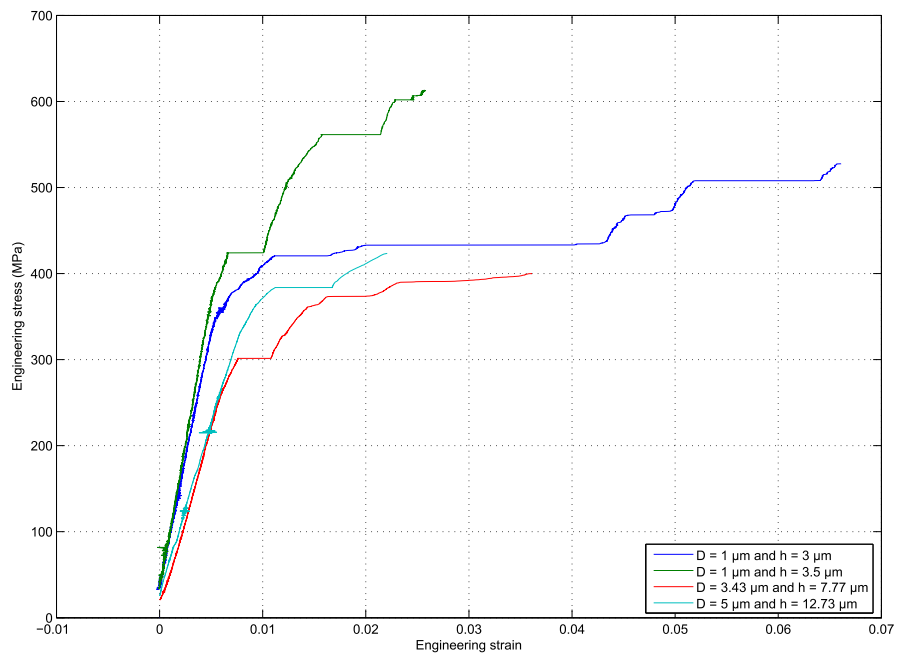


Figure 69: Pillar 207, 208 and 210.



(a) Pillar series 200 overview.



(b) Pillar series 200 overview. Showing increasing trend.

Figure 70: Stress and strain plot of pillar series 200.

Figure 71: Pillar series 200 data.

Pillar	201	202	203	204	205	206	207	208	210	Maksimum	Minimum	Average
D [ $\mu\text{m}$ ]	1.0	1.0	3.4	3.1	5.0	5.0	0.57	0.29	0.17	5.0	0.17	2.2
H [ $\mu\text{m}$ ]	3.0	3.5	7.8	8.5	9.7	12.7	1.8	1.5	0.55	12.7	0.55	5.5
H/D	3.0	3.5	2.3	2.7	1.9	2.5	3.2	5.2	3.2	5.2	1.9	3.1
Area [ $\mu\text{m}^2$ ]	0.79	0.79	9.2	7.5	19.6	19.6	-	-	-	19.6	0.79	9.6
Surface area [ $\mu\text{m}^2$ ]	3.9	3.9	20.0	17.2	35.3	35.3	-	-	-	35.3	3.9	19.3
Volume [ $\mu\text{m}^3$ ]	2.4	2.7	71.8	63.4	191.2	250.0	-	-	-	250.0	2.4	96.9
Slope 1	59 452	67 208	43 267	-	37 020	39 662	-	-	-	67 208	37 020	49 322
Slope 2	60 318	38 615	42 476	-	39 979	39 979	-	-	-	60 318	38 615	44 273
Slope 3	-	63 387	-	-	43 311	-	-	-	-	63 387	43 311	53 349
0.1 % plastic strain	367	424	304	-	-	365	-	-	-	424	304	365
2 % elastic and plastic strain	431	~570	374	-	-	407	-	-	-	431	374	404
2 % plastic strain	430	631	391	300	>509	-	-	-	-	631	300	438
4 % elastic and plastic strain	430	-	-	-	-	-	-	-	-	430	430	430
4 % plastic strain	468	-	-	301	-	-	-	-	-	468	301	385
Stress [MPa] defined at:												

E Test Data of FM Series 100

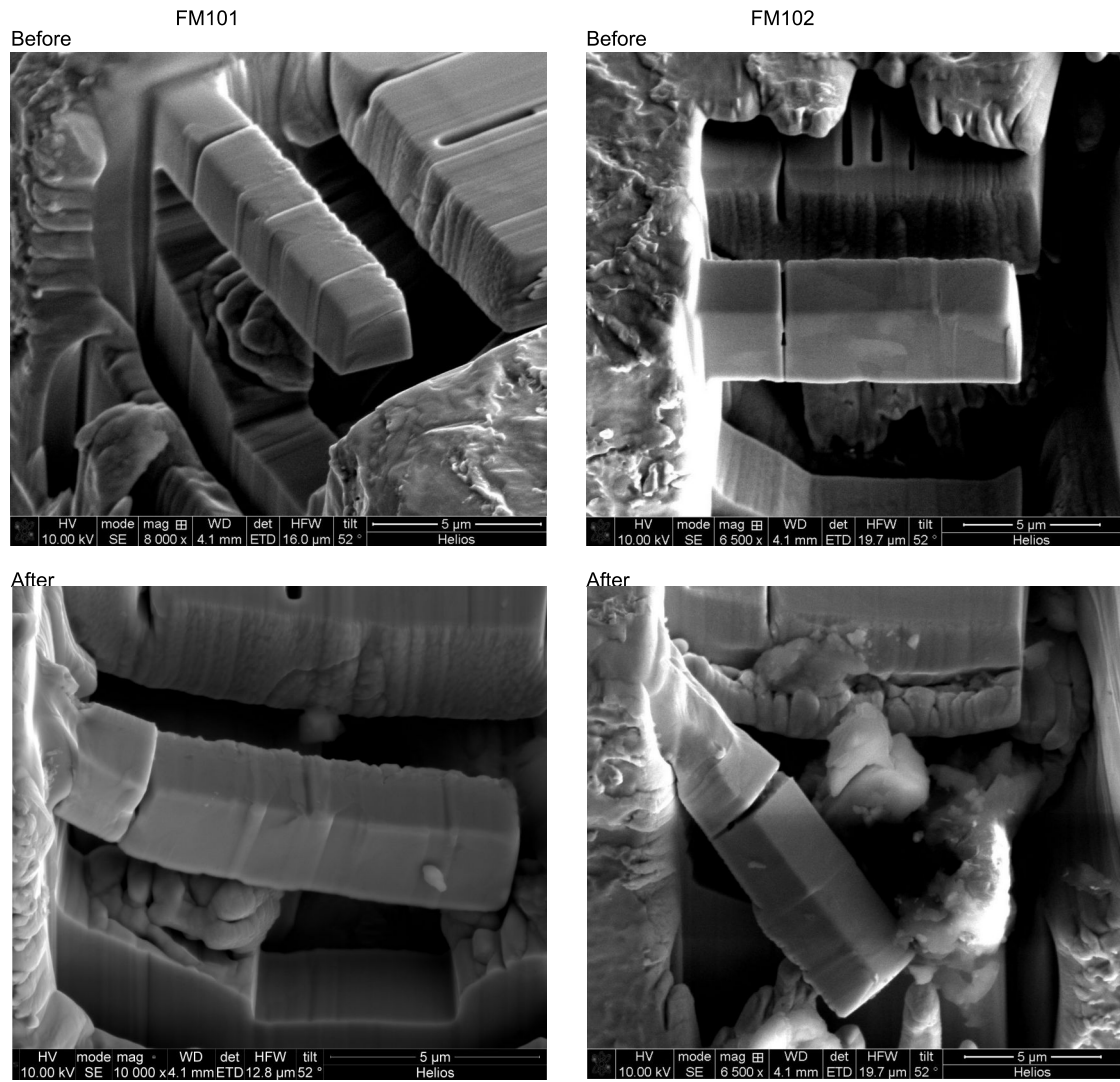
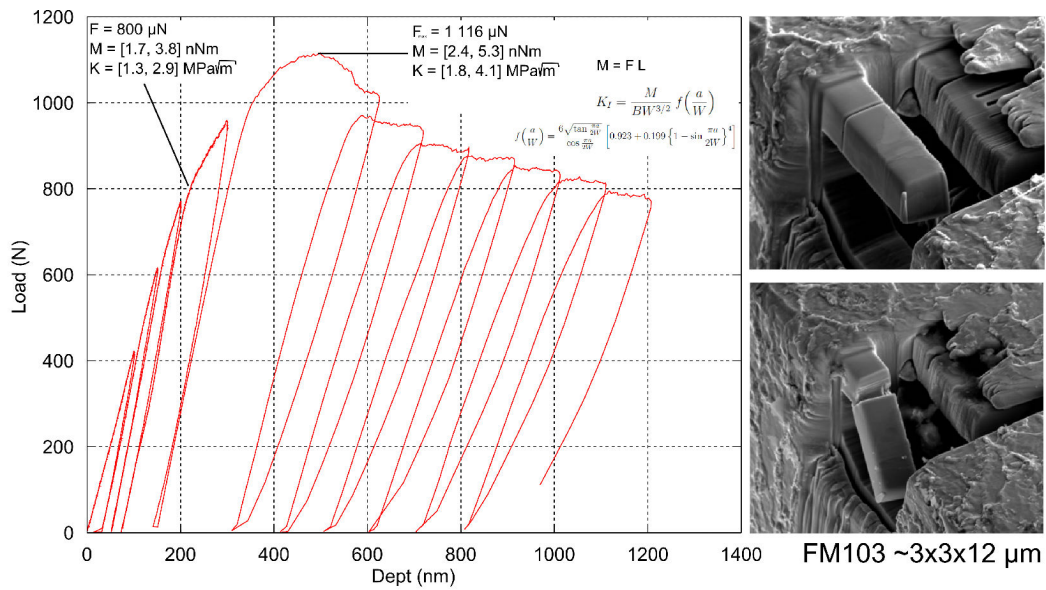
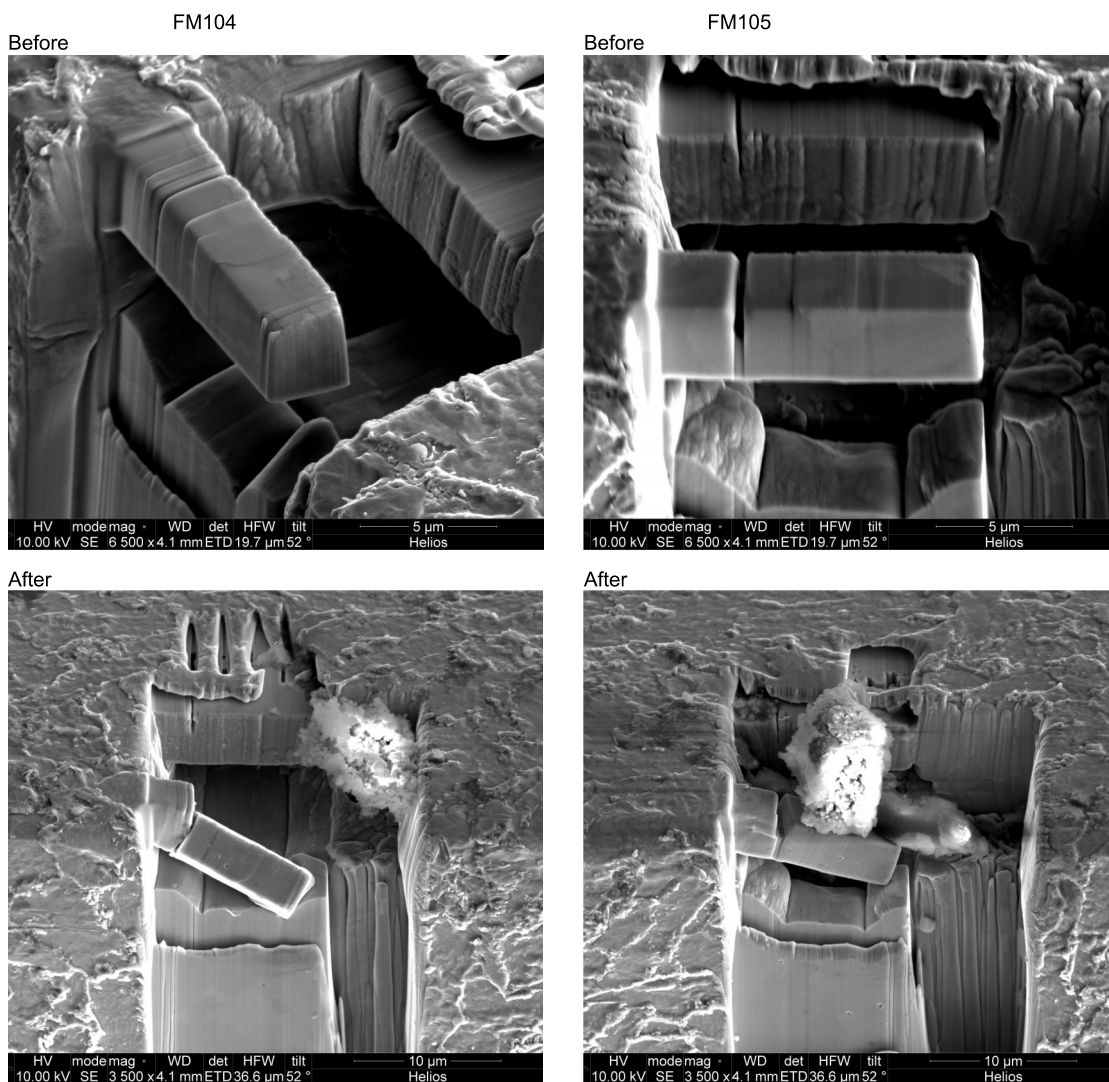


Figure 72: FM101 and FM102.



(a) FM103.

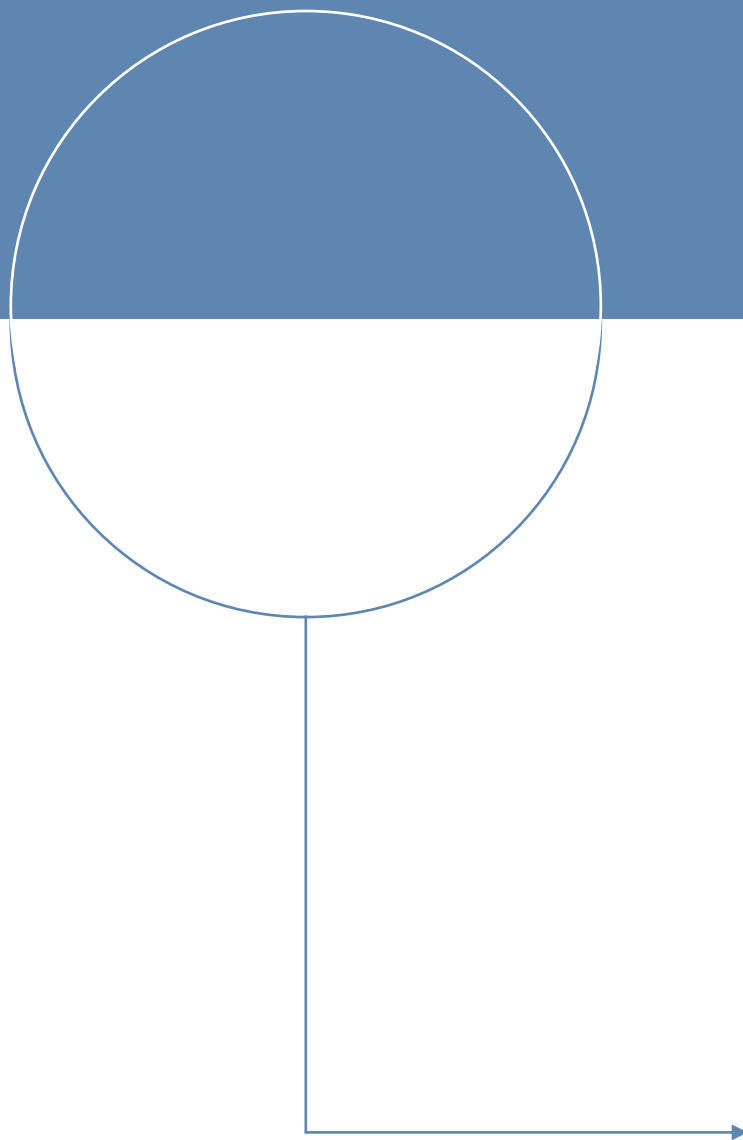
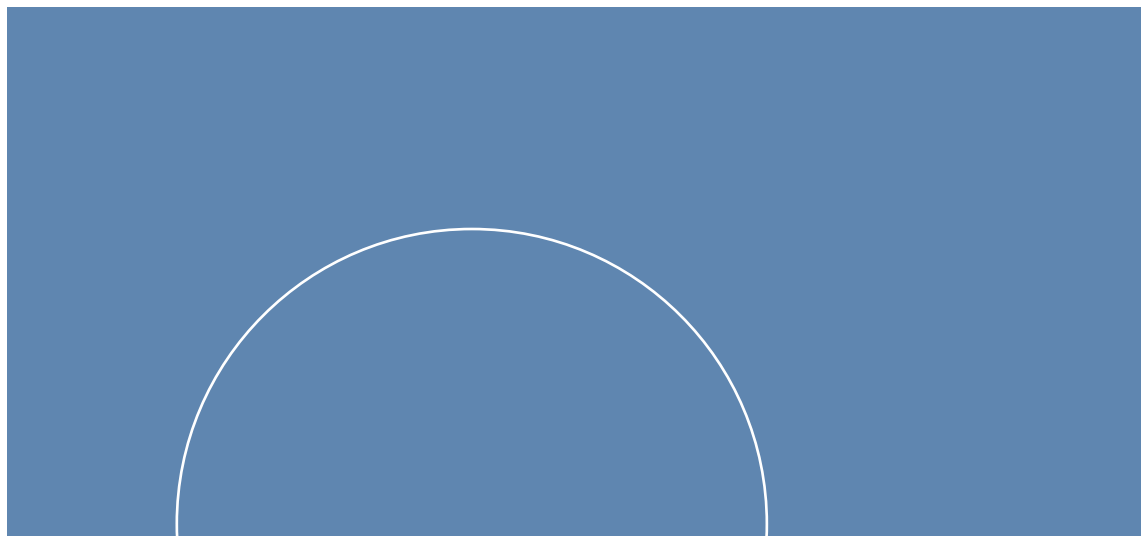


(b) FM104 and FM105.

Figure 73: FM103, FM104 and FM105







Norwegian University of  
Science and Technology